Spin and lattice properties of optically trapped exciton polaritons

Yago del Valle-Inclán Redondo

Department of Physics

University of Cambridge

This dissertation is submitted for the degree of

Doctor of Philosophy

King's College 2018

Spin and lattice properties of optically trapped exciton polaritons

Yago del Valle-Inclán Redondo

Exciton-polaritons are the fundamental excitations arising from the strong coupling of quantum well excitons and cavity photons in semiconductor microcavities. They are compound bosons for which stimulated scattering and macroscopic occupation of single quantum states can occur at sufficiently high densities. One way of creating such *polariton condensates* is with nonresonant optical pumping. Doing so creates a large density of free-carriers and excitons that strongly interact and blueshift the polariton energy levels. Using spatially patterned nonresonant fields, the polariton potential landscape can be tailored and optically trapped condensates can be created.

This thesis shows that the spin properties of polariton condensates are strongly modified by such trapping. Under linearly polarised pumping, helicity can spontaneously develop at a critical occupation, breaking the parity symmetry. This formation of spin-up/spin-down condensates is explained within a Gross-Pitaevskii model which accurately reproduces the influence of electric fields and condensate density. Under elliptically polarised pumping, two phenomena are observed: the formation of condensates with the opposite handedness to the pump and hysteresis of both occupation and spin with respect to pump power. The spatial dependence of these effects highlights the limitations of commonly used models of polariton condensation.

Finally, the suitability of patterned optical fields for the creation of polariton lattices is explored. For small chains of condensates, controllable coupling between adjacent spins is demonstrated, with the formation of antiferromagnetic and ferromagnetic domains. The extent of these domains is strongly affected by sample nonuniformity, fundamentally limiting the scalability of these lattices.

Declaration

I hereby declare that except where specific reference is made to the work of others, the contents of this dissertation are original and have not been submitted in whole or in part for consideration for any other degree or qualification in this, or any other University. This dissertation is the result of my own work and includes nothing which is the outcome of work done in collaboration, except where specifically indicated in the text. This dissertation contains less than 60,000 words including appendices, bibliography, footnotes, tables and equations.

Yago del Valle-Inclán Redondo

2018

Acknowledgements

This PhD has seen me through some of the best and worst times in my life so far, and I could not have made it through without a wonderful group of people supporting me.

First, I am extremely thankful to my supervisor Jeremy Baumberg for giving me the opportunity to be a part of the NanoPhotonics research group, and for being an extraordinary supervisor and person. I would also like to thank Hamid Ohadi, for being able to put up with me for three years and being an indispensable source of knowledge. I am also indebted to our collaborators Yuri Rubo, Tim Liew, Helgi Sigurdsson and Andrew Ramsay for invaluable contributions and insights, as well as to Pavlos Savvidis for taming the MBE beast.

Despite the frustrations involved in completing this PhD, I have immensely enjoyed my time in NanoPhotonics and the positive influence of such a congenial and affable group of people cannot be overstated. Special thanks go to William Deacon, Marie-Elena Kleemann, Rohit Chikkaraddy, Cloudy Carnegie, and Bart de Nijs, for proof-reading my thesis and, together with Alexander Casalis de Pury, Sean Cormier, Jamie Dolan, Junyang Huang, Dean Kos, Charlie Readman, Ana Andrés Arroyo, Vladimir Turek, Orr Be'er, and Alexander Dreissman, for dispelling the myth of socially inept physicists. Beyond NanoPhotonics, I cannot but extend my gratitude to the friends I have made along the way, in no particular order, Rodrigo García-Velasco Bernal, David Lamoureux, Rhys Jones, Allegra Fryxell, Daniel Petersen, Bhasi Nair, Angela Wittmann, Simon Price, Jen Upton, Nino Guruli, Emma Nicholls, Luna Sabastian, Adam Lewicki, CJ, SOKC, Papón and Stir.

This project could have not been materialised without Richard Bowman spearheading the use of Python in the lab, Anthony Barnett tirelessly providing support, or without the financial support of the Winton Programme for the Physics of Sustainability, EPSRC, CHESS and la Caixa. I also want to thank, from the bottom of my heart, the support and understanding my family has extended, without which I would not have become the person I am today.

Above all, I want to thank Shiru.

Abstract

Exciton-polaritons are the fundamental excitations arising from the strong coupling of quantum well excitons and cavity photons in semiconductor microcavities. They are compound bosons for which stimulated scattering and macroscopic occupation of single quantum states can occur at sufficiently high densities. One way of creating such *polariton condensates* is with nonresonant optical pumping. Doing so creates a large density of free-carriers and excitons that strongly interact and blueshift the polariton energy levels. Using spatially patterned nonresonant fields, the polariton potential landscape can be tailored and optically trapped condensates can be created.

This thesis shows that the spin properties of polariton condensates are strongly modified by such trapping. Under linearly polarised pumping, helicity can spontaneously develop at a critical occupation, breaking the parity symmetry. This formation of spin-up/spin-down condensates is explained within a Gross-Pitaevskii model which accurately reproduces the influence of electric fields and condensate density. Under elliptically polarised pumping, two phenomena are observed: the formation of condensates with the opposite handedness to the pump and hysteresis of both occupation and spin with respect to pump power. The spatial dependence of these effects highlights the limitations of commonly used models of polariton condensation.

Finally, the suitability of patterned optical fields for the creation of polariton lattices is explored. For small chains of condensates, controllable coupling between adjacent spins is demonstrated, with the formation of antiferromagnetic and ferromagnetic domains. The extent of these domains is strongly affected by sample nonuniformity, fundamentally limiting the scalability of these lattices.

List of publications

1. Yago del Valle-Inclan Redondo, Helgi Sigurdsson, Hamid Ohadi, Ivan A. Shelykh, Yuri G. Rubo, Zacharias Hatzopoulos, Pavlos G. Savvidis, Jeremy J. Baumberg. *Trap-size dependent spin inversion and hysteresis in optically trapped polariton condensates*. In preparation

2. Yago del Valle-Inclan Redondo, Hamid Ohadi, Yuri G Rubo, Orr Beer, Andrew J Ramsay, Symeon I Tsintzos, Zacharias Hatzopoulos, Pavlos G Savvidis, Jeremy J Baumberg. *Stochastic spin flips in polariton condensates: nonlinear tuning from GHz to sub-Hz.* New J. Phys. **20** 075008, 2018

3. Hamid Ohadi, Alexander Dreismann, Yuri G. Rubo, Florian Pinsker, Yago del Valle-Inclan Redondo, Symeon I. Tsintzos, Zacharias Hatzopoulos, Pavlos G. Savvidis, Jeremy J. Baumberg. *Spontaneous Spin Bifurcations and Ferromagnetic Phase Transitions in a Spinor Exciton-Polariton Condensate.* Phys. Rev. X **5**, 031002, 2015

4. Alexander Dreismann, Hamid Ohadi, Yago del Valle-Inclan Redondo, Ryan Balili, Yuri G. Rubo, Simeon I. Tsintzos, George Deligeorgis, Zacharias Hatzopoulos, Pavlos G. Savvidis, Jeremy J. Baumberg. *A sub-femtojoule electrical spin-switch based on optically trapped polariton condensates.* Nature Materials **15**, 1074 2016

5. Hamid Ohadi, Yago del Valle-Inclan Redondo, Alexander Dreismann, Yuri G. Rubo, Florian Pinsker, Symeon I. Tsintzos, Zacharias Hatzopoulos, Pavlos G. Savvidis, Jeremy J. Baumberg. *Tunable Magnetic Alignment between Trapped Exciton-Polariton Condensates.* Phys. Rev. Lett. **116**, 106403, 2016

6. Hamid Ohadi, Andres J. Ramsay, Helgi Sigurdsson, Yago del Valle-Inclan Redondo, Symeon I. Tsintzos, Zacharias Hatzopoulos, Timothy C. H. Liew, Ivan A. Shelykh, Yuri G. Rubo, Pavlos G. Savvidis, and Jeremy J. Baumberg *Spin Order and Phase Transitions in Chains of Polariton Condensates* Phys. Rev. Lett. **119**, 067401, 2017

7. Hamid Ohadi, Yago del Valle-Inclan Redondo, Andrew J. Ramsay, Zacharias Hatzopoulos, Timothy C. H. Liew, Paul R. Eastham, Pavlos G. Savvidis, Jeremy J. Baumberg *Synchronization crossover of polariton condensates in weakly disordered lattices* Phys. Rev. B **97**, 195109, 2018

8. Orr Be'er, Hamid Ohadi, Yago del Valle-Inclan Redondo, Andrew J. Ramsay, Symeon I. Tsintzos, Zacharias Hatzopoulos, Pavlos G. Savvidis, Jeremy J. Baumberg *Strain-assisted optomechanical coupling of polariton condensate spin to a micromechanical resonator* Appl. Phys. Lett. **111**, 261104 2017

9. William M. Deacon, Anna Lombardi, Felix Benz, Yago del Valle-Inclan Redondo, Rohit Chikkaraddy, Bart de Nijs, Marie-Elena Kleemann, Jan Mertens, and Jeremy J. Baumberg *Interrogating Nanojunctions Using Ultraconfined Acoustoplasmonic Coupling* Phys. Rev. Lett. **119**, 023901, 2017

Contents

Contents xiii
List of Figures xv
Chapter 1 Outline 1
Chapter 2 Introduction 5
2.1 Excitons 5
2.2 Semiconductor microcavities 10
2.3 Exciton polaritons 14
2.4 Polariton condensation 18
2.4.1 Theoretical model 23
2.5 Optical trapping 25
Chapter 3 Methods 29
3.1 Experimental setup 29
3.1.1 Technical details 32
3.1.2 Spatial light modulation 35
3.2 Samples 39
Chapter 4 Spontaneous spin bifurcation 43
4.1 Stochastically magnetised condensates 44
4.1.1 Reservoir density dependence 47
4.2 Single-mode mean-field model 48
4.2.1 Gross-Pitaevski equations 50
4.2.2 Polarisation splitting 53
4.2.3 Connection to self-trapping 54
4.3 Electrical control 57
4.3.1 Spin flips and hysteresis 60
4.4 Conclusion 63
Chapter 5 Spin flips and dynamical instability 65
5.1 Stochastic spin flips 65
5.2 Mean-field theory and dynamical instability 70
5.2.1 Frequency combs and chaos 73
5.3 Conclusion 76

Chapter 6 Nonresonant bistability 77
6.1 Spin and intensity hysteresis 79
6.1.1 Trap size and position dependence 83
6.1.2 Spatial profiles 85
6.1.3 Energy 87
6.2 Insufficient Gross-Pitaevskii and possible extensions 89
6.3 Conclusion 92
Chapter 7 Coupled condensates 95
7.1 Ferromagnetic-antiferromagnetic transition 96
7.1.1 Josephson coupling 100
7.1.2 Unexplained phenomenology and experimental issues 103
7.2 Spin chains 106
7.3 Conclusion 113
Chapter 8 Conclusion 115
Appendix A Alignment procedure 119
References A-1

List of Figures

Figure 2.1 GaAs bandstructure. 6
Figure 2.2 Quantum well wavefunctions 7
Figure 2.3 Bandstructure diagram 8
Figure 2.4 Fine structure of the excitonic ground state 9
Figure 2.5 TMM simulations of a typical DBR cavity. 12
Figure 2.6 Angular dependence of photonic modes. 13
Figure 2.7 Strong coupling of excitons and photons. 16
Figure 2.8 Simplified picture of polariton condensation. 21
Figure 2.9 Expanding condensates. 26
Figure 2.10 Transition to trapped condensates. 27
Figure 3.1 Simplified beam path. 31
Figure 3.2 Typical experimental setup 32
Figure 3.3 Spatial disorder. 33
Figure 3.4 Focusing. 34
Figure 3.5 Cryostat and objective mounts 35
Figure 3.6 SLM offset. 36
Figure 3.7 Basic IFTA principle. 37
Figure 3.8 Hexagonal MRAF patterns. 38
Figure 3.9 Oscillator model fit. 39
Figure 3.10 Sample structure. 40
Figure 4.1 Optically trapped condensates. 44
Figure 4.2 Polarisation-resolved emission. 45
Figure 4.3 Condensate stability and ellipticity. 46
Figure 4.4 Influence of reservoir overlap. 47
Figure 4.5 Power dependence 48
Figure 4.6 Comparison of simulations and experiment. 52
Figure 4.7 Energy and dissipation splitting. 53
Figure 4.8 Conservative physics and self-trapping. 55
Figure 4.9 Dissipative physics and spin bifurcation. 56

Figure 4.10 Voltage-induced polarisation splitting. 58
Figure 4.11 Electrical control of spin bifurcation. 59
Figure 4.12 Electrical spin switching. 60
Figure 4.13 Basins of attraction. 61
Figure 4.14 Spin hysteresis with voltage. 62
Figure 5.1 Condensate occupation. 66
Figure 5.2 Trap size dependence 68
Figure 5.3 Spin flip time. 69
Figure 5.4 Simulated power dependence. 72
Figure 5.5 Simulations with no noise. 74
Figure 5.6 Chaos. 75
Figure 6.1 Typical hysteresis loop 77
Figure 6.2 Optical trapping. 78
Figure 6.3 Spin inversion and collapse. 80
Figure 6.4 Polarisation and intensity hysteresis. 82
Figure 6.5 Trap size dependence. 83
Figure 6.6 Sample position dependence. 84
Figure 6.7 Spatial profiles. 86
Figure 6.8 Condensate energies. 87
Figure 6.9 Condensate energy splitting. 88
Figure 6.10 Simulations. 91
Figure 7.1 Schematic pumping geometry. 96
Figure 7.2 Coupled spins. 97
Figure 7.3 Coupled spin flips. 98
Figure 7.4 Barrier dependence. 99
Figure 7.5 Josephson coupling. 101
Figure 7.6 Power dependence. 104
Figure 7.7 Population imbalance. 104
Figure 7.8 Slow spin oscillations. 106
Figure 7.9 Four coupled condensates. 107
Figure 7.10 Barrier dependence of magnetic order. 108
Figure 7.11 Spin chains and iterative optimisation. 111

Chapter 1 Outline

Semiconductor physics is a very productive part of current academic and industrial research, as well as an integral part of many industries and devices, particularly in microelectronics. The development of the transistor in the middle of the 20th century revolutionised technology and paved the way for all modern electronics. Most current applications of semiconductors rely on inorganic material systems (silicon, GaAs, InP…), which have been heavily studied for many decades. [1,2] Recently, there has also been a push towards using organic semiconductor materials, which hold the promise of new applications and devices. [3] This thesis is focused on inorganic semiconductors (GaAs, in particular), where crystal growth has been perfected to the level that individual atom layers of different semiconductor alloys can be controllably and sequentially deposited. Complex electronic heterostructures can be created, from relatively simple p-i-n junctions and transistors, to 2D electron gases. Such incredible control of semiconductor interfaces has kept inorganic semiconductors at the forefront of many research fields in physics, particularly thanks to the confinement of electronic excitations down to the quantum level and the creation of quantum wells, wires and dots for confinement in two, one or zero dimensions.

The coupling of light to such quantum structures is especially interesting, and has led to the development of modern laser diodes, quantum cascade lasers and single-photon sources, to name a few. This thesis focuses on a specific aspect of the coupling of light and matter in GaAs microcavities: exciton polaritons. These are quasiparticles arising from the strong coupling of quantum well excitons and cavity photons, generally in the visible to NIR part of the electromagnetic spectrum. They bridge two aspects of semiconductor research: possible integration into the next generation of devices, [4] and interesting quantum effects. [5]

Because of their mixed light-matter nature, the properties of polaritons are relatively unique within the quasiparticle zoo of solid state physics. They are bosons, they have very light

masses (five orders of magnitude smaller than a free electron), and they interact via their excitonic component. The combination of these three properties allows them to form a quantum condensed phase at relatively high temperature (between 4K and room temperature, depending on the material). This condensed state is a quantum nonlinear fluid akin to both Bose-Einstein condensates and lasers, and that also has a spin degree of freedom.

As explained in further detail in the next chapter, polariton condensates can be created using off-resonant photons at a higher energy than the polaritons. These photons create free carriers (electrons and holes) inside the microcavity which recombine and form a cloud of hot excitons. These then thermally relax, feeding the polariton quantum fluid. Spatially tailoring the shape of the pumping light allows one to tune both the energy and the gain of the polariton condensate. The gain is influenced because locations with higher light intensity lead to denser clouds of excitons, which leads to the creation of more polaritons. The energy is tuned because the exciton energy is higher in the presence of other excitons, blueshifting the polariton energy in those sample locations which are pumped more strongly. Hence, by careful design of an optical pump pattern, the properties of polariton quantum fluids can be tuned. Of special interest to this thesis is the possibility of creating optically-trapped condensates, and the first few chapters focus on how the spin properties of these trapped polariton condensates can be controlled with external optical and electric fields.

The second aspect this thesis studies is the possibility of building lattices from polariton condensates. Many different fields of physics research are currently devoted to developing implementations of quantum simulators: a well-controlled system that is used to emulate the unknown physics of a complex system. [6–9] Lattices are a typical geometry for quantum simulators as they mimic the structure of solid state systems, and there has been a lot of work creating polaritonic lattices using different techniques. [10–15] This thesis presents the first steps in using optically-trapped polariton condensates to build lattices.

Chapter 2 introduces the basic concepts of polariton physics, from excitons and microcavities to polariton condensates and potential landscaping and trapping using optical fields. Chapter 3 presents the experimental setup, sample structure and how optical patterns can be created using spatial-light modulators. Chapter 4 presents the new spin physics that arise in optically

trapped polariton condensates: a spin bifurcation where the condensate spontaneously develops handedness. A theoretical framework is developed and shown to reproduce experimental observations and dependence on external electrical fields. Chapter 5 generalises this theory to include spin noise, demonstrating that spontaneous spin flips can occur and how the spin flip rate can be controllably varied over many orders of magnitude. Chapter 6 then considers a situation where handedness is introduced externally, rather than being spontaneously chosen. This leads to two effects: an inversion of the handedness at high powers, and bistability in both the spin and the intensity of polariton condensates. Finally, Chapter 7 is devoted to using trapped condensates to create lattices, starting from the demonstration of controllable coupling between two condensates and ending with a closed spinor chain of condensates showing different magnetic phases.

Chapter 2 Introduction

Semiconductor microcavities are an incredible achievement of semiconductor engineering. Careful deposition of very thin layers (between 20 and 100 atoms thick) of alloys of different band gaps and refractive indexes creates structures in which both excitons (Sec. 2.1) and photons (Sec. 2.2) can be trapped and controllably coupled. This thesis focuses on $Al_xGa_{1-x}As$ microcavities with GaAs quantum wells, as their growth methods are well established and cavities have low spatial disorder. For sufficiently high-quality samples, the coupling between excitons and photons can be strong enough to overcome losses, causing photons and excitons to stop being the fundamental system excitations and new eigenmodes to be formed: exciton-polaritons (Sec. 2.3). This chapter introduces the basic concepts required to understand the physics of polaritons, focusing on how quantum condensates can be created (Sec. 2.4) and manipulated with nonresonant optical fields (Sec. 2.5). It is meant as an introduction to the physics of the following chapters and not an overview of the whole field.

2.1 Excitons

The ground state of a semiconductor is a valence band full of electrons. This ground state can be excited if enough energy (the band gap) is provided and an electron is promoted to the conduction band, where it interacts with the sea of valence electrons. This interaction can be described as an interaction between an electron in the conduction band and a *hole* left by its absence in the valence band. This hole behaves like a positively charged quasiparticle moving in a neutrally charged band, so the semiconductor ground state can be thought of as a vacuum from which positively (holes) and negatively (electron) charged particles can be excited. This section deals with the properties of and interactions between electrons and holes in bulk and quantum well GaAs, unless otherwise mentioned.

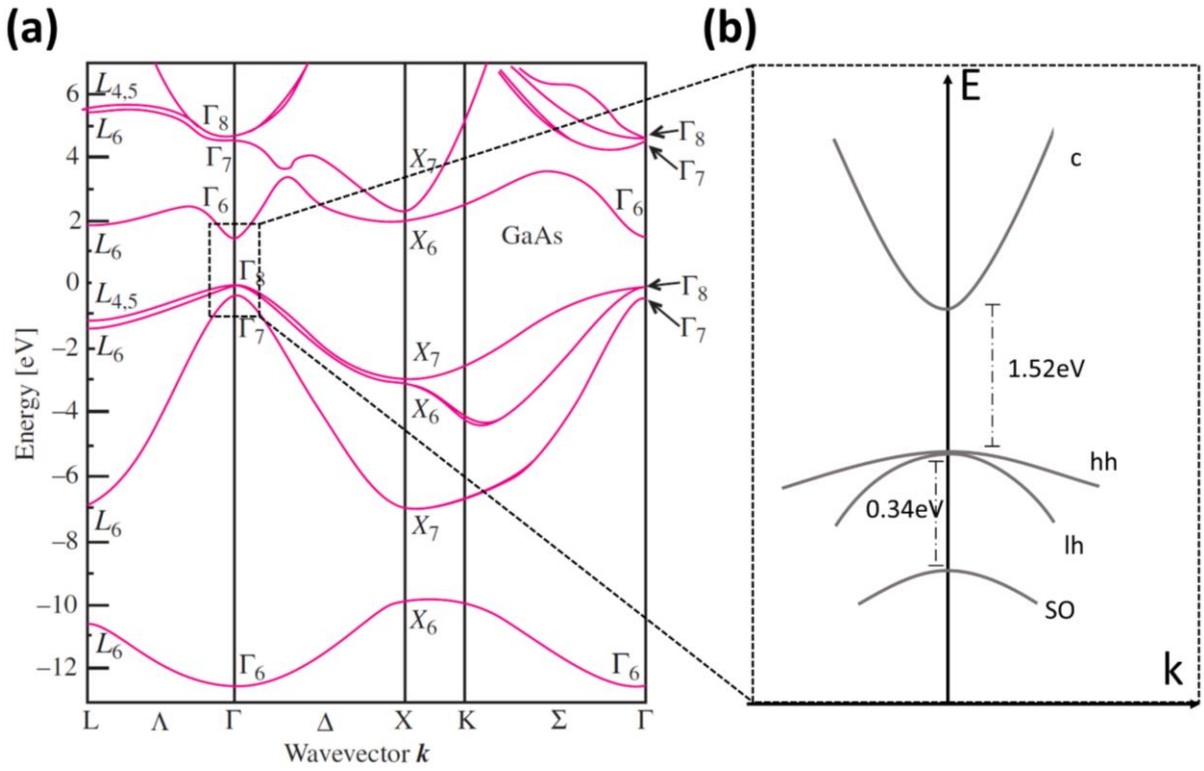

Figure 2.1 **GaAs bandstructure**. **(a)** Full structure of valence (E<0) and conduction (E>0) bands along high-symmetry directions. Taken from [1] **(b)** Band diagram around the direct band-gap transition

The fundamental property needed to understand semiconductor physics is the band structure: the relationship between electron's energy and momentum. Band structures are generally very complicated, with multiple valence and conduction bands that all have a complex three-dimensional structure (Figure 2.1a). A typical approximation is to ignore all bands except those near the direct band gap transition (Γ-point, Figure 2.1b), which is appropriate for optical experiments in the red and near-IR part of the electromagnetic spectrum. In this limit, the dispersion of each band becomes approximately quadratic: the particle energy is proportional to the square of the momentum. This is the same as the kinetic energy of a free particle with an *effective mass*, determined by the band properties. In general, the effective mass can be anisotropic in momentum space, [1] but this effect plays no role in the physics considered here and will be ignored.

Around the Γ-point, in addition to the conduction band, there are three valence bands: heavy-hole, light-hole and the split-off (Figure 2.1b). These bands differ in their $J = L + S$ (total spin) and m_z (projection of J): split-off holes have $J = 1/2$ and heavy-holes and light-holes have $J = 3/2$ but different m_z ($m_z^{hh} = \pm 3/2$ and $m_z^{lh} = \pm 1/2$). For the purposes of this

thesis, only energy levels within 100meV of the bandgap are relevant, so split-off holes will be ignored and the effective masses for electrons, heavy holes and light holes are $m_e = 0.067\ m_0$, $m_{hh} = 0.53\ m_0$, and $m_{lh} = 0.08\ m_0$, with m_0 being the free-electron mass. [1] In the absence of a preferential axis in the system, the above picture in terms of a heavy- and a light-hole band is slightly more complicated. Holes with a well-defined m_z along an arbitrary axis will have different effective masses depending on their direction of propagation in the crystal and are hence not simply heavy or light. However, a full understanding of the 3D bandstructure in terms of $k \cdot p$ theory is not required for this thesis.

Nevertheless, the picture in terms of a heavy- and a light-hole band is a valid approximation in quantum wells (QWs), where there is a well-defined axis of projection for m_z (the growth direction). QWs are semiconductor heterostructures where a thin layer of a small-bandgap semiconductor is sandwiched between higher-bandgap semiconductors. This layer is so thin that the wave-nature of electrons and holes cannot be ignored, and the states become quantised (Figure 2.2). An estimate for the energy of the nth trapped state can be obtained assuming the potential well is infinitely deep and using the standard particle in a box quantum mechanics equation: [16]

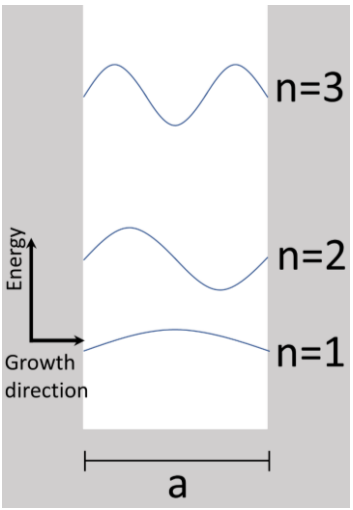

Figure 2.2 **Quantum well wavefunctions** First three modes (not to scale) of an infinitely deep quantum well

$$E = \frac{(\hbar\, n\, \pi)^2}{2\, m\, a^2} \qquad (2\text{-}1)$$

The QWs in this thesis are 10nm wide, which using the effective masses quoted earlier, leads to a ground state energy of 50meV for electrons, 10meV for HH and 40meV for LH. The barrier material in this thesis is $Al_{0.3}Ga_{0.7}As$, which has a bandgap 370meV higher than GaAs (Figure 2.3), leading to a confinement of ~200meV for electrons and ~100meV for holes. Since the confinement potentials are not infinite and are not the same for electrons and holes (Figure 2.3), these numbers are only an approximation but are a good rule of thumb. However, they provide an intuitive explanation about how the ground state of holes is split, making the HH the ground state.

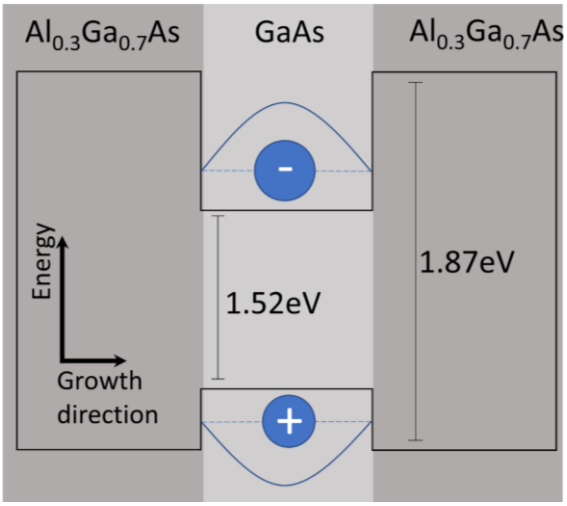

Figure 2.3 **Bandstructure diagram** of electron and hole energy levels for the quantum wells used in this thesis.

When considering the interaction between electrons and holes, a new bound quasiparticle appears: *excitons*. The Hamiltonian describing the interaction between an electron and a HH has a form reminiscent of the hydrogen atom Hamiltonian:

$$H = -\frac{\hbar^2\nabla^2}{2\,m_e} - \frac{\hbar^2\nabla^2}{2\,m_{hh}} - \frac{e^2}{4\,\pi\,\varepsilon\,|\boldsymbol{r}_e - \boldsymbol{r}_{hh}|} \tag{2-2}$$

where the charged particles, instead of a free electron and a proton, are an electron and a hole with mass m_e and m_{hh}, interacting inside a dielectric with constant ε, and with positions given by $\boldsymbol{r}_{e,hh}$. This Hamiltonian supports the existence of a bound state which has an energy and size, following the analogy with the hydrogen atom, given by (we only consider the *1s* exciton): [1,16]

$$\begin{aligned} E_b &= -\frac{\mu}{m_o {\varepsilon_r}^2} \times 13.6\ \text{eV} \\ a_b &= \frac{m_o \varepsilon_r}{\mu} \times 0.053\ \text{nm} \\ \frac{1}{\mu} &= \frac{1}{m_e} + \frac{1}{m_{hh}} \end{aligned} \tag{2-3}$$

where 13.6eV and 0.053 are the binding energy and radius of a hydrogen atom and where m_o is the free electron mass, μ is the effective masses of heavy-holes excitons and ε_r is the static relative permittivity of GaAs. From Eq.(2-3), HH-excitons are seen to have a binding energy of 4.9meV and size of 11.5nm. Following the same analogy, LH-excitons have a binding

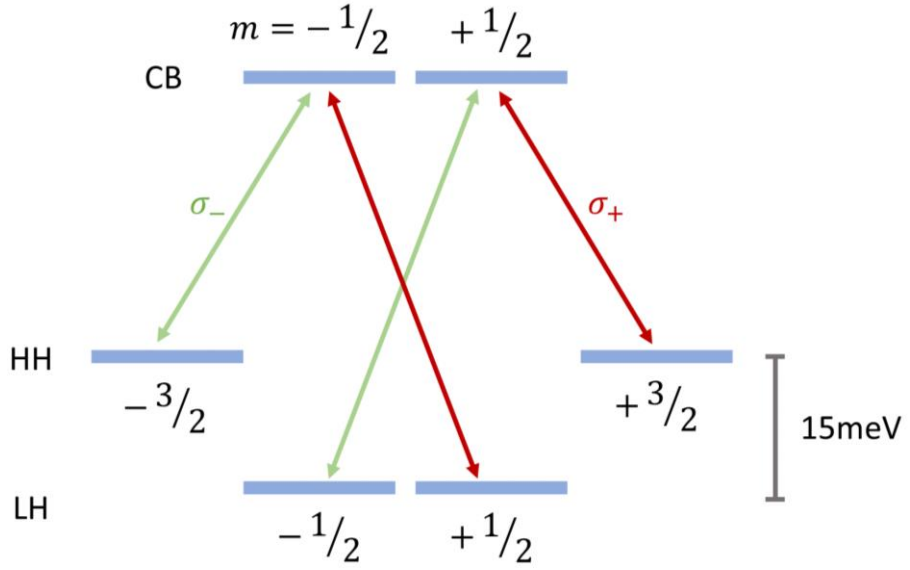

Figure 2.4 **Fine structure of the excitonic ground state** in a typical 10nm GaAs QW. Optical transitions for right-circular (red) and left-circular (green) polarisation are shown with arrows.

energy of 3meV and radius of 18.8nm. Although these values arise from a very simplistic model, they are an excellent approximation to the experimental values at low densities in 3D semiconductors. At high carrier densities, the presence of many electrons and holes screens the mean Coulomb interaction reducing the binding energy. This leads to the *Mott transition* in which the ground state of the system goes from a collection of excitons to a collection of correlated unbound electrons and holes. [17] In lower dimensional semiconductors, the increased spatial overlap between the electron and hole wavefunctions due to confinement also increases the binding energy (~10meV for HH-excitons) and oscillators strengths, making quantum well excitons more robust and easier to couple to light.

The spin structure of HH, LH and electrons in QWs at $k = 0$ is shown in Figure 2.4 (k will always refer to the momentum in the plane of the QWs). Electrons have $m_z = \pm 1/2$, HHs have $m_z = \pm 3/2$, and LHs have $m_z = \pm 1/2$. This leads to HH-excitons having either $m_z = \pm 2, \pm 1$, and LH-excitons having $m_z = \pm 1, 0$. By conservation of angular momentum, the $m_z = \pm 2$ cannot interact with light and are hence called dark excitons. All other excitons can interact with light. If light is circularly polarised (red and green in Figure 2.4), it interacts with excitons of $m_z = \pm 1$. As will be seen in Sec. 2.3, polariton physics are generally concerned with the ground-state, optically-active HH-excitons. This limitation is valid as long as there are no mechanisms for transforming these excitons into dark excitons or LH-excitons, as we discuss next.

There are three main spin relaxation mechanism for excitons in QWs, each with a different physical origin that causes different transitions between the excitonic fine structure:

- *Elliott-Yafet*. In this type of scattering, a moving exciton sees an electric field in the sample as an effective magnetic field that rotates its spin. The electric field can originate dynamically from phonons, or it can be due to static impurities in the sample, or from the crystal structure inversion asymmetry. [2] In QWs, this mechanism plays a major role in hole spin relaxation and causes a coupling between optically active and inactive excitons. [18]
- *Dyakonov-Perel*. The effective magnetic field in this case arises from spin-orbit splitting, either from non-centrosymmetric semiconductors or from asymmetric QWs, and also couples optically active and inactive excitons. [18] In contrast with the Elliott-Yafet mechanism where spin is preserved between scatterings, the spin here rotates between scatterings. Hence the spin relaxation rate increases as the impurity concentration decreases, and it becomes the major relaxation mechanism in bulk semiconductors. [2]
- *Bir-Aronov-Pikus* and *Maille, de Andrada e Silva, and Sham*. Although they are differently named, both of these spin relaxation effects arise from the Coulomb exchange interaction between electrons and holes. This exchange is the main exciton spin relaxation mechanisms in QWs, [2,18] and couples the two optically active heavy-hole excitons. [1] As excitons propagate through the sample, their spin precess in a direction perpendicular to their motion. After a few scatterings and changes of directions, the direction of the precession and the exciton spin is randomised leading to spin relaxation. For our experiments, the exciton spin relaxes with similar timescales (~100ps) to energy relaxation, and can play an important role in the formation of a steady state (Chapter 6).

2.2 Semiconductor microcavities

Microcavities are photonic resonators with spatial dimensions close to the wavelength of the light being trapped. To create a microcavity from semiconductor material, the first step is to

create mirrors in the form of distributed Bragg reflectors. DBRs are alternating layers of high- and low-refractive index materials (n_2, n_1), each of width given by $d_2 n_2 = d_1 n_1 = \lambda/4$. On their own, each layer only reflects a small fraction of incident light and does not behave like a mirror. But when combining the reflections from all the layers, they interfere destructively in the incoming direction and constructively on reflection, making DBRs very high-quality mirrors. Because this is an interference effect, DBRs only reflect light for a range of wavelengths (the stopband) around λ. The width of the stopband (Δ) is proportional to the refractive index contrast: [18]

$$\Delta = \frac{8}{\lambda} \frac{c}{} \frac{n_2 - n_1}{n_2 + n_1} \tag{2-4}$$

where c is the speed of light. Placing a spacer layer of width L_c in between two DBRs creates an optical cavity, akin to planar Fabry Perot resonators. [19] For cavities with ideal mirrors separated by L_c, the resonance wavelength is given directly by $L_c = m\,\lambda/2$. The situation is slightly more complicated in semiconductor structures for two reasons. Firstly, the limited bandwidth of the DBR reflection means that typically only one longitudinal mode is present in the cavity. This leads to cavities being described as $m\,\lambda/2$ cavities, where m is an integer corresponding to the longitudinal mode order. Secondly, due to the nonnegligible penetration of the electromagnetic field into the DBRs, the cavity resonance depends not only on the width of the cavity layer but also on the location of the DBR centre. [20]

Transfer-matrix simulations (TMM) are a good numerical approach for modelling the optical behaviour of semiconductor microcavities. [21] For the purposes of this thesis, it suffices to say that TMM is a numerically efficient computation of Fresnel-coefficients in multilayer structures.[1] The simulated reflectivity and mode profiles for a structure similar to that used in this thesis is shown in Figure 2.5. For simplicity, the refractive index dispersion and absorption of the $Al_xGa_{1-x}As$ compounds was ignored. The DBRs consists of 32 (35) layer-pairs with refractive index $n_2 = 3.5$ and $n_1 = 3$ and widths $d_2 = 57.2\text{nm}$ and $d_2 = 65.4\text{nm}$. They are placed above (below) a 595nm layer of refractive index 3.4. The DBR stopband goes from 750nm to 840nm (Figure 2.5a). The cavity resonance linewidth is smaller

[1] Simulations are done with the TMM Python package by Steven J. Byrnes https://github.com/sbyrnes321/tmm

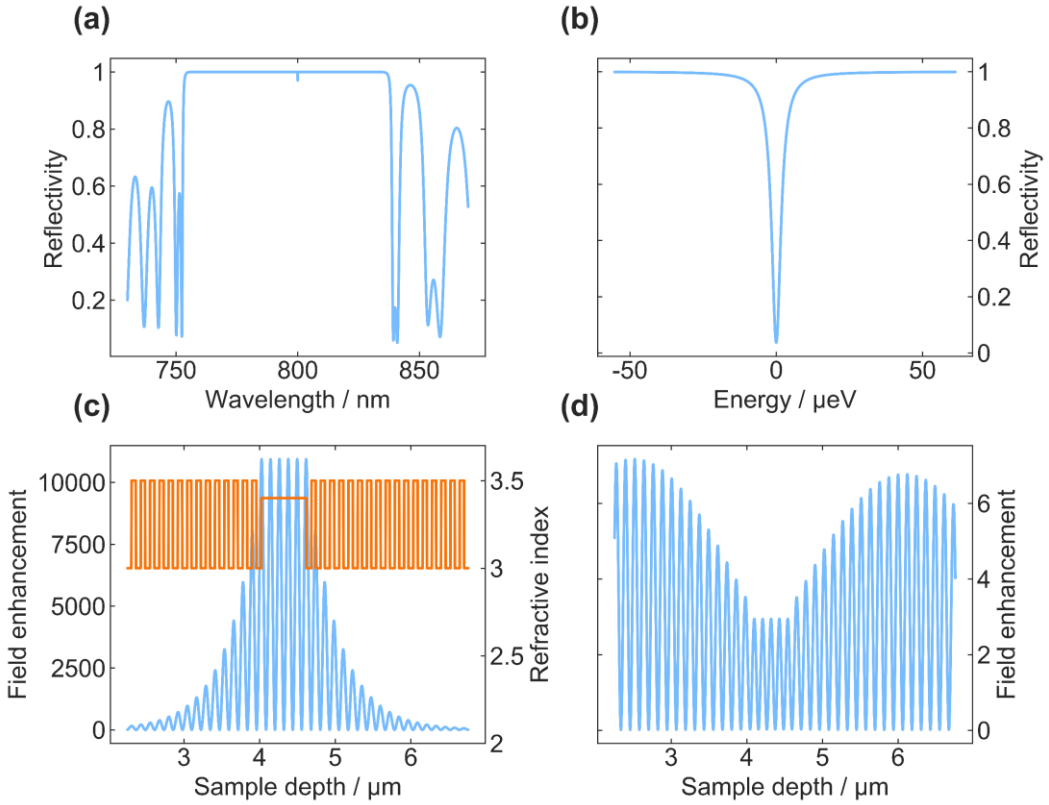

Figure 2.5 **TMM simulations of a typical DBR cavity**. **(a)** Reflectivity spectra at normal incidence, showing the DBR stopband and a small dip around the cavity resonance. The dip does not go down to zero because of the limited wavelength resolution. **(b)** Reflectivy around the cavity resonance showing the full cavity dip. Field distribution inside the microcavity for light **(c)** on resonance and **(d)** at the first DBR stopband mininum.

(~3.5μeV, Figure 2.5b) and Q-factor is larger (4×10^5) than in experiment by an order of magnitude. However, simulations including dispersion and absorption provide much better agreement. [22] In addition to the spectral position of the cavity resonance, an important feature of microcavities is the field distribution inside the cavity for an incident field of unit amplitude. For coupling to excitons (see next section), the relevant field distribution is that on the spectral resonance of the cavity, where the electromagnetic field has a very large amplitude at the centre of the cavity (Figure 2.5c), where quantum wells would be placed. For nonresonant optical pumping (Sec. 2.4), the relevant field distribution is that at 750nm (the stopband minimum), where the field amplitude inside the cavity is of a similar order of magnitude to the incident wave (Figure 2.5d) with most light penetrating into the cavity layer.

Two effects need to be considered when looking at the angular dependence of the microcavity modes. Firstly, due to the increased path length at higher angles, there is a

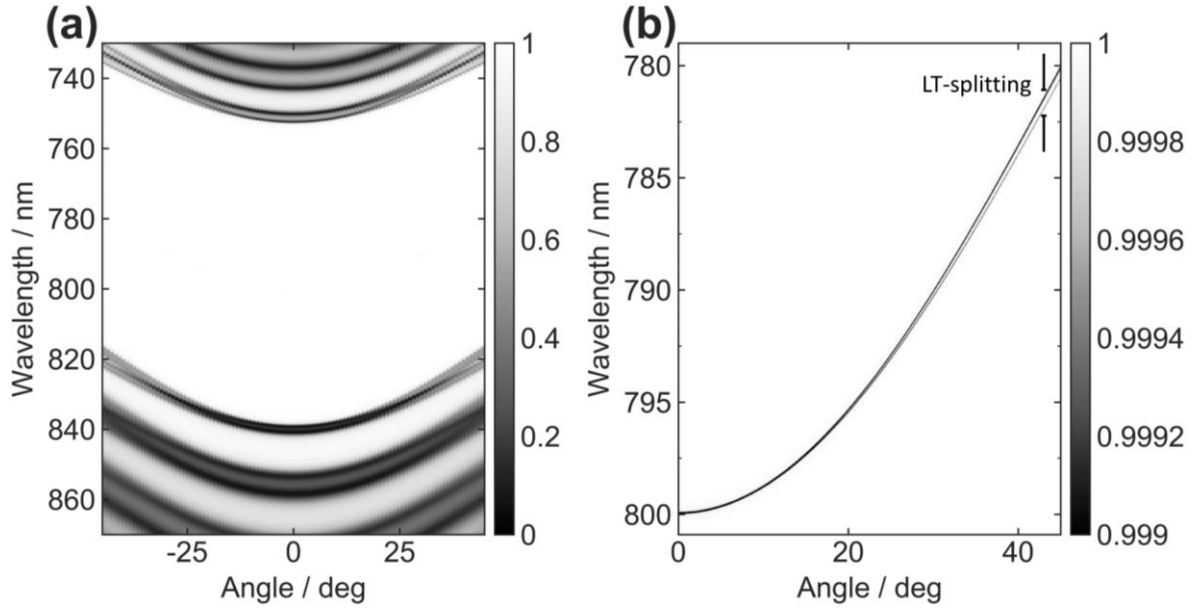

Figure 2.6 **Angular dependence of photonic modes**. **(a)** Reflectivity spectra at different angles, showing the hyperbolic dependence of the stopband. The cavity does not appear because of limited wavelength resolution. **(b)** Reflectivity spectra at different angles, focused around the cavity resonance, showing the hyperbolic dispersion and LT splitting at high angles. The colourbar is scaled such that the cavity dips can be easily seen despite limited resolution.

blueshift of the photonic energy with increasing angle, which appears in both the DBR stop band (Figure 2.6a) and the cavity resonance (Figure 2.6b). At small angles, the cavity dispersion is approximately quadratic, and an effective-mass approximation can also be applied to cavity photons leading to very light masses of $m_p \sim 10^{-5} m_0$. The second effect is a polarisation dependent splitting between *s*- (TE) and *p*- (TM) linearly polarised modes, simply referred to as LT-splitting. [23–25] It arises from the angular dependence of the Fresnel coefficients and hence is zero at normal incidence (*s*- and *p*- are equivalent) but can reach ~100μeV at high angles (just visible in Figure 2.6b).

Finally, in addition to polarisation splitting due to the angle of incidence, it is possible to have polarisation splitting at $k = 0$ due to birefringence. As will be further discussed in Chapter 4, even tiny levels of birefringence, on the order of 0.004%, produce measurable polarisation splittings. [26] This splitting is between two linearly-polarised, orthogonal modes in the plane of the microcavity, and is generally due to the local strain profiles in the cavity. Such a splitting can also be induced with applied electric fields due to the Kerr effect (see Sec. 4.3).

2.3 Exciton polaritons

When growing semiconductor microcavities, quantum wells can be deposited inside the cavity layer, leading to interaction between photons and excitons. Cavity photons can create quantum well excitons and quantum well excitons can radiatively decay into cavity photons. For sufficiently weak coupling, the effect is to increase the excitonic radiative lifetime via the Purcell effect as well as reduce the threshold required for lasing. [27] This is the basis of the huge field of vertical cavity surface emitting lasers (VCSELs), a widely used semiconductor laser with a billion-dollar industry. Although the underlying semiconductor structure of VCSELs is the same as in this thesis, the high-quality of the samples studied here leads to strong-coupling of excitons and photons. [28] What this means is that the exciton-photon interaction cannot be treated perturbatively, and it is no longer valid to think of excitons and photons as independent particles. Instead, the quasiparticles of the system are mixed excitons and photons called *exciton polaritons*, or simply polaritons.

To illustrate the new properties arising from strong coupling it is useful to make two assumptions to reduce the excitonic energy level structure (Figure 2.4) to a single mode that can be coupled to light. Firstly, only the optically active ground state will be considered, so both LH and $J = 2$ dark HH states will be ignored. Secondly, the m-sublevels will be assumed to be degenerate. With these assumptions, the excitonic field can be described as a single mode that is coupled to the single mode of the photonic field:

$$H = \sum_k (E_C(k) - i\Gamma_C)\, A_k^\dagger A_k + (E_X(k) - i\Gamma_X)\, B_k^\dagger B_k + \hbar\Omega(A_k^\dagger B_k + B_k^\dagger A_k) \tag{2-5}$$

Where $E_{C,X}$ are the cavity and exciton dispersions, $\Gamma_{C,X}$ are the cavity and exciton decays, A_k and B_k are the photon and exciton annihilation operators, and Ω is the coupling energy between the two oscillators (Rabi splitting). This approximation is called the coupled oscillator model and the complex Hamiltonian can be diagonalized by transforming it into the so called polariton basis:

$$a_k^L = X_k\, B_k - C_k\, A_k \tag{2-6}$$

$$a_k^U = X_k\, B_k + C_k\, A_k$$
$$E_{U,L} = \frac{1}{2}\left[(E_X + E_C - i(\Gamma_C + \Gamma_X)) \pm \sqrt{4\,\hbar^2\Omega^2 + {\Delta_k}^2}\right]$$
$$\Delta_k = E_C(k) - E_X(k) - i(\Gamma_C - \Gamma_X)$$

where $a_k^{L,U}$ are the annihilation operators for lower and upper polaritons, and C_k, X_k are the Hopfield coefficients. [29] The amplitude of these coefficients corresponds to the photon (C_k) and exciton (X_k) component fraction of the lower polariton:

$$|X_k|^2 = \frac{1}{2}\left(1 - \frac{\Delta_k}{\sqrt{4\,\hbar^2\Omega^2 + {\Delta_k}^2}}\right)$$
$$|C_k|^2 = \frac{1}{2}\left(1 + \frac{\Delta_k}{\sqrt{4\,\hbar^2\Omega^2 + {\Delta_k}^2}}\right) \qquad (2\text{-}7)$$
$$|X_k|^2 + |C_k|^2 = 1$$

This framework can in general be generalised to include LH-excitons in the Hamiltonian of Eq. (2-5), which leads to an additional polariton mode, called the middle polariton. Middle polaritons are generally ignored, as they are not the ground state and their coupling to the cavity field is weaker, although some experiments have been dedicated to them. [30,31]

From Eq. (2-6), the energy difference between the two polariton modes at zero detuning ($E_C = E_X$) is given by $\sqrt{4\,\hbar^2\Omega^2 - (\Gamma_C - \Gamma_X)^2}$. If this splitting is imaginary the system is said to be in the *weak coupling* regime, in which the excitons and photons are still the eigenmodes of the system, but have their lifetimes modified (Purcell effect). If the splitting is real, the system is in the *strong coupling* regime, and the emission energies are modified. Two approaches are most commonly used to overcome weak coupling. The first is to increase the photon lifetime by using higher-reflectivity DBRs, either by using different alloys with higher refractive index contrast or depositing more layers. The second is to increase the excitonic density by placing multiple quantum wells (N_{QW}) inside the cavity spacer, leading to an increase in the Rabi splitting: [20,32,33]

$$\Omega \propto \sqrt{f_{osc}\, N_{QW}} \tag{2-8}$$

where f_{osc} is the QW oscillator strength and is proportional to the dipole matrix element of the excitonic transition.

The effect of strong coupling can be visually represented by how the energy and Hopfield coefficients vary as a function of wavevector (Figure 2.7). The dispersions in the weak-coupling limit ($E_{C,X}$), give way to dispersions ($E_{U,L}$) with new wavevector dependences. Additionally, the ratio between photonic and excitonic mixture of polaritons changes with wavevector. At high momentum, the lower polariton is mostly excitonic and the upper polariton is mostly photonic, while at low momentum both polaritons have non-negligible

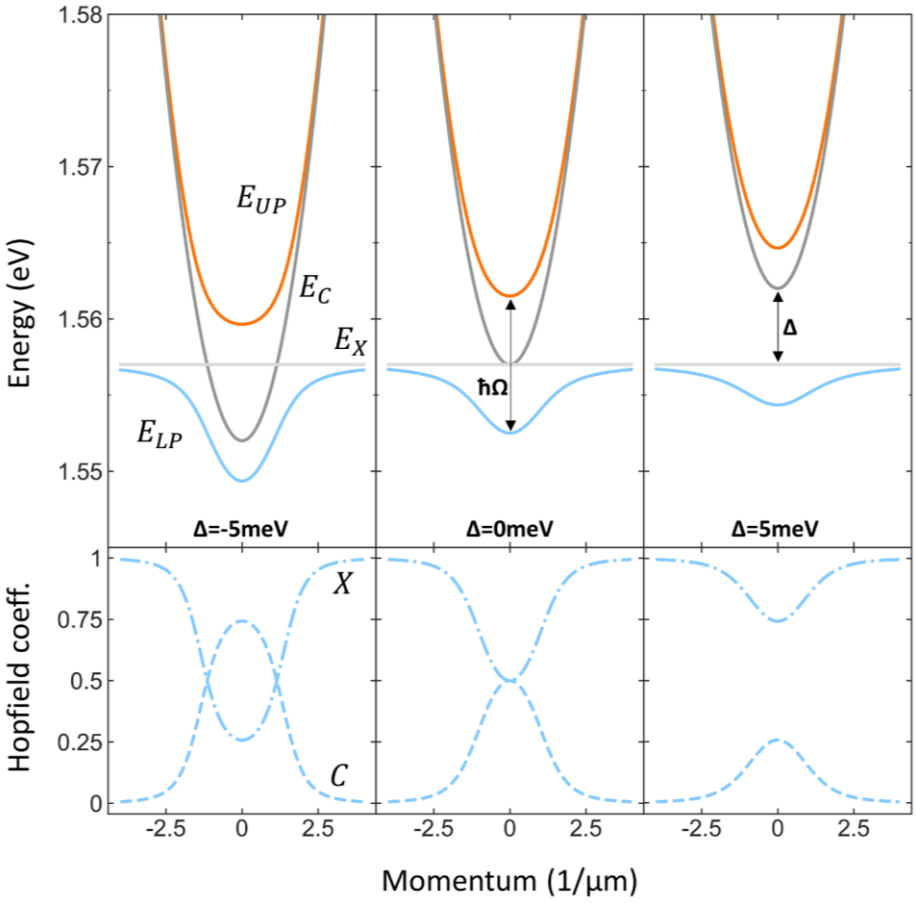

Figure 2.7 **Strong coupling of excitons and photons**. **(top row)** Dispersion relations of cavity E_C, exciton E_X and upper and lower polaritons $E_{UP/LP}$. **(bottom row)** Hopfield coefficients of the LP mode showing excitonic X and photonic C fractions, at different detunings between the cavity and exciton line.

amounts of both excitons and photons. Focusing on the ground state of the system (LP at $k = 0$), polaritons have properties coming from both components: small effective mass ($10^{-5}m_0$) and short lifetimes (~10ps) from the photonic part, and nonlinearity due to the Coulomb interaction between the excitonic parts.

Because of their photonic component, detecting polaritons is relatively straightforward by standard optical methods. The photonic field escaping the cavity has a one-to-one correspondence with the polaritonic field inside: the intensity corresponds to the polariton density, the emission angle is the wavevector, and the polarisation corresponds to the spin. More specifically, the Stokes components S_i of the light polarisation, directly correspond to the spin of the exciton-polariton field:

$$\begin{aligned} S_x &= \frac{I_H - I_V}{I_H + I_V} \\ S_y &= \frac{I_D - I_A}{I_D + I_A} \\ S_z &= \frac{I_R - I_L}{I_R + I_L} \\ S &= \sqrt{S_x^2 + S_y^2 + S_z^2} \end{aligned} \tag{2-9}$$

where $I_{H,V,D,A,R,L}$ are the intensities of horizontal-, vertical-, diagonal-, antidiagonal-, right-circular and left-circularly polarized light, $S_{x,y,z}$ are the degrees of polarisation of light and S is the light intensity.

There are two ways of creating polaritons: electrically [34–36] and optically. Optical methods can be divided into nonresonant (see next section) and resonant. Resonant experiments work by tuning an incident laser to the same energy and wavevector as the polariton resonance, such that incident photons enter the cavity and form polaritons. These polaritons are then able to freely propagate around the cavity and scatter, either from each other or from defects present in the sample. Three different regimes can be distinguished depending on the angle of the incident light. First, when pumping near the inflection point of the lower polariton dispersion (the so called magic angle), stimulated scattering between polaritons can dominate

the dynamics and an optical parametric oscillator can be formed. [37–41] This is a consequence of the unique shape of the LP dispersion, which allows for three real states to participate in the pair scattering without need for virtual states. Second, for angles smaller than the magic angle, scattering from sample disorder can dominate. Changing the polariton density by tuning the laser intensity modifies the properties of the polariton field and effects like superfluidity, [42,43] and spontaneous vortex/soliton formation [44–46] can be observed. Finally, resonant pumping can be done at normal incidence ($k = 0$). Despite the relative experimental simplicity, the nonlinear photonic properties of polaritons lead to a wide range of observations, from intensity [47] and spin [48–50] bistability, to squeezing, [51] Josephson self-trapping [52] and dissipative phase transitions. [53] In Chapter 7, resonant pumping at $k = 0$ will be used to coherently drive an existing polariton cloud causing it to change its spin state.

2.4 Polariton condensation

This section deals with polariton condensation under non-resonant optical pumping. Before addressing the specificities of the polariton system, it is important to have a basic understanding of what a condensate is. To do so, we begin with a simple introduction to the gold-standard: atomic Bose-Einstein condensates (BEC). The relevant quantity when describing an ideal atomic gas of mass m in a vacuum at temperature T is its thermal de Broglie wavelength: [54]

$$\lambda_{th} = \sqrt{\frac{2\,\pi\,\hbar^2}{m\,k_B T}} \tag{2-10}$$

when this wavelength is shorter than the interparticle distance, the boson gas can be described by classical thermodynamics. As the temperature or the interparticle distance is decreased the overlap between atomic wavefunctions can no longer be ignored, and atoms become phase coherent and macroscopically occupy the quantum ground state. This macroscopic coherent occupation of the ground state is what is called a BEC. This quantum state was first observed in 1995 with atomic gases, which required very low temperatures (nK to μK) and specialised

cooling techniques. [55–57] Although excitonic condensation had been suggested very early on, [58] it wasn't until soon after the observation of atomic BECs that the experimental viability of such experiments was re-addressed. [59] Exciton polaritons, having a much lighter mass and longer thermal de Broglie wavelengths than other quasiparticles, were the first to present condensation at liquid-He temperatures in the mid-2000s. [60–62] Subsequent work showed condensation at room temperature in different semiconductor materials. [63,64]

A more quantitative way of understanding this process is via thermodynamic distributions. Considering a grand canonical ensemble at temperature T, the occupation number n_i of a state at energy ε_i: [65]

$$n_i = \frac{1}{e^{\frac{\varepsilon_i - \mu}{k_B T}} - 1} \tag{2-11}$$

where k_B is the Boltzmann constant and μ is the chemical potential, which is fixed by the normalization condition $N = \sum n_i$ where N is the total number of particles. At high-temperatures, the chemical potential is large and negative, and increases monotonically as the temperature is reduced. If ε_0 is the lowest single-particle energy level, then at some critical temperature, when $\mu \to \varepsilon_0^{-}$, the normalization condition can be satisfied having $n_0 \sim N$ and a condensate is formed. It is instructive to find this critical temperature for a uniform ideal gas in the thermodynamic limit, so that $\varepsilon = p^2/2m$ with p being the momentum and m the mass. In this limit, the normalization condition can be replaced by an integral over the density of states:

$$\begin{aligned} N = \sum n_i \to \int \rho(\varepsilon) d\varepsilon = \int \frac{V}{(2\pi)^2} \left(\frac{2m}{\hbar^2}\right)^{\frac{3}{2}} \sqrt{\varepsilon}\, d\varepsilon \\ \therefore\ k_B T_c = \frac{2\pi\, \hbar^2}{m} \left(\frac{N}{V\, \zeta(3/2)}\right)^{2/3} \end{aligned} \tag{2-12}$$

where $\zeta(3/2) \approx 2.612$ is the Riemann zeta function. This can be rewritten as ${\lambda_{th}}^3 N/V = \zeta(3/2)$, meaning that the critical temperature, as said before, is when the thermal wavelength becomes comparable to the interparticle distance. Note that this critical temperature crucially depends on the density of states and so it is modified if the gas is in a harmonic trap (as it is

generally in cold atom experiments), or if the dimensionality of the system is different. In fact, in the case of two-dimensional systems (like QWs) there is no critical temperature and a BEC is never formed. Nevertheless, a macroscopically occupied state does appear at low temperatures through the Berezinskii–Kosterlitz–Thouless (BKT) transition, which some polariton experiments have aimed to detect. [66] The distinction between BEC and BKT will be ignored from here on, since it is minor compared to the other fundamental differences between atomic and polariton condensates that will be explored in the rest of this section.

In atomic systems, the density of an atomic cloud is selectively reduced via evaporative cooling to decrease the temperature and achieve condensation. The process is different for polariton BECs: the temperature is kept fixed and the density is increased until the interparticle distance is comparable to the thermal de Broglie wavelength. For condensation to take place, polaritons need to be able to spontaneously select their phase, i.e. they cannot inherit the phase coherence of the pump as they do in resonant experiments. By using high energy photons or electrical pumping, the relaxation of electronic excitations provides a mechanism for incoherently populating the ground state. For inorganic semiconductors (CdTe and GaAs), the typical simplified microscopic picture of this process is shown in Figure 2.8, and can be divided in four steps:

1. **Pumping**. Free carriers can be injected in two ways: optically or electrically. High energy photons at the DBR reflection minimum have enough energy to create free carriers inside the small bandgap region of the QWs. Alternatively, p- and n- doping the top/bottom DBR mirrors creates a p-i-n junction across the QWs that can be used for electrically injecting electrons and holes inside the cavity layer. [35,67]
2. **Exciton formation**. Two different exciton formation processes can occur: direct/geminate formation from a correlated e-h pair via optical phonon emission, or bimolecular formation via free carrier scattering. Both processes depend on the pumping strength: geminate formation is linearly proportional to the pump intensity, while bimolecular formation is proportional to the product of electron and hole densities. [68,69] The exact ratios of these processes to other recombination mechanisms are dependent on a variety of factors (e.g. spin, material quality, quantum well width, pumping intensity and energy). Hence a variety of exciton formation

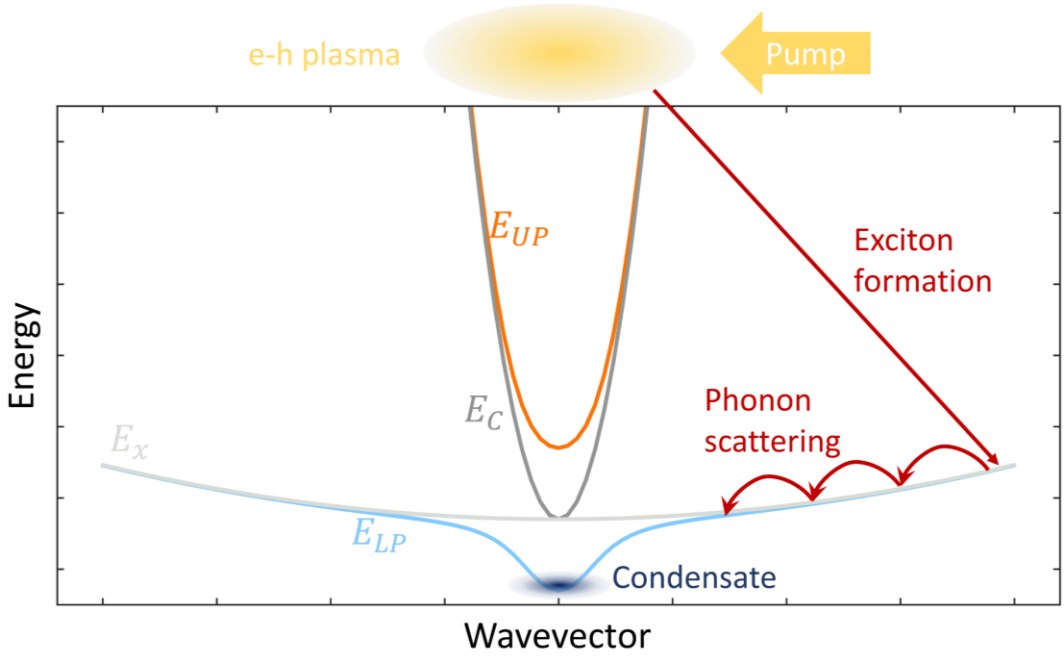

Figure 2.8 **Simplified picture of polariton condensation**. Incoherent pumping creates an electron-hole plasma at high energy. Energy relaxation happens via exciton formation and phonon emission until the ground state is macroscopically occupied.

timescales have been published in the literature (see [70] for a summary). For the densities in this thesis, exciton formation can be assumed to occur in under 100ps.

3. **Relaxation**. After formation, excitons have very large momenta and start losing energy primarily by emission of longitudinal phonons. The UP branch is generally ignored as it has very small excitonic component at high wavevectors and hence does not participate in the relaxation.
4. **Condensation**. After multiple phonon emissions, polaritons start to populate the ground state of the LP. If relaxation is sufficiently fast and pumping sufficiently strong, this population can be sufficiently dense for the ground state of the system to become condensed. The pump power at which this occurs is referred to as the condensation threshold, or simply threshold. Experimentally, there are three main signatures of condensation:
    a. Spontaneous build-up of spatial coherence, as evidenced in the formation of fringes in interferometry experiments.
    b. Spontaneous build-up of polarisation.
    c. Reduction of linewidth.
    d. Super-linear increase in emission intensity.

Within these simplified steps, the analogy between polariton and atomic condensates is clear. Both are simply a cloud of bosons that reaches a sufficiently high density/low temperature for quantum effects to take place. However, multiple factors distinguish polaritons and may question the full validity of the analogy with cold atoms:

- In atoms, thermalisation timescales are generally faster than the rate of decay, so atomic clouds tend to be in thermal equilibrium. This is not the case for polaritons, as the short cavity lifetimes mean thermalisation and decay timescales are comparable. Recently, using very long lifetime cavities, new claims have been made about the thermalisation of polaritons, [71] similar to those presented in the first works showing condensation. [61,62] Interpretation of these results is complicated by the fact that photon lasing also produces a thermalized emission, [72] and hence is not sufficient evidence for claiming a thermalized condensate.
- Similar to the previous point, the fast decay of polaritons requires a constant source of new particles. This means that in continuous wave experiments, the steady states of the system are the result of competition between pumping and decay, rather than a true thermodynamic state. This has no analogy in atomic BECs.
- The simplified picture of the relaxation processes presented previously does not necessarily capture all the relevant dynamics. In many experiments, a bottleneck is observed at the point where the lower polariton starts acquiring a more photonic component. [73,74] This creates a reservoir of excitons at medium energy and can change the process by which polaritons acquire coherence. Instead of coherence emerging as a quantum thermodynamic effect, stimulated scattering from this higher energy reservoir into the condensate can cause spontaneous coherence. This would make polariton condensates more like lasers, where coherence emerges due to stimulated emission. The relaxation process gets further complications from the spin dependence of this bottleneck, [75] the role of LHs, [30] and the bimolecular formation of dark excitons. [2]
- At high carrier densities, screening of the Coulomb interaction between electrons and holes means the properties of polaritons themselves start to be modified (Sec. 0). This leads to a saturation of the coupling strength and a transition to weak-coupling.

[17,76] If this happens the microcavity behaves like a conventional photon laser (VCSEL) and the emission energy is that of the cavity resonance, rather than the polariton. Another effect that can occur at high densities is a BEC-BCS-like transition where the composite nature of polaritons becomes important. In such a situation, polaritons do not behave as independent bosons, but rather as a sea of fermionic excitations that couple to light. [77]

- Finally, polariton condensates of different energies can be created simultaneously from the same shared pump. This highlights that these condensates are not necessarily the ground state of the system, and can be understood as an analogy with lasers, where multiple cavity modes can have enough gain to lase/condense.

Taking all of this into consideration, it is useful to think of polariton condensates as a hybrid between BECs and lasers: a coherent state formed of massive particles (like in a BEC) but where at least some of the coherence might be due to stimulated scattering and gain (similar to a laser).

2.4.1 Theoretical model

A relatively simple, but very effective, model for reproducing the behaviour of polariton condensates was developed by Wouters and Carusotto. [78,79] It is a mean-field approximation valid at the bottom of the LP dispersion, and where condensates have a macroscopic wavefunction $\psi(\boldsymbol{r})$ that is fed by an exciton reservoir $n(\boldsymbol{r})$:

$$i\hbar\frac{\partial\psi(\boldsymbol{r})}{\partial t} = \left\{E_0 - \frac{\hbar^2}{2m}\nabla_{\boldsymbol{r}}^2 + \frac{i\hbar}{2}\{R[n(\boldsymbol{r})] - \gamma_c\} + V_{ext}(\boldsymbol{r}) + \hbar g|\psi(\boldsymbol{r})|^2 + V_R(\boldsymbol{r})\right\}\psi(\boldsymbol{r})$$
$$\frac{dn(\boldsymbol{r})}{dt} = P(\boldsymbol{r}) - \gamma_R n(\boldsymbol{r}) - R[n(\boldsymbol{r})]|\psi(\boldsymbol{r})|^2 \quad (2\text{-}13)$$

where E_0 and m are the polariton energy and mass at the bottom of the dispersion, V_{ext} is the disorder potential, and P is the phenomenological pumping term. Coulomb interaction between the excitonic components leads to a repulsive polariton-polariton interaction constant $g > 0$. Polaritons are constantly decaying at a rate γ_c and being replenished at a rate $R[n(\boldsymbol{r})]$ by stimulated scattering from the reservoir, which is generally assumed to be

linearly proportional to density $R[n(\boldsymbol{r})] \propto n(\boldsymbol{r})$. The transition from a cloud of hot excitons to a polariton condensate occurs when this term is equal to γ_c and the steady state solution has $\psi(\boldsymbol{r}) \neq 0$. The term $V_R(\boldsymbol{r}) = g_R\, n(\boldsymbol{r}) + g_P\, P(\boldsymbol{r})$ accounts for the nonlinear interactions of polaritons with reservoir excitons and with other free carriers created by the pump P. Finally, the term γ_R corresponds to the effective decay of reservoir excitons. In the case $\gamma_R \gg \gamma_c$ the reservoir can be assumed to adiabatically follow the condensate $\dot{n}(\boldsymbol{r}) = 0$, in what is called the static reservoir approximation.

Equations with similar forms to Eq. (2-13) exist in different fields [54,80,81] and have different names: the complex nonlinear Schrodinger, Gross-Pitaevskii, or Ginzburg-Landau equations. The link to well-known nonlinear optics is made clearer by taking the static reservoir approximation and ignoring disorder, so that Eq. (2-13) becomes:

$$\begin{aligned} n(\boldsymbol{r}) &= \frac{P(r)}{\gamma_R + R\,|\psi(\boldsymbol{r})|^2} \approx \frac{P(r)}{\gamma_R}\left(1 - \frac{R}{\gamma_R}\,|\psi(\boldsymbol{r})|^2\right) \\ i\hbar\frac{\partial\psi(\boldsymbol{r})}{\partial t} &= \left\{E_0 - \frac{\hbar^2}{2m}\nabla_{\boldsymbol{r}}^2 + \frac{i\hbar}{2}[\tilde{P}(r) - \eta\,|\psi(\boldsymbol{r})|^2 - \gamma_c] + \hbar g|\psi(\boldsymbol{r})|^2 + V_R(\boldsymbol{r})\right\}\psi(\boldsymbol{r}) \end{aligned} \tag{2-14}$$

The second equation in Eq. (2-14) then directly maps to the diffraction equation of light moving inside a nonlinear medium with saturable absorption. [80] It is hard to over-state the generality of Eq. (2-13), which has been one of the factors behind the great success in describing the dynamics of polariton condensates for both resonant and nonresonant pumping.

However, this generality is also the main drawback. Since they are a phenomenological simplification and many of the parameters cannot be independently measured, their values are chosen to match individual experimental observations and are numerically optimised each time. This, combined with the complexity of the solutions of Eq. (2-13), can make it difficult to develop intuitive understanding of the governing physics. A good discussion of this problem for the specific case of the saturation parameter can be found in [82]. A second issue with these equations is that they can become numerically unstable and they require careful solver approaches and significant know-how, particularly in situations where the spatial degrees of freedom are important. A typical way of addressing this issue is to introduce an

additional, phenomenological energy relaxation that quantifies, not the decay rate of the polariton wavefunction itself, but of its energy. [83,84] Different forms of this energy relaxation can be considered, either simply proportional to the total energy, [85] to the kinetic energy, [86] or to a combination of reservoir density and total energy. [83,87,88] The most accurate reproduction of the results in this thesis arises when considering a reservoir-dependent relaxation, that accounts for energy relaxation induced by scattering between polaritons and free-carriers and excitons created by the nonresonant pumping.

2.5 Optical trapping

So far, the discussion of polariton condensates has not explicitly dealt with spatially non-uniform systems. Due to the interplay between multiple sources of nonlinearity and the gain provided by the nonresonant laser, spatially varying pump profiles can strongly affect the properties of the created polariton condensates. In this section, a basic review of the work done on this subject (by our group and others) is presented, starting by comparing condensates created by narrow and wide pump spots, and then considering what happens when multiple pump spots are used.

The simplest, experimentally relevant situation is that of a narrow, focused pump spot. This configuration intuitively leads to larger carrier densities and hence should show condensation at lower total laser powers. This, however, is not the case. The pump creates a large number of excitations in the semiconductor (e.g. free carriers, excitons, dark excitons) that interact repulsively with each other and with polaritons. This Coulomb repulsion causes a blueshift of the electronic energy levels at the positions on the sample where the pump is incident, and repels polaritons away from the pump positions. Condensates can then be formed with non-zero wavevectors, expands inside the cavity away from excitation spots and transforming potential- into kinetic-energy. [78,89] The formation of high-k condensates for the sample used in this thesis is shown in Figure 2.9. At the position of the nonresonant pump, two main features are seen in the emission: a hot polariton reservoir at the bottleneck and strong emission around the bottom of the dispersion. As one moves away from the excitation spot, the blueshift of the dispersion $\Delta(r)$ decreases due to the reduced carrier density,

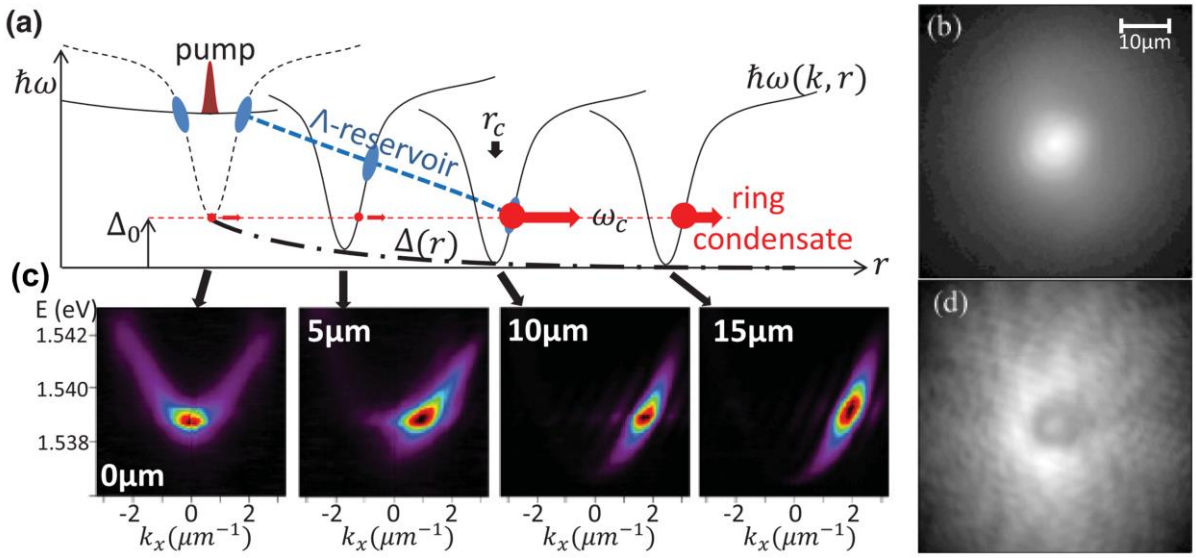

Figure 2.9 **Expanding condensates**. **(a)** Energy levels as a function of distance from pump spot. **(b)** Below threshold photoluminescence. **(c)** k-space image of polariton emission at different distances from pump spot. The condensate remains at the same energy but acquires higher wavevectors. **(d)** Above threshold emission showing a ring-shaped expanding condensate. Modified from [85]

simultaneously lowering the energy of the bottleneck and of the hot polariton reservoir. The strong polaritonic emission at the bottom of the dispersion, however, does not redshift. It is a coherent condensate that remains at the same energy as it moves away from the pump, transforming potential energy from the blueshift into kinetic energy at higher wavevectors. [85] This interplay between nonlinearity, energy relaxation and propagation is representative of the kinds of processes that need to be considered in the formation of polariton condensates. In this case, it leads to the emission above threshold having a distinct ring pattern (Figure 2.9d).

Many experiments use wider pump spots (~20μm) and condensation into high-k polaritons is not observed, forming instead in the $k\sim0$ ground state. [61,90,91] For such wide spots, the repulsion from the centre of the spot is not sufficiently large for propagation to occur. [78] Whether a condensate will form at $k\sim0$ or not also depends on the excitonic fraction of the polariton, with more photonic polaritons being able to more easily propagate through the sample and create high-k condensates. [91]

Finally, the effect of multiple pump spots is considered. Restricting the analysis to narrow pump spots, two regimes can be distinguished. In the limit of large separation between spots, polariton condensates are initially formed with independent wavefunctions each with their

own phase. As they expand and start to overlap, they synchronise and their phase difference becomes fixed. [92,93] This synchronisation appears in Figure 2.10b-d as interference fringes in the emission, and has recently been used as a classical simulator. [94] In the opposite limit of small separation between pump spots, high-k condensates may not necessarily be formed, being instead replaced by a trapped condensate (Figure 2.10e-i). These trapped condensates are created in the region in space between pump spots and are confined to this region. They have a much smaller overlap with the pump spots, lower thresholds, and narrower linewidths. The origin of the trapping can be attributed to the energetic potential landscapes created by the pumping. As mentioned before, the pumping creates a local blueshift of the polaritonic energy levels. If pump spots are placed sufficiently close to each other, this can create a potential minimum between laser spots with a depth of the order of ~800μeV. [95] It is in this potential minimum that polaritons get trapped and reach a sufficiently high density for condensation. Inside the trap, the condensate profiles match those of the textbook quantum modes of a potential well (Figure 2.10h,i). The first demonstration of such trapped states used

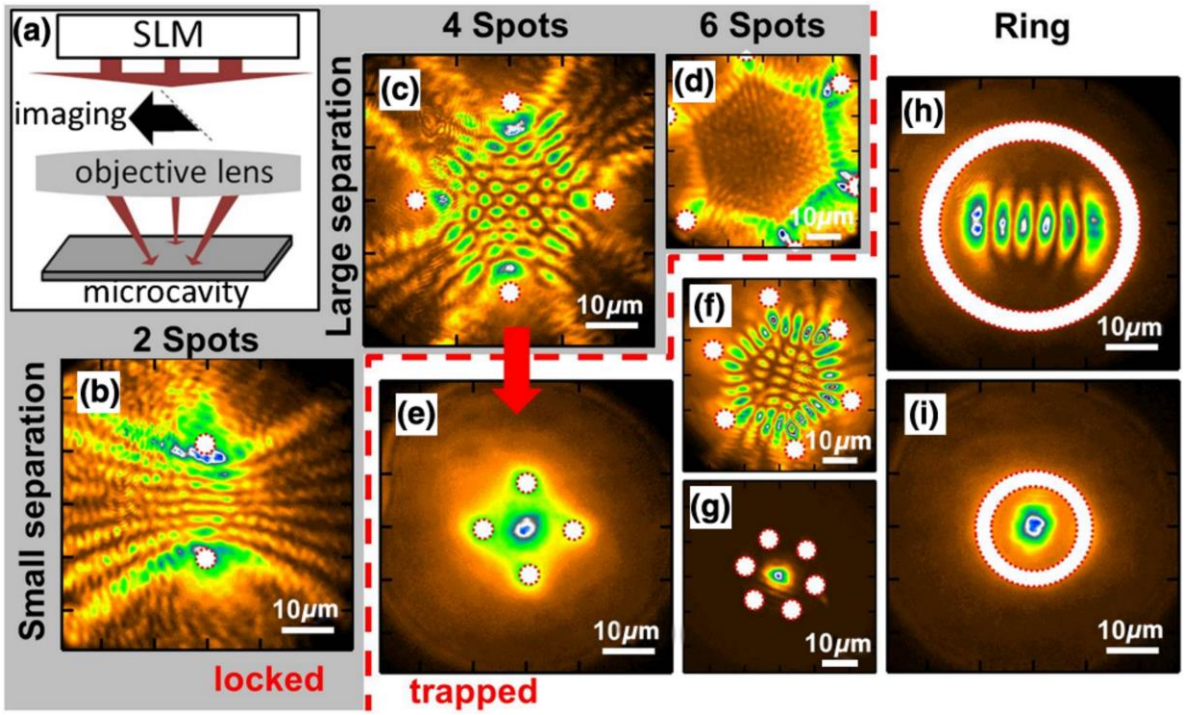

Figure 2.10 **Transition to trapped condensates**. **(a)** Setup for creating laser patterns. **(b-d)** PL for large separation between pump spots showing interference from the synchronisation of different untrapped condensates. **(e-i)** PL for small separation between pump spots showing trapped condensates in the (e,g,i) ground state and excited states (f,h). Taken from [86]

a single laser spot near a hard potential wall, [89] but recent experiments using all-optical potentials allows for more complicated potentials and condensates to be created. [86,88,95,96] This thesis will primarily focus on the properties of ground state trapped condensates created by this method.

It is also important to note that the trapping is not simply determined by the energy landscape but also by the gain landscape. In [97], a single, wide, top-hat pump spot was used to also observe trapped states. These are not trapped by an energy landscape but by a gain landscape, highlighting again the connections between polariton condensates and lasers. As in lasers, the mode profile can be determined by the gain profile, which is determined by the overlap with the excitonic reservoirs created by the pump. Hence polaritons do not necessarily condense at the lowest energy of the system, but at an optimal balance between low energy and high gain. [98]

Chapter 3 Methods

This chapter describes the experimental procedures and methods. The first section deals with the optical setup built as part of this PhD project. The second section contains the details of the microcavity samples used in experiments.

3.1 Experimental setup

A diagram of the final version of the setup built during this thesis is shown in Figure 3.1. Experiments were either done on this setup or in an equivalent setup built by P. Cristofolini, A. Dreissman and Dr. H. Ohadi. The setup consists of five sections:

1. **Pump laser preparation.** Experiments are done using a nonresonant laser (750nm) as a polariton pump. Some experiments also require the use of a resonant laser (800nm), e.g. to trigger spin switching (Chapter 7, Figure 7.3). Acousto-optic modulators (AOM) are used for beam-chopping and intensity control. An SLM is used to phase-imprint the nonresonant pump to create intensity patterns and a photodiode is used to monitor the SLM refresh rate (3.1.2). In addition to patterning the pump laser, the SLM is used for carefully selecting the focal plane of the pump light (Appendix A). Half- and quarter-wave plates are used for full control of the pump polarisation.
2. **Sample excitation and filtering.** NIR-optimised, long working-distance objectives are used to focus the pump lasers onto the microcavity and collect the polariton emission. The nonresonant laser is focused on the front of the microcavity, while the resonant one is focused on the back. Two front objectives are used interchangeably, with ×20, 0.4NA, WD=8.1mm Olympus LMPlan-IR (Chapter 6) and ×50, 0.42NA, WD=17mm Mitutoyo M Plan Apo NIR (Chapter 4, Chapter 5, Chapter 7) magnification. The back objective is a ×10, 0.28NA, WD=34mm Mitutoyo M Plan

Apo. The sample is kept inside a continuous-flow helium cryostat (Oxford Instruments Microstat), with temperature control and possibility of electrically contacting the sample. A long-pass dichroic mirror at near normal incidence (10°) is used to separate the pump light and the polariton PL (Sec. 3.1.1). A removable bandpass (THORLABS FBH800-40) filters the remaining laser light and low-energy emission from the GaAs substrate.

3. **k-space and Stokes components.** A removable 'k-space' lens allows measuring the far-field (if the lens is in place) or the near-field (if not). The following five beamsplitter cubes (BSC) allow simultaneous measurement of all Stokes components of the PL. The first cube splits the PL that will be resolved in the H-V basis when it reaches the polarizing beamsplitter (PBS). The HWP is placed at 22.5° to the vertical so that beam from the second cube is resolved in the D-A basis. Finally, the QWP is placed at 45° to the HWP axis leading to the PL being resolved in the σ_+-σ_- basis. All the cubes are mounted magnetically and can be removed without changing the beam alignment, so that any number of Stokes components can be measured at any time. In the case of a single polarisation being resolved, the last BSC can be replaced with a polarizing one so that no light is wasted. This is important, for example, in the single shot streak camera measurements of 5.1. For Chapter 7, the polarisation splitting is instead done with a Wollaston prism placed in front of the CCD. To perform accurate polarisation measurements, calibration is generally needed. This can be done by rotating the known polarisation of the input laser with a QWP and a HWP to extract the full Mueller matrix. In Chapter 4, this calibration was done by Hamid Ohadi and Alexander Dreismann, while in the following chapters, the polarisation is only split into a single component and hence calibration only required the placement of a ND wheel (THORLABS NDC-25C-2) in the reflection of the PBS which balanced the reflected and transmitted beams.
4. **Phase interferometry.** To measure the spatial coherence of the emitted light, two types of interferometers are used: a Mach-Zender (shown in Figure 3.1) or a Michelson. The Mach-Zender is simple to set up and the results easy to interpret. It relies on magnifying part of the emission to provide a constant phase reference across the field of view, so that changes in phase can easily be seen in the interference

fringes. In practice, achieving a truly flat phase reference is surprisingly tricky and removing the slow phase variation requires relatively complicated data analysis. A Michelson interferometer with a retro-reflector in one arm is slightly harder to set up but provides data that is easier to analyse.

5. **Detection.** Flipper mirrors allow the sample PL to be recorded by three different measurements. Firstly, it can be time-resolved onto PMTs (Hamamatsu H10720-20 recorded on TeledyneLecroy WaveSurfer 10, ~1ns resolution) or a streak camera

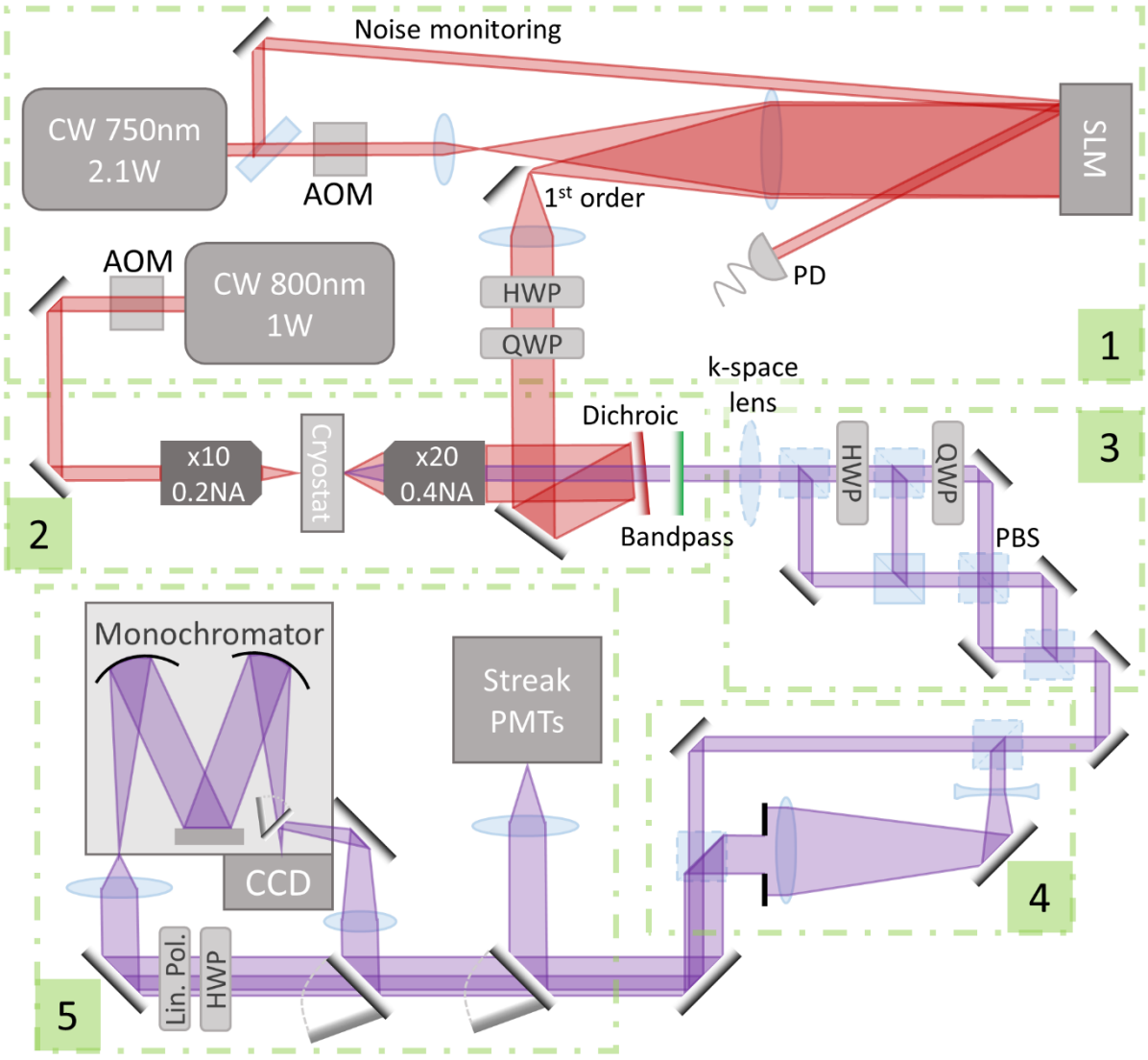

Figure 3.1 **Simplified beam path**. Removable components are dashed. The first mirror and other beam-steering mirrors (not shown) are dielectric to maximise reflection. The mirror before, and all after, the dichroic are silver mirrors to minimise polarisation scrambling.

(Hamamatsu C5680, 2ps resolution). For streak measurements, a cylindrical lens is used to further focus the light onto the slit to achieve maximum signal. Secondly, 2D images of the near-field or far-field can be recorded directly on a CCD (Andor Newton 971). Finally, a 4f monochromator (Triax550, 1200lines/mm, 60μeV resolution) can be used to measure the polariton spectra, again in either near- or far-field. For ease of alignment, not all experiments matched the input NA of the spectrometer, leading to reduced resolution (~70μeV). The HWP and linear polariser in front of the spectrometer ensure that the light is polarised vertically, as required.

3.1.1 Technical details

Lasers. Two different Ti:sapphire lasers were used in this thesis, for both resonant and nonresonant experiments: a Coherent MBR driven by a V10 Verdi (1.5W at 750nm), and a MSquared SolsTiS driven by a Quantum Finesse Pure (2.1W at 750nm). It is crucial for the nonresonant pump to be single mode. Condensate trapping [86,95] can still be performed with a multi-mode pump, but multiple trapped polariton modes are occupied instead of one. Such multimode operation breaks down the spin physics discussed in this thesis, so ensuring single-mode operation is crucial. The SolsTiS easily operates in a single-mode for long periods of time (days) thanks to internal locking electronics. The MBR is not as stable and often shows multi-mode lasing. To correct for this, the mode profile was monitored with a Fabry-Perot resonator (THORLABS SA200-5B, 1.5 GHz), manually adjusting the laser to ensure single-mode operation.

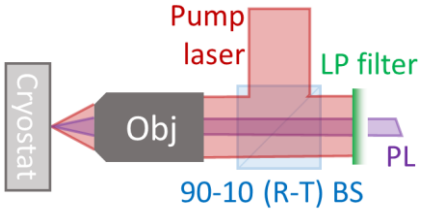

Figure 3.2 Typical experimental setup

Dichroic filter. Although Figure 3.1 shows a dichroic (FF700-Di01 Brightline Semrock) being used to separate the nonresonant pump from the polariton PL. This setup was only used for Chapter 6. The rest of the chapters used a 90-10 BSC and a long-pass filter instead (Figure 3.2). The problem with the latter design (which is standard in polariton experiments) is that the BSC gives a slight phase difference between the s- and p-polarisation directions upon reflection. Hence, if the linearly-polarised pump is not polarised along these axes, it will become slightly elliptical after the BSC. Since trapped polaritons are incredibly sensitive to

pump ellipticity (Chapter 6), minimising this ellipticity is crucial. The dichroic at near-normal incidence does precisely that. Additionally, using the dichroic allows one to use all the pump laser power and detect all of the polariton PL, without wasting 90% of one or the other.

Polarisation optics. As just discussed, BSCs are polarisation sensitive on reflection. Hence, careful arrangement of the polarisation splitting optics must be made for accurate Stokes measurements (section 3 in Figure 3.1). The order of the BSC and waveplates is such that whichever basis is going to be resolved by the PBS (H-V, D-A or σ_+-σ_-) is not scrambled by reflections. This is achieved by ensuring reflections with only s- or p-polarised light.

Sample positioning. Imperfections during MBE growth mean that the sample is not spatially uniform. The polariton energy, emission, and condensation threshold vary across the sample

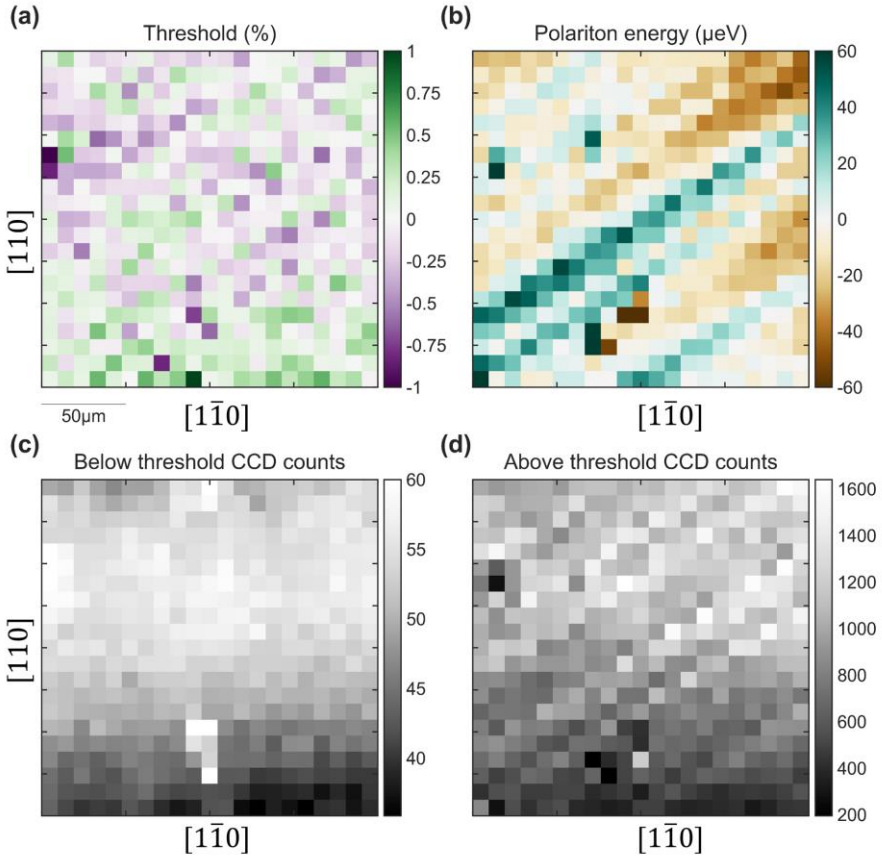

Figure 3.3 **Spatial disorder**. **(a)** Percentage variation in the condensation threshold power. **(b)** Polariton energy at k=0. Polariton emission **(c)** below threshold ($0.1P_{th}$) and **(d)** above threshold ($1.8P_{th}$). The disorder is spatially structured, and there are striations along the sample that have different energy and emission above threshold. The threshold itself and the emission below it do not seem to be affected by these defects.

(±50ueV, ±50% and ±1%, respectively in Figure 3.3). Hence the microcavity needs to be carefully positioned to ensure reproducibility. To do this, the cryostat is mounted on a 3-axis translation stage (Figure 3.5). The combined weight of the cryostat and He transfer tube is larger than the stage specifications allow, but repeatable positioning down to a few μm is still achieved.

Focusing. Accurate positioning of the microcavity at the focal plane of the objective (for collection) and the SLM (for pumping) is crucial. A few μm offset from the focal plane can lead to a change in the handedness of the polariton emission polarisation (Figure 3.4a), even if the intensity changes by only ~20% (Figure 3.4b), and the shape of the condensate in real-space does not change noticeably. The reason for the polarisation being so sensitive to the focal plane position is that birefringence changes in the focus lead to the pump light hitting the cavity surface at an angle, and TE-TM splitting causes the initial polarisation to precess. Such changes to the pump polarisation strongly influence the polarisation of the condensate (Chapter 6). The translation stages are unable to provide the level of accuracy required for reproducible positioning of the sample at the focal plane. However, small adjustments to the focal plane of the pump light can be made with the SLM, improving accuracy and reproducibility (Appendix A).

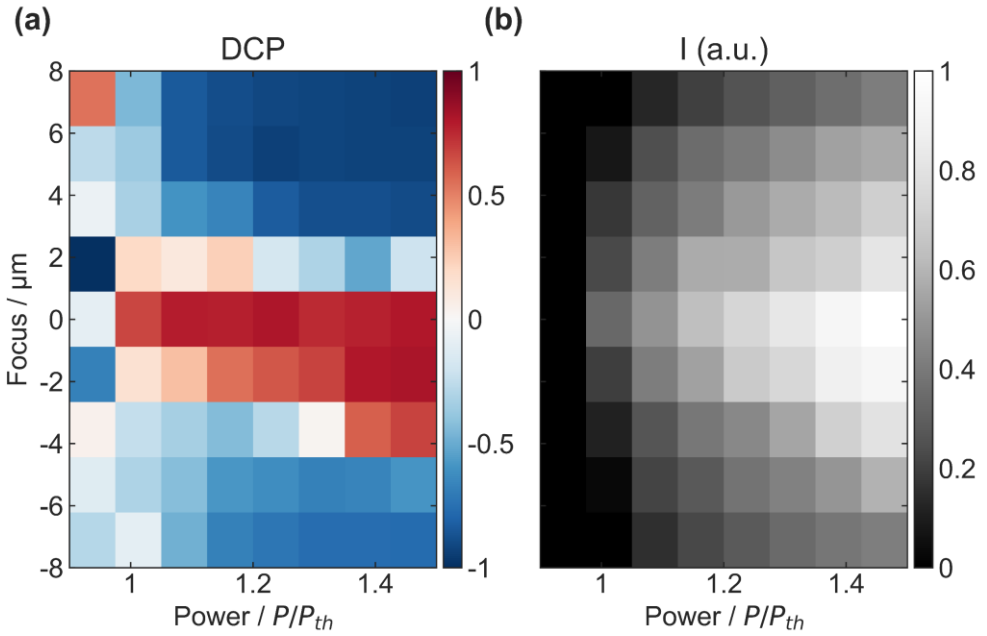

Figure 3.4 **Focusing**. **(a)** Degree of circular polarisation (DCP) and **(b)** emission intensity (I) of an optically trapped condensate as a function of offset from the focal plane and pump power.

Alignment. To minimise birefringence due to TE-TM splitting, it is necessary to ensure the sample is perpendicular to the microscope objective. The simplest way of doing this would be to rotate the cryostat, but the heavy torque on the cryostat holder prevents accurate angular positioning. Instead, the objective is mounted on a four-axis stage (x-y and tip-tilt). This slightly complicates the alignment procedure but ensures reproducibility (Appendix A).

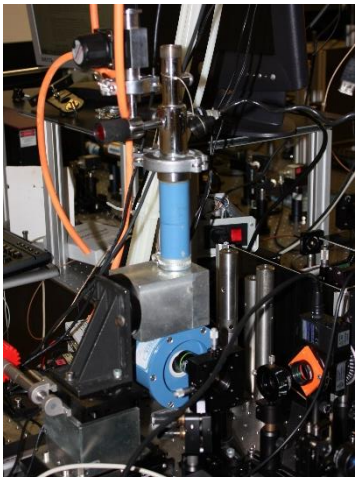

Figure 3.5 Cryostat and objective mounts

Automation. A major component of this PhD was devoted to fully automating the data acquisition and analysis to ensure reproducibility and repeatability. A Python suite was developed based on nplab (https://github.com/nanophotonics/nplab) for interactive data acquisition and analysis. The AOMs, SLM, waveplates, filters, flipper mirrors, sample positioning and focusing, and data taking with CCD, streak camera and PMTs, are all computer controlled. This allows for larger, consistent datasets to be recorded revealing new physics.

3.1.2 Spatial light modulation

Phase-only SLMs are very flexible tools and can reproduce the behaviour of many optical elements: a quadratic phase is equivalent to a spherical lens, a linear phase in one direction is a mirror/grating, a radially linear phase is an axicon, etc. Three liquid-crystal, phase-only spatial light modulators were used in this thesis: a BNS P512-0785 (Chapter 4, Chapter 5, Chapter 7), a HOLOEYE HEO1080 and HOLOEYE LC-R 2500 (Chapter 6). They have different resolutions (512×512, 1920×1080 and 1024×768 respectively), but are all able to produce sufficiently high-quality laser patterns for the experiments.

Despite their usefulness, SLMs present a few practical problems. The first problem is that, of all the incident light on the SLMs, only 60-70% is phase modulated. The rest of it is simply reflected and needs to be filtered. To achieve this, a linear offset is added to all patterns, spatially separating the modulated and unmodulated beams (Figure 3.6). This offset is

equivalent to a grating so the modulated and unmodulated beams tend to be called the 1st and 0th order, respectively. [99]

The second problem is calibration: finding out how much voltage needs to be applied to the liquid crystal to provide a pre-determined phase. The HOLOEYE models have an approximately linear relationship between voltage and phase, and can be easily calibrated by optimising the power of the modulated beam. The BNS model requires a more complicated calibration that was done by P. Cristofolini and A. Dreissman.

The third problem is that slow refresh rates lead to intensity oscillations in the modulated pattern. Although this does not affect the BNS model significantly, the HOLOEYE models have oscillation amplitudes of ~15-30% at 0.3-1kHz. This complicates how experiments are done. First, the pulse width used to pump the polariton condensates are kept short (<10μs), so each condensate effectively feels a constant laser power. And second, the SLM power oscillations are monitored with an additional laser beam (Figure 3.1). This signal is then used to synchronise the data taking, reducing power variations to <5%.

Algorithms

To create laser patterns using a phase-only SLM, one needs to solve the phase retrieval problem, i.e. what phase needs to be applied to a known input field $A_{in}(x,y)e^{\phi_{in}(x,y)}$ to get a specified amplitude $A_{out}(x,y)$ in the Fourier plane? There is no analytical solution to this problem and a common approach is to use iterative Fourier transfer algorithms (IFTA). [100] A schematic representation of how these algorithms work is shown in Figure 3.7, where it is assumed that $\phi_{in}(x,y) = 0$. There are many different IFTA [100,101], each with different advantages and disadvantages. The common trade-off in these algorithms is between efficiency – how much of the total light goes into the desired target – and smoothness (η in Figure 3.7). Given the spatial variations of PL energy and intensity, smoothness

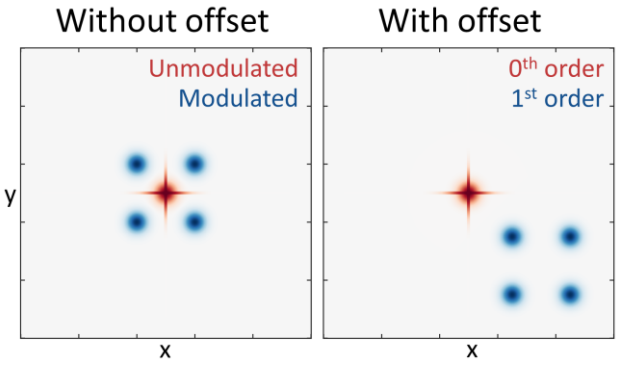

Figure 3.6 **SLM offset.** Adding a linear offset to a 4-spot phase pattern separates it from the unmodulated 0th order.

was not critical, and algorithms with 50-70% efficiency could be used. It was found that the mixed-region amplitude freedom algorithm (MRAF) [102] had the right balance of smoothness, efficiency, computational cost and flexibility.

The laser patterns used in this thesis are relatively simple geometric arrays of a small number of diffraction-limited spots (Figure 3.8). Hence, further improvement on the MRAF algorithm was made by using single-pixel targets (Figure 3.8a). This means that $|A_{out}|$ is only non-zero at isolated pixels centred around the desired location of the laser spot. This approach gets rid of the problem of vortex nucleation during the algorithm's iteration [101], but brings a new problem: the positioning of the laser spots is now discrete. This becomes an issue when fine control is needed over the polariton trap size (Chapter 5) or the distance between trapped

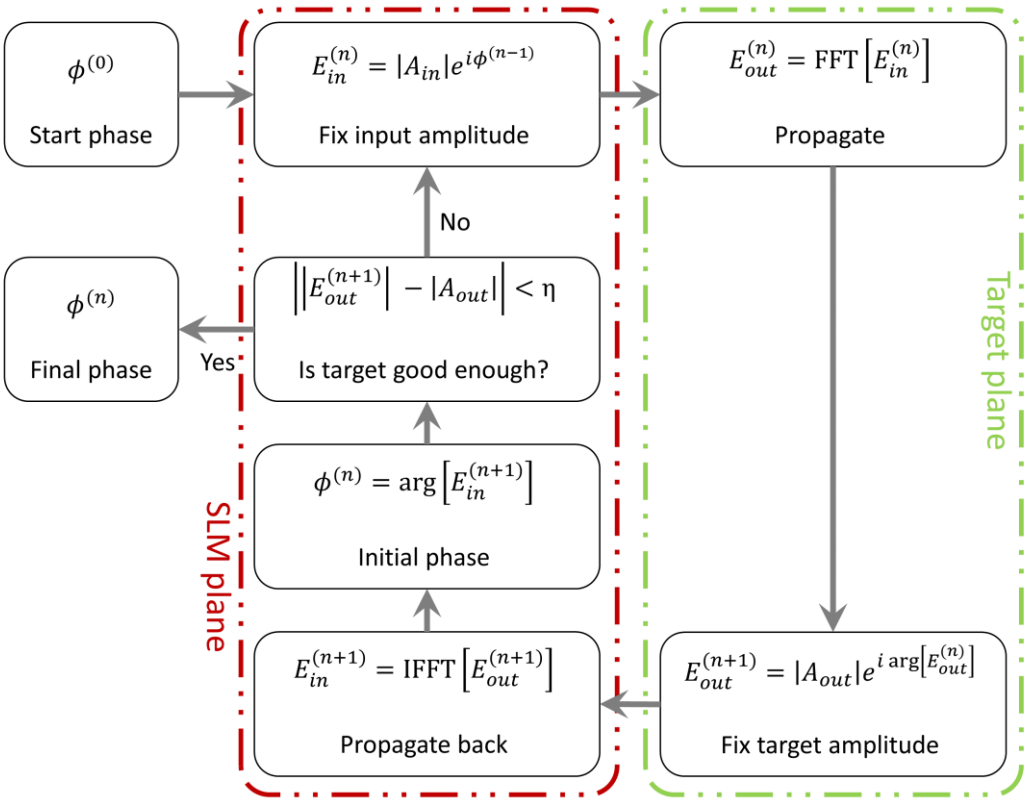

Figure 3.7 **Basic IFTA principle**.The starting point is a given input field with flat phase and amplitude $|A_{in}|$. An initial guess phase $\phi^{(0)}$ is imprinted on this field which, after propagation, leads to an output field $E_{out}^{(n)}$. The phase of this field is kept (phase freedom), while its amplitude is replaced by the desired target pattern A_{out}. This new field $E_{out}^{(n+1)}$ is propagated back to the SLM plane $E_{in}^{(n+1)}$, where again the phase is kept and the amplitude is replaced with A_{in}. This is repeated until convergence (~30 iterations for this thesis).

condensates (Chapter 7). In those chapters, a different method was used to calculate the SLM phase. Starting from the calculated MRAF laser field $E_{out}^{(n)}$, and using the amplitude A_i and phase φ_i of this field at the laser spot positions $\left(k_x^{(i)}, k_y^{(i)}\right)$ the SLM phase was set to be:

$$\phi(x,y) = \arg\left[\sum_i A_i e^{-i(k_x^{(i)}x + k_y^{(i)}y + \varphi_i)}\right]$$

where the difference with MRAF is that $\left(k_x^{(i)}, k_y^{(i)}\right)$ can take any continuous value without compromising on the pattern quality.

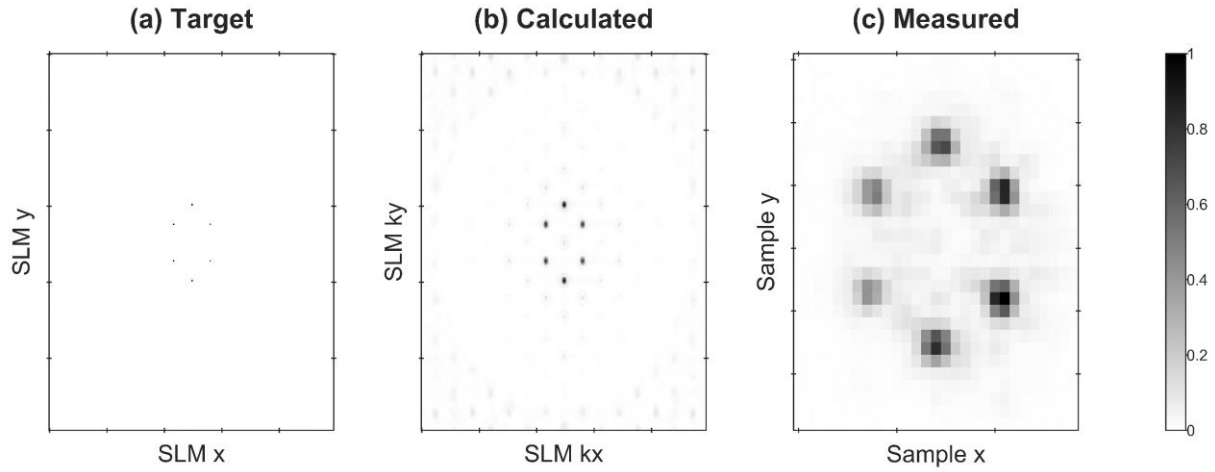

Figure 3.8 **Hexagonal MRAF patterns. (a)** Single-pixel target pattern $|A_{out}|$. **(b)** Optimised pattern with MRAF $\left|E_{out}^{(n)}\right|$ **(c)** Laser reflection measured on the CCD

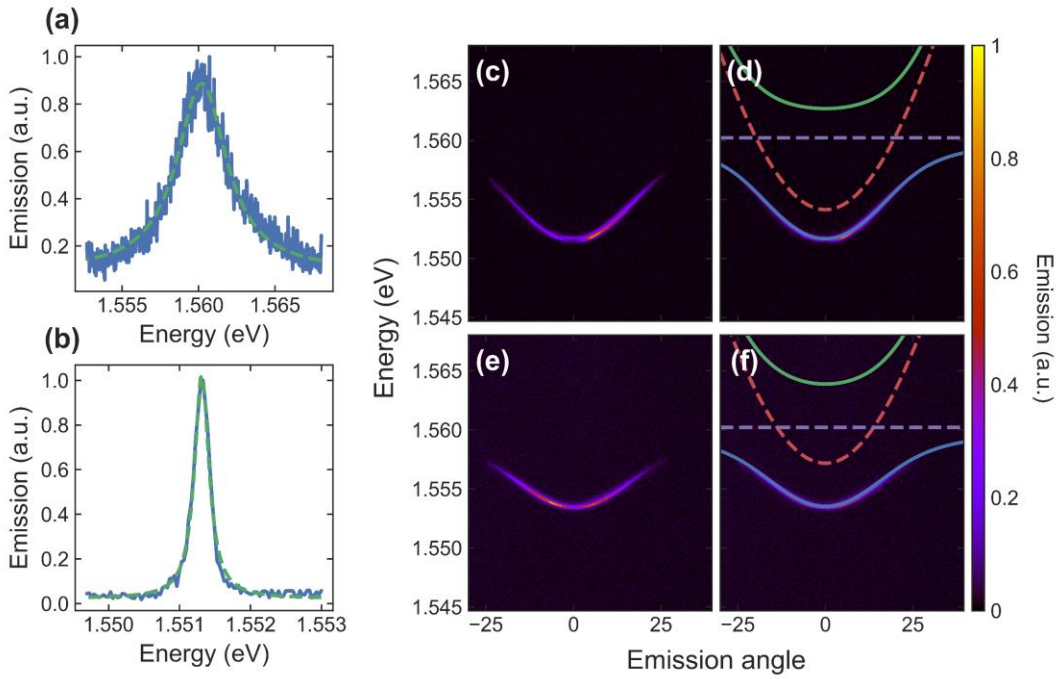

Figure 3.9 **Oscillator model fit. (a)** Exciton emission. **(b)** LP emission at k=0. **(c)** Measured dispersion at −6meV detuning and **(d)** fitted model. **(e)** Measured dispersion at −3meV and **(f)** fitted model

3.2 Samples

A cross-section through the semiconductor structure[2] is shown in Figure 3.10. A 5λ/2 cavity ($Al_{0.3}Ga_{0.7}As$) is sandwiched between two distributed Bragg reflectors (DBRs) formed by 32/35 layer pairs on the top/bottom. Each individual layer pair is composed of 57.2nm of $Al_{0.15}Ga_{0.85}As$ and 65.4 nm of AlAs. The quality factor of the microcavity is ~16,000, leading to polariton lifetime of >7ps. Four sets of three 10nm GaAs QWs (separated by 10nm of $Al_{0.3}Ga_{0.7}As$) are placed at the cavity anti-nodes. The exciton-photon detuning varies from +2 to -10meV, and experiments were done at a detuning of -5meV unless otherwise noted. The substrate is n^+ doped GaAs. A detailed study of polariton condensation and transition to weak coupling under nonresonant pumping in this structure can be found in [22].

The excitonic PL peak is shown in Figure 3.9a, with an energy of 1.5602eV and a linewidth of 2meV. The lower polariton mode has a linewidth of 100μeV (Figure 3.9b). We manually

[2] The microcavities were MBE grown and processed in the group of P. Savvidis at the University of Crete.

fit the oscillator model to multiple sample positions with different detunings, of which two are shown in Figure 3.9: 6meV (c,d) and 3meV (e,f). This gives a Rabi splitting of 9meV, and a photon mass of $1.2e^{-5}m_o$, where m_o is the free electron mass.

Three samples were studied in this thesis, having the same underlying structure, but being post-processed differently:

- **Strip sample**. This was an unprocessed sample, used to check the post-processing did not affect the observed physics.
- **Membrane sample** (Figure 3.10a). The GaAs substrate used for crystal growth is opaque at the polariton energy, preventing optical access to the microcavity from both sides. To get around this, sample was glued on another substrate and thinned down by mechanical polishing to ~250μm. Then circles with a diameter of 300μm are photolithographically defined onto the substrate, followed by reactive ion etching. This etching is highly sensitive to the Al concentration, and stops when it reaches the first AlAs DBR layer. Both steps combined creates suspended 300μm-wide membranes, that can be optically accessed on both sides. Apart from electrical measurements, all data in this thesis was taken on this sample.
- **Electrically-contacted sample** (Figure 3.10b). This sample was designed to be able to apply electric fields perpendicular to the QW. In this case, the substrate is not

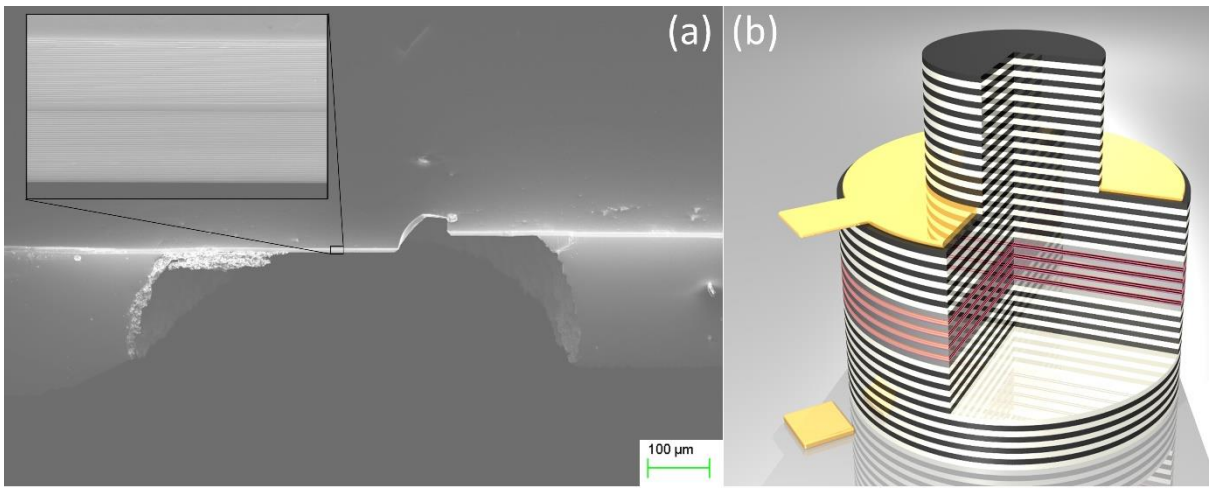

Figure 3.10 **Sample structure**. **(a)** SEM of sample edge. The substrate has been etched to create a membrane. **(b)** Diagram of the electrically contacted sample

polished and the etching is divided into two steps. First, an annular recess (inner diameter 100μm, outer diameter 200μm) is defined on the top DBR, etching most of the DBR down to the last 4 layer pairs before the QWs. A Shottky contact is deposited on this recess (20nm Ti, 200nm Au). Then, the sample surrounding this recess is etched further, through the QWs, creating something like what is seen in Figure 3.10b. Finally, an Ohmic contact (5 layer pairs of 10nm Au and 20nm Ge) is deposited onto the substrate, allowing us to apply electric fields across the QWs.

Chapter 4 Spontaneous spin bifurcation

This chapter explores the spin properties of optically trapped polariton condensates.[3] While untrapped condensates are either unpolarised or linearly polarised, trapped condensates are typically linearly polarised just above the condensation threshold. At higher powers, the condensate is found to become elliptically polarised and bistable: the handedness is chosen stochastically upon formation. This symmetry-breaking transition is termed here a spin bifurcation. Increased overlap with the exciton reservoirs is shown to make this effect disappear, explaining why it has not been observed previously.

Possible explanations for these effects are explored, and it is concluded that it arises due to splitting in the energy and dissipation of two linearly polarised modes, with the higher energy mode having the longer lifetime. Experimental results are well reproduced by a zero-dimensional mean field model based on Gross-Pitaevskii equations for the polariton wavefunction. The spin bifurcation occurs due to the interplay between the small linear-polarisation splittings and the spin-asymmetry of the polariton-polariton nonlinearities. A close analogy with self-trapping in a two-mode system is demonstrated.

Finally, externally applied electric fields are used to control the spin of the condensate. Two different experimental results are presented and are well reproduced by simulations. First, the linear-polarisation splitting is found to be linearly proportional to the applied electric field. Hence, the condensate spin can be tuned by the applied voltage. Second, voltage-induced birefringence can cause the pump light to be slightly circularly polarised, externally breaking the parity-symmetry and fixing the handedness of the condensate. The transition between oppositely-handed condensates is found to be hysteretic and is used to demonstrate an electrical spin switch.

---

[3] Part of the work presented here has been published in [103,104]. Experimental work was undertaken by Dr. H. Ohadi and A. Dreismann, while simulations and modelling were done together with Y. Rubo

4.1 Stochastically magnetised condensates

Linearly-polarised, nonresonant excitation of a semiconductor microcavity produces equal densities of spin-up and spin-down excitons. Free-energy minimization predicts that the polariton condensate formed from such a spin-balanced exciton cloud should have linear polarisation, with the direction of the linear polarisation randomly chosen. [105–107] While this behaviour has been seen in bulk GaN samples, [64] most samples support steady-state condensates that have linear polarisation pinned to the crystal axes by strain. [26,61,62,108,109]

In contrast with this, optically trapped polariton condensates can develop strongly circular polarisation under linearly-polarised pumping (also see 4.2.2). A typical trapping scheme can be seen in Figure 4.1a, where the laser pattern is formed by 4 diffraction-limited spots

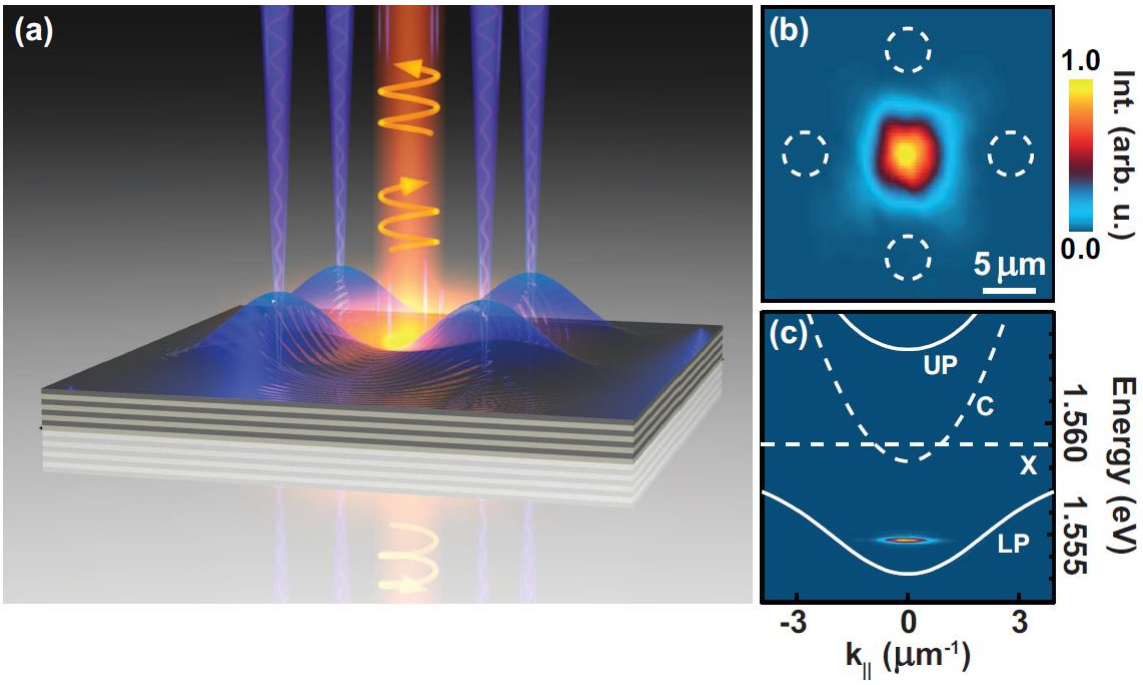

Figure 4.1 **Optically trapped condensates**. **(a)** Four nonresonant beams (blue) create exciton clouds that blueshift the energy levels and trap the condensate emission (orange). The condensate is either right- or left-circularly polarised. **(b)** Spatial image of the condensate emission. The pump light is spectrally filtered and is located on the dashed, white circles. **(c)** Dispersion relation of cavity (C), exciton (X) and upper and lower polaritons (UP/LP) at -1meV detuning. The condensate emission is blueshifted from the LP line but still ~5meV below the exciton line. The emission is flat along the k-axis because of the trapping. Taken from [103]

arranged in a 15μm-side square. The experimental results of this chapter were measured on the membrane sample (Sec. 3.2) at 4K. The detuning between the cavity and the exciton was -1meV (Figure 4.1c). Nonetheless, the results presented are general and similar results have been obtained with hexagonal trapping patterns, with different separation between the laser spots (from 8μm to 16μm), at different temperatures <15K, in regions with different detuning (from +2meV to -10meV) and on different samples. Note however, that the circularly polarised states disappear if the nonresonant laser pump is not single-mode. The likely cause for this are the large intensity oscillations on GHz timescales coming from multimode interference. Further work is needed to study the influence of such intensity noise on the condensate polarisation but for the rest of the thesis single-mode pumping will be assumed. Additionally, in many sample positions, changes in the direction of the linear polarisation can lead to only one of the circularly polarised solutions being observed. This is particularly the case with 90-10 beamsplitter used in this chapter (Figure 3.2), where a deviation of a few degree in the linear polarisation is enough to break the symmetry. This is due to birefringence (mostly in the cube, but also from the objective and the sample) which causes the linear polarisation to turn slightly circular. When using a dichroic filter at normal incidence (Figure 3.1), this birefringence is reduced, and at most sample positions, the linear polarisation can be rotated by $\pm 10^{o}$ without significant changes to the condensate spin.

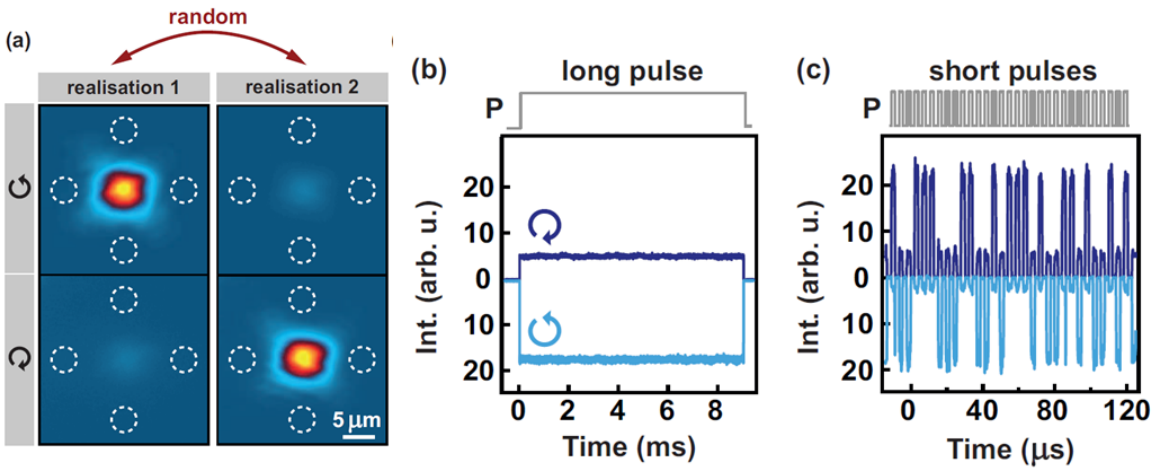

Figure 4.2 **Polarisation-resolved emission**. **(a)** Spatial images of the two elliptically-polarised states. Dashed white circles indicate the position of the pump laser spots. **(b)** PMT traces of the circular polarisation components for a 9ms pump pulse (pump profile shown on top). **(c)** same as (b) but for a train of 2μs laser pulses. Modified from [103]

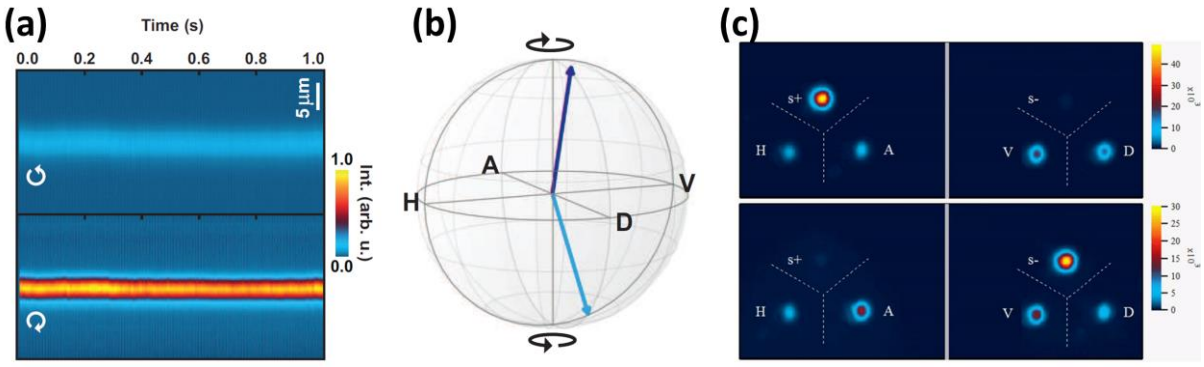

Figure 4.3 **Condensate stability and ellipticity. (a)** Spatially resolved emission as a function of time, showing that the spin state can be retained over a second. **(b)** Poincare sphere and **(c)** CCD images of all three polarisation components of the two polarisation states showing they are not fully circular but have a small linear polarisation component correlated with the handedness. (a) and (b) are modified from [103]

The polarisation resolved images of the trapped polariton condensate can be seen in Figure 4.2a. The condensate has a strong degree of circular polarisation ($0.6 < |s_z| < 0.95$) and it stochastically develops either right- or left-handedness every time the condensate is created. These two states are associated with a defined exciton spin, with right-circularly polarised emission corresponding to a spin-up condensate. Hence the stochastic formation of right- or left-handedness corresponds to a spontaneous development of magnetisation of the excitonic part of the polaritons. In this sense, the condensate is *magnetised*.

While circularly polarised condensates have been observed before, the stochastic formation into states with opposite handedness has not been seen. Generally, the handedness of the polarisation has been fixed either by external factors like pumping handedness [75,110–112] and magnetic fields [113–115] or by internal energy splittings like TE-TM [24,116]. There have been experiments showing that the condensate can form in an elliptically polarised state at short timescales [108], and theoretical work predicting that this circular polarisation should remain in the absence of spin relaxation. [106] But the degree of circular polarisation in these works is a continuum of values, in contrast with the two discrete states observed here.

The formation of these states is truly random. Trains of pulses, whether long (Figure 4.2b) or short (Figure 4.2c), show no correlation in the handedness between consecutive condensates. This remains the case up to the shortest pulses tested (500ns). Once formed, however, the condensate can retain the polarisation for seconds, eleven orders of magnitude longer than the polariton lifetime (Figure 4.3a). Importantly, the two polarisation states are not fully

circularly polarised and retain some linear polarisation (Figure 4.3b-c). Both the ratio of the linear-to-circular components and the direction of the linear polarisation vary with position along the sample surface.

These observations point towards a spontaneous symmetry breaking in the system. The initial state – a linearly polarised laser – has no handedness, yet the final state – the condensate – does have a defined handedness. This symmetry breaking is independent from sample position, trap shape, and exciton-photon detuning.

4.1.1 Reservoir density dependence

Given the robustness of the observed symmetry breaking, the fact that it has not been observed in previous experiments using similar samples is intriguing. The reason for this is that most studies have not looked at *optically trapped* condensates, where the condensate and the exciton reservoir are spatially separated and condensates have narrower linewidths. [110] Externally creating an additional exciton reservoir on top of the trapped condensate strongly decreases the observed circular polarisation (Figure 4.4), and the typically observed linear polarisation is recovered. This additional nonresonant laser spot is linearly polarised and its power is less than 2.5% of the total pump power. It is sufficiently weak that it produces no observable blueshifts or changes to the trapping potential, yet it clearly strongly decreases the

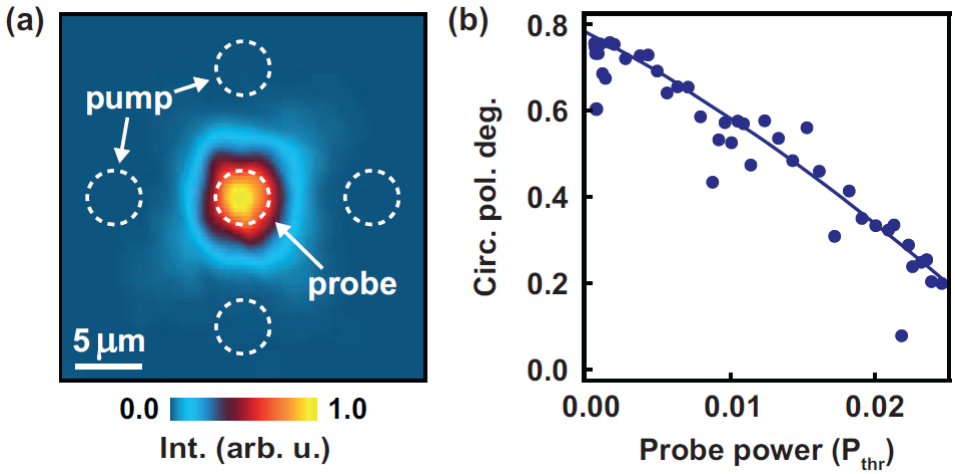

Figure 4.4 **Influence of reservoir overlap. (a)** Spatial image of the condensate emission. White dashed circles indicate the position of the nonresonant pump and probe. **(b)** Average degree of circular polarisation as a function of probe power. Taken from [103]

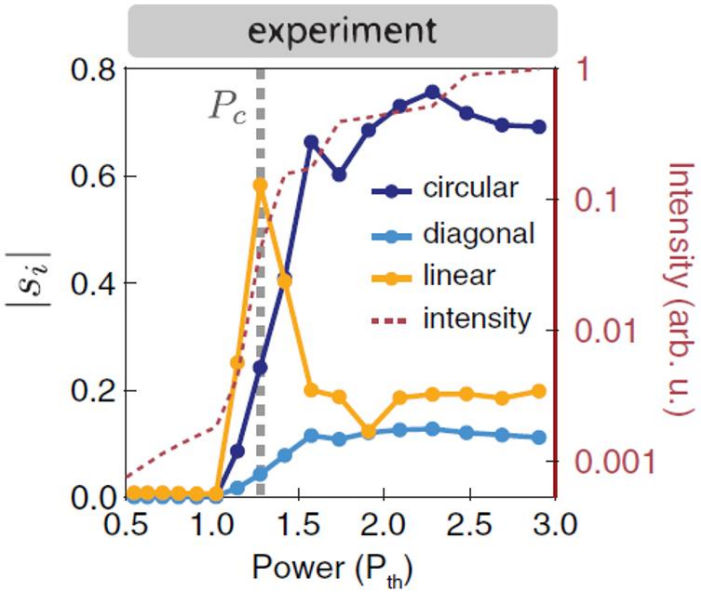

Figure 4.5 **Power dependence** of the three polarisation components ($s_{x,y,z}$) and condensate intensity. Immediately after threshold there is a fast increase of linear polarisation, followed by a second threshold (P_c) after which the circular polarisation grows. Taken from [103]

degree of circular polarisation (Figure 4.4b). A possible explanation for this is the increase of free-carrier scattering and consequent reduction of spin relaxation. [117]

In addition to the dependence on the spatial overlap with the reservoir, the condensate polarisation also strongly depends on the exciton reservoir density (i.e. nonresonant laser power). Below threshold (P_{th}), the PL is unpolarised (Figure 4.5). Immediately after the threshold, the condensate polarisation is linear, as in previous literature. However, as the density is increased passed a second threshold ($P_c \sim 1.2P_{th}$), the linear polarisation decreases and the circularly polarised states emerge.

4.2 Single-mode mean-field model

The previous section demonstrated the stochastic build-up of circular polarisation in trapped polariton condensates, and how they are affected by exciton reservoir density and spatial overlap. However, no explanation for why the condensates might stochastically magnetise has been presented. Here, two possible scenarios are discussed and rejected before developing the most likely explanation: a spin bifurcation.

The first possible explanation comes from considering stronger nonlinear interactions between cross-spin polaritons than between co-spin polaritons ($\alpha_2 > \alpha_1$). In this situation, the free energy is minimised when all the polaritons are in the same spin state, leading to spontaneously magnetised condensates under spin balanced pumping. There are four reasons why this explanation is incorrect. Firstly, energy minimisation arguments apply only to condensates in equilibrium, which is not the case here. [118] Secondly, if $\alpha_2 > \alpha_1$ one would expect to get *fully* circularly polarised condensates at *all powers* above threshold, which contradicts our observation of a linearly polarised condensate evolving into elliptically polarised condensates at a second threshold. Thirdly, if $\alpha_2 > \alpha_1$, then untrapped condensates should also be circularly polarised, which is not the case. Finally, and most importantly, it is well established that cross-spin interactions are weaker (and usually the opposite sign) than co-spin interactions. [105,119,120]

The second explanation requires one to consider increased loss in the presence of opposite spin polaritons. Biexciton formation has been proposed as a microscopic mechanism that could produce such cross-spin saturation, [48,119–121] and even very weak losses could lead to circularly polarised states. This process, however, would be expected to strongly depend on detuning, with stronger losses occurring for condensate energies close to the biexciton energy. Given that the magnetised condensates presented here appear over a large range of detuning (+2 to -10meV), it is highly unlikely that biexciton formation is the underlying physical explanation.

The final scenario is that of a *spin bifurcation*, where the magnetised condensates emerge from the interplay of the polariton nonlinearity spin-asymmetry with energy and dissipation splitting of linearly polarised polaritons. It is a specific case of the theory of *weak lasing*, [122–124] where nonlinear bosonic modes with different losses can spontaneously synchronise and break time-reversal symmetry. The rest of this section justifies the description of magnetised polariton condensates in terms of a spin bifurcation, by first comparing the experimental results with a mean-field Gross-Pitaevskii model; then discussing the evidence of splitting of the linear polarisation modes; and finally developing a physically intuitive picture and a connection to self-trapping.

4.2.1 Gross-Pitaevski equations

The spin bifurcation theory of optically trapped condensates is a mean-field model where a spinor order parameter (spin-up $\psi_\uparrow$ and spin-down $\psi_\downarrow$) is used to describe the polariton condensate (Chapter 2). Since the condensate is always in the lowest mode of the trap, all spatial dimensions are ignored and the evolution of the order parameter is given by:

$$\begin{aligned}\frac{d\psi_\uparrow}{dt} &= \left[\frac{1}{2}\left(R\,n - \Gamma_p\right) - \frac{i}{2}\left(\alpha_1|\psi_\uparrow|^2 + \alpha_2|\psi_\downarrow|^2\right)\right]\psi_\uparrow - \frac{1}{2}(\gamma - i\,\varepsilon)\psi_\downarrow \\ \frac{d\psi_\downarrow}{dt} &= \left[\frac{1}{2}\left(R\,n - \Gamma_p\right) - \frac{i}{2}\left(\alpha_1|\psi_\downarrow|^2 + \alpha_2|\psi_\uparrow|^2\right)\right]\psi_\downarrow - \frac{1}{2}(\gamma - i\,\varepsilon)\psi_\uparrow \\ \frac{dn}{dt} &= P - \Gamma_x - R(|\psi_\uparrow|^2 + |\psi_\downarrow|^2)n\end{aligned} \tag{4-1}$$

where n is the exciton reservoir density, R is the feed rate from the reservoir to the condensate, $\Gamma_{p/x}$ are the polariton and exciton decay rates, $\alpha_{1/2}$ are the same-spin and opposite-spin polariton-polariton interaction constants, and the ground state energy of $\psi_{\uparrow/\downarrow}$ is normalised to zero. The last term in the evolution of the wavefunction corresponds to splitting in energy (ε) and dissipation (γ) between two linearly polarised modes (Sec. 4.2.2). For simplicity, the splitting is assumed to be between a vertically polarized state (V) with energy $+\varepsilon/2$ and dissipation $\Gamma_p - \gamma$; and a horizontally polarised state (H) with energy $-\varepsilon/2$ and dissipation $\Gamma_p + \gamma$. The model can be trivially generalised to account for splittings along arbitrary axes (Sec. 4.3).

The pseudo-spin vector is a useful way of describing and visualising the system, as it directly corresponds to the Stokes polarisation components measured experimentally. It is defined as $S_i = \sigma_i \Psi$, where $i = \{x, y, z\}$, σ_i are the Pauli matrices and $\Psi = \{\psi_\uparrow, \psi_\downarrow\}$ is the condensate spinor wavefunction. The magnitude of the pseudo-spin vector is S. Applying the static reservoir limit to Equation (4-1) (see Sec. 2.4.1) and rewriting in terms of pseudo-spin components:

$$\begin{aligned}\dot{S_x} &= -g(S)S_x - \gamma\, S - \alpha\, S_z\, S_y \\ \dot{S_y} &= -g(S)S_y + \varepsilon\, S_z + \alpha\, S_z\, S_x\end{aligned} \tag{4-2}$$

$$\dot{S}_z = -g(S)S_z - \varepsilon\, S_y$$

where $g(S) = \Gamma_p - \frac{P}{\Gamma_x} + \frac{P\,R}{\Gamma_x{}^2}\, S = \Gamma - W + \eta\, S$ and $\alpha = \alpha_1 - \alpha_2$, following the conventions established in [103]. In addition to the trivial $S = 0$, Equation (4-2) has two sets of solutions: two paramagnetic and two ferromagnetic solutions.

The paramagnetic solutions correspond to the *H*- and *V*-polarised states: $S_y = S_z = 0$, $S_x = \pm(W - (\Gamma \pm \gamma))/\eta$. The positive solution corresponds to the *H*-state and is always unstable due to its shorter lifetime. The condensation threshold is first reached for the longer lifetime mode (*V*) at $W_1 = \Gamma - \gamma$ and it remains the only stable solution at low powers. At a critical occupation (S_c) and critical pumping (W_2) this paramagnetic solution also becomes unstable:

$$S_c = \frac{\gamma^2 + \varepsilon^2}{\alpha\, \varepsilon} \qquad\qquad W_2 = W_1 + \eta\, S_c \tag{4-3}$$

At this critical threshold, the single paramagnetic solution bifurcates into two ferromagnetic solutions. While the paramagnetic solution is parity symmetric, i.e. unaffected by the exchange of right- and left-circular polarisation ($S_z \to -S_z$), the new solutions are not. The bifurcation breaks the parity symmetry with the formation of elliptically polarised states. Obtaining closed-form expressions for these solutions is impossible, but the following analytical expressions provide most of the required physical insight:

$$\begin{aligned} S_x &= -\frac{g(S)}{\gamma} S & S_y &= -\frac{g(S)}{\varepsilon} S_z \\ S_z &= \pm\frac{\varepsilon}{\gamma}\sqrt{\frac{\gamma^2 - g(S)^2}{\varepsilon^2 + g(S)^2}}\, S & S &= \frac{\gamma\,(\varepsilon^2 + g(S)^2)}{\alpha\,\varepsilon\, g(S)} \end{aligned} \tag{4-4}$$

Note S_x is always negative, but the sign of both S_y and S_z changes for each of the two solutions. This means that a left-circularly polarised component is accompanied by a diagonal component ($S_z < 0 < S_y$), while a right-circularly polarised component is accompanied by an anti-diagonal component ($S_z > 0 > S_y$). Experiments show such a correlation between the linear and circular components (Figure 4.3c).

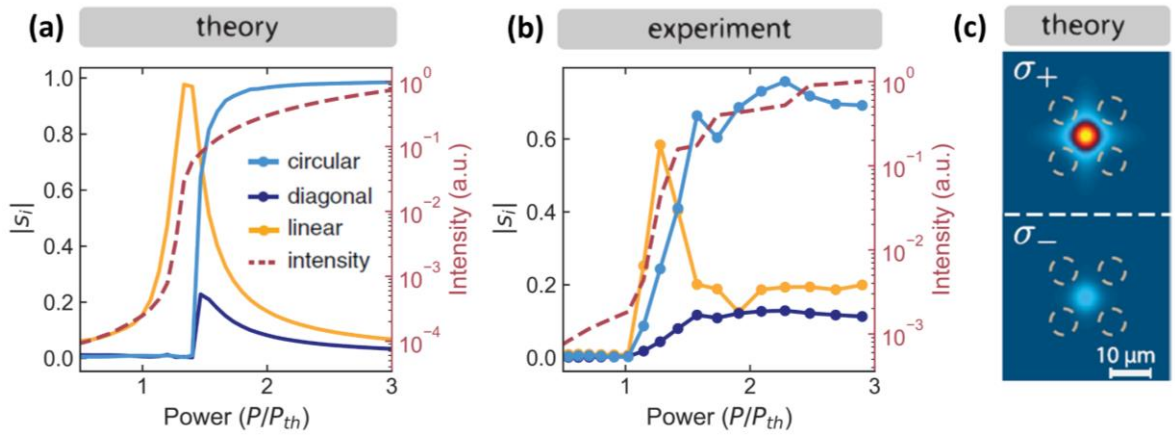

Figure 4.6 **Comparison of simulations and experiment. (a)** Power dependence of the three polarisation components of the polariton wavefunction simulated from Equation (4-1). **(b)** Measured power dependence of the three polarisation components. **(c)** Spatial images of 2D simulations showing trapped condensates with elliptical polarisation. The handedness was stochastic (not shown). Modified from [103] Parameter values are $\alpha_1 = 0.015\text{ps}^{-1}$, $\alpha_2 = -0.5\alpha_1$, $\Gamma_p = 0.1\text{ps}^{-1}$, $\Gamma_X = 0.1\Gamma_p$, $R = 0.1\text{ps}^{-1}$, $\varepsilon = 0.045\text{ps}^{-1}$, $\gamma = 0.1\varepsilon$

The role of γ in driving the spin bifurcation is crucial, and only if $\gamma > 0$ does this theory work. For $\gamma < 0$, the higher energy linearly polarised mode has shorter lifetime and the ferromagnetic solutions lose their stability. The only stable solution, at all powers, is the *H*-polarised state, linearly polarised along the minimum-energy direction. For $\gamma = 0$, the ferromagnetic solutions turn into limit cycle oscillations, which have been previously connected to self-induced Larmor precession [106] and which are also connected to the idea of self-trapping (Sec. 4.2.3).

An important assumption so far has been the spin-independence of the gain saturation $g(S)$. In general, this term should be modified to allow for the saturation to depend on the individual occupation of right- or left-circular polarization. The third line in Equation (4-1) would become $\dot{n} = P - \Gamma_x - (R_s\,|\psi_\uparrow|^2 + R_o|\psi_\downarrow|^2)n$, with $R_{s/o}$ being the same-spin and opposite-spin saturation constants. Such a term does not destroy the parity breaking spin bifurcation, but the stability of the solutions is significantly more complex and will be explored in Chapter 5.

Numerically solving Equation (4-1) as a function of power, there is good agreement with experiment (Figure 4.6). Below the critical occupation $S < S_c$, the condensate is linearly polarised along the higher-energy, low-dissipation direction. When the occupation is

increased $S > S_c$, the condensate becomes elliptically polarised, with an increase of both the diagonal and the circular components. Extending Equation (4-1) to account for the 2D real-space degrees of freedom of the polariton condensate (Figure 4.6c) gives quantitatively equivalent results to the 0D theory.

4.2.2 Polarisation splitting

Up to now, the spin bifurcation has been able to reproduce the experimental results. Both the formation of a linearly polarised condensate below a critical threshold (S_c) and the stochastic formation of elliptically polarised condensates above S_c are captured by the theory. However, no justification has been provided for the energy (ε) and dissipation (γ) splitting of the linearly polarised modes on which the model relies.

Inhomogeneous sample strain is known to split the polariton mode into two, in-plane linearly polarised modes at different energies, either by splitting of the exciton modes through exchange interactions [125] or by splitting of the cavity modes through birefringence. Even tiny levels of birefringence, on the order of 0.004%, produce measurable splitting. [26] The splitting can be directly measured by energy resolving the polariton photoluminescence below threshold. Figure 4.7a demonstrates 30μeV splitting between horizontal and vertical polarisation. No splitting was observed in the circular basis. The magnitude of the splitting varies across the sample, reaching 100μeV near the edges of the etched mesas in the

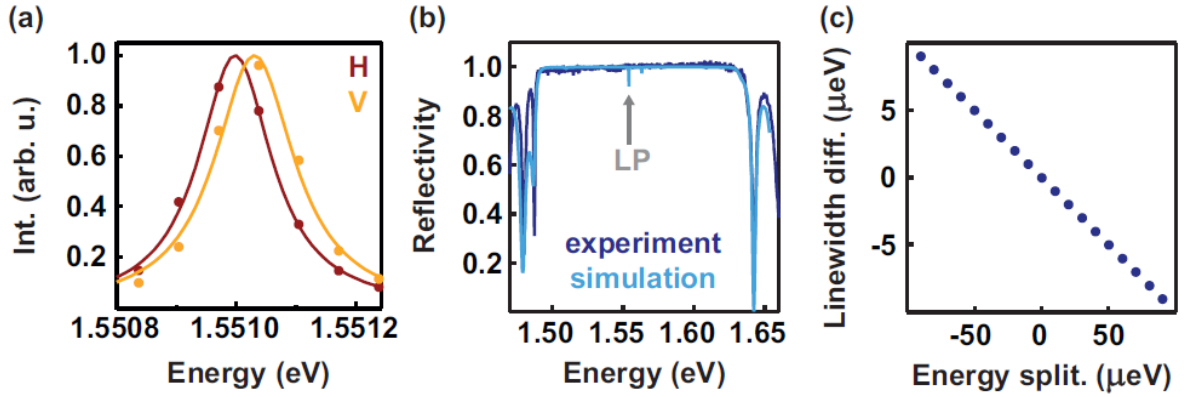

Figure 4.7 **Energy and dissipation splitting. (a)** Energy-resolved photoluminescence below threshold for horizontally and vertically polarised light, showing ~30μeV energy splitting. **(b)** Comparison of experimentally measured reflectivity and that from transfer matrix simulations. **(c)** The slight curvature of the DBR reflection band causes a linewidth difference between modes at different energies. Taken from [103]

electrically contacted sample. The orientation of the splitting, i.e. the linear polarisation direction of the highest-energy mode, also varies randomly along the sample and is not necessarily between horizontal and vertical polarisation.

In addition to an energy difference between linearly polarised modes, the spin bifurcation model requires a difference in the lifetimes (γ), with the higher energy mode having a longer lifetime. Even a small difference in the lifetimes, on the order of a few percent of the total linewidth, are enough to drive the spin bifurcation. Since the polariton linewidth is almost resolution-limited, direct measurement of such tiny differences is difficult, if not impossible. A possible physical explanation for γ comes from considering the slight curvature of the DBR stopband (Figure 4.7b), which has a maximum in the middle. If the two linearly polarised modes are at slightly different energies, they will experience slightly different DBR reflectivity, and will necessarily have different lifetimes. If the modes are in the low-energy half of the DBR stopband, the higher energy mode will have longer lifetimes, as required for the spin bifurcation. Transfer-matrix simulations for our sample parameters support this argument and provide a sufficiently large difference in the linewidths to support the spin bifurcation theory (Figure 4.7c).

The very small energy splittings involved are comparable to splittings due to nuclear spin polarisation: a fully polarised GaAs lattice would lead to splittings of multiple 10s of μeV. [126,127] Given that are condensates are strongly magnetised, it is reasonable to think they could drive the optical orientation of the nuclei, which could create a sufficiently large magnetic field to split the circular polarisation components. However, we see no splitting in the energy of the circular components. Additionally, one would expect this nuclear polarisation to decay very slowly (on the order of many seconds). Hence, if one were to pump the condensate with a long pulse (a second) and then create multiple short condensates (a few μs long) immediately after, one would expect some memory effects, which we have not seen.

4.2.3 Connection to self-trapping

The physics of the spin bifurcation has a very close analogy to the physics of self-trapping in bosonic Josephson junctions. [52,128–130] Considering a two-level nonlinear system, with coherent coupling between the two levels, the evolution of the system will be governed by:

$$i\,\hbar\frac{d\psi_1}{dt} = UN_1\psi_1 - J\,\psi_2$$
$$i\,\hbar\frac{d\psi_2}{dt} = UN_2\psi_2 - J\,\psi_1 \tag{4-5}$$

where $\psi_{1,2}$ are the wavefunctions of the two levels, $N_{1,2}$ the occupation numbers, U the nonlinear constant and J the Josephson coupling. The total energy can be written in terms of the population difference $z = \frac{N_1 - N_2}{N_1 + N_2}$ and phase difference $\theta = \arg(\psi_1) - \arg(\psi_2)$: [128]

$$H = \frac{UNz^2}{4J} - \sqrt{1 - z^2}\cos\theta \tag{4-6}$$

where $N = N_1 + N_2$. It is instructive to plot the energy contours of the system as a function of the phase and population difference to understand the full dynamics of Equation (4-5). In the linear limit, Equation (4-5) reduces to the coupling of a two-level system, resulting in bonding and antibonding modes (Figure 4.8a). Figure 4.8b shows the energy contours in the linear limit, with a low-energy (bonding, brown) and a high-energy mode (antibonding, green). If the system does not start in one of these eigenmodes, it will oscillate along the contour lines of constant energy. Adding nonlinearity to one of the modes, say a repulsive nonlinearity in ψ_2, modifies the energy contours (Figure 4.8c). The lowest energy mode (brown) is no longer a balanced mix of ψ_1 and ψ_2, but a state with higher occupation in ψ_1

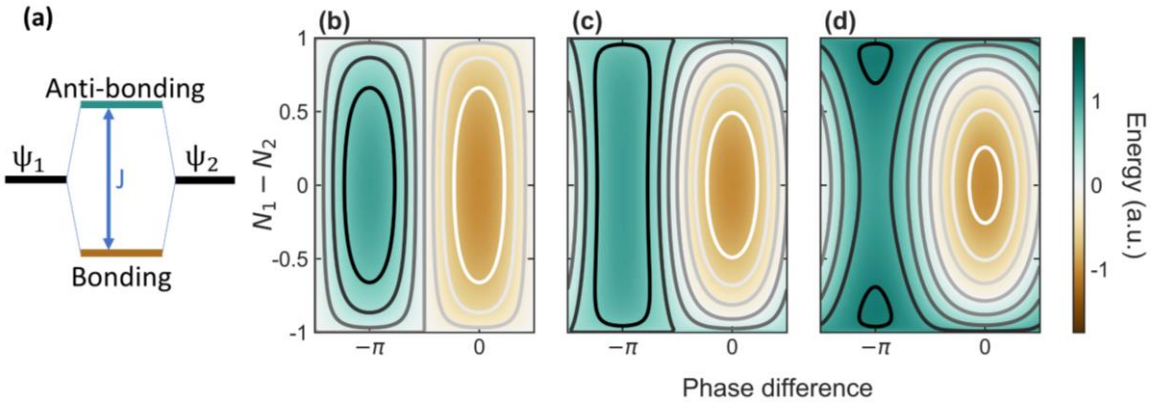

Figure 4.8 **Conservative physics and self-trapping. (a)** Coupling of ψ_1 and ψ_2 into bonding-antibonding modes. **(b)** Energy contours in the linear limit. **(c)** Energy contours for repulsive/attractive interactions in ψ_2/ψ_1. **(d)** Energy contours for repulsive interactions in both ψ_1 and ψ_2, showing the two self-trapped solutions at phase difference $-\pi$

which minimises the nonlinear interactions of ψ_2. Hence nonlinear interactions lead to imbalance in the populations. With this in mind, the behaviour of the system when both modes are nonlinear is easier to understand (Figure 4.8d). The antibonding mode splits into two modes with non-zero population imbalance, and there are three fixed points instead of two. Initialising the system with all the population in one mode, means population transfer to the other mode is impossible as it would violate energy conservation. In this sense, the population is *self-trapped* by nonlinear interactions.

These new self-trapped states are completely analogous to the spin bifurcated states discussed previously. The analogies between Equation (4-5) and Equation (4-1) become clear when we consider the fact that the feeding term in Equation (4-1) is spin independent and can be effectively ignored when discussing spin dynamics. Hence, the two modes $\psi_{1,2}$ correspond to right- and left-circular polarisation $\psi_{\uparrow,\downarrow}$. The spin nonlinearities ($\alpha_{1,2}$) can be mapped to $U_{1,2}$. The splitting between linear polarisations (ε) corresponds to Josephson coupling (J) between the circular polarisations. The only difference left is the γ term of Equation (4-1). This term makes the spin dynamics dissipative, and energy contours cannot be used to describe the dynamics. Plotting the evolution of the system in population difference vs phase difference

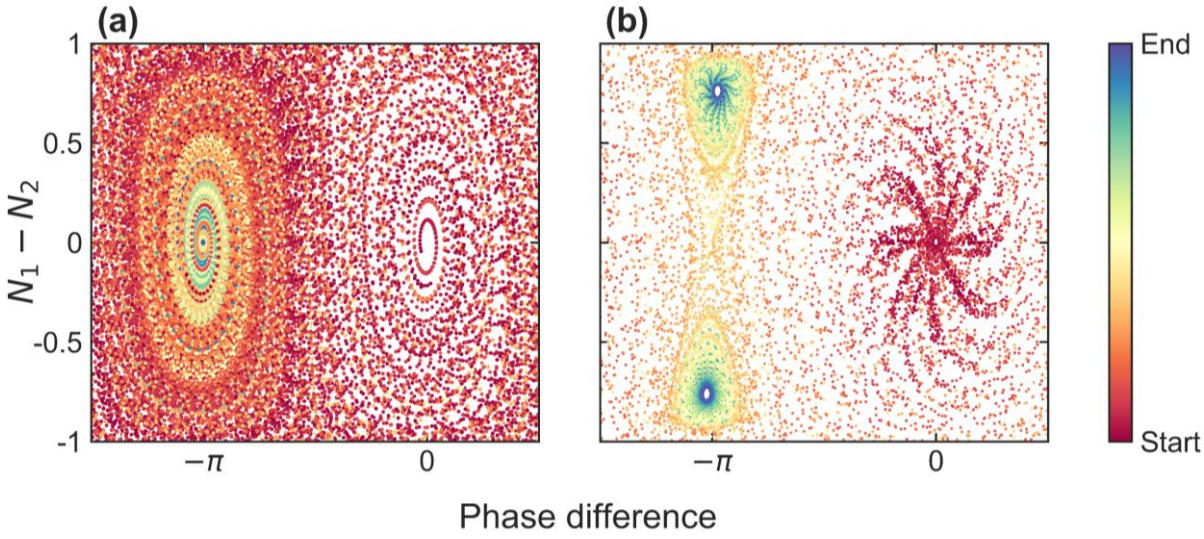

Figure 4.9 **Dissipative physics and spin bifurcation. (a)** Simulated spin trajectories in the linear limit. All solutions end in the *V*-polarised mode (phase difference $-\pi$). **(b)** Simulated spin trajectories in the nonlinear limit, showing the two spin-bifurcated/self-trapped solutions. The simulations end before reaching the steady state, leading to the empty space around the steady states.

shows the similarities of self-trapping and spin bifurcation (Figure 4.9). Population differences correspond to circular degree of polarisation. Phase difference corresponds to the angle of the linear polarisation, the *H*-polarisation having 0 phase difference and *V*-polarisation having $-\pi$. In the linear regime, the γ term makes the antibonding/*V*-polarised state have a longer lifetime, and all trajectories end up at this fixed point (Figure 4.9a), even though it is the state of highest energy. Similarly, in the nonlinear regime, all the trajectories end up at one of the self-trapped solutions, since they have the longest lifetime (Figure 4.9b).

4.3 Electrical control

This section studies the influence of external electric fields on the spin bifurcation. The sample used is the electrically contacted one, which has the same underlying semiconductor structure as in the rest of this chapter (Sec. 3.2). Voltages between -15V and +15V are applied to create electric fields perpendicular to the quantum wells and two measurements are performed: spectrally-resolved photoluminescence below threshold for horizontal and vertical polarisation, and full Stokes-vector characterisation of the condensate above threshold.

The external bias induces a small energy splitting between the $[110]$ and $[1\bar{1}0]$ crystal axes, which correspond to horizontal and vertical polarisation (Figure 4.10a). This splitting is linear with applied voltage, with slope 0.9μeV/V (Figure 4.10b). Two physical mechanisms can contribute to this splitting, one affecting the photonic part of polaritons and one affecting their excitonic part. First, the Pockels effect induces birefringence linearly proportional to the applied field. This changes the refractive index of the $[110]$ and $[1\bar{1}0]$ and hence changes the energy of the cavity resonance for polarisations aligned along those axes. [26] Second, an electric field applied along the growth axis $[001]$ induces light-heavy hole mixing at the quantum well interfaces and breaks the spin degeneracy of the excitonic ground state, which is split into two linearly polarised excitons along $[110]$ and $[1\bar{1}0]$. [131] Distinguishing between both effects is beyond the scope of this work, but note that either one of them could be large enough to explain the experimentally measured splitting.

Given that splitting between linearly-polarised modes is one of the driving factors behind the spin bifurcation, tuning the splitting via electric fields is expected to significantly affect the

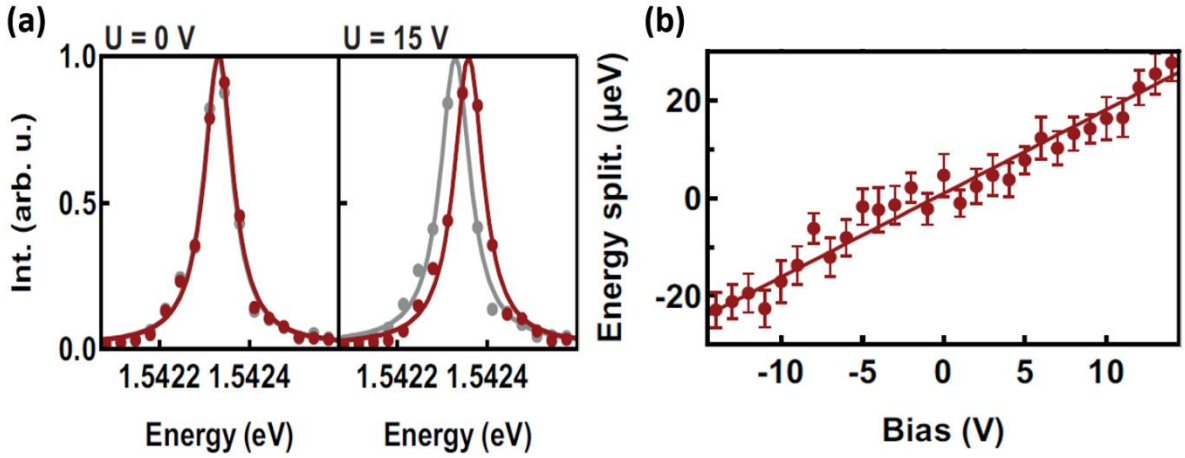

Figure 4.10 **Voltage-induced polarisation splitting. (a)** Energy resolved, below threshold photoluminescence of horizontal (grey) and vertical (red) polarisation at two different applied voltages. **(b)** Energy splitting between linear polarisations as a function of applied voltage. Taken from [104]

spin properties of the condensate. Figure 4.11a shows the variation of the three condensate polarisation components with voltage. The power is kept constant and 200 condensates are created at each voltage. At zero bias, the condensate behaves as described previously: it stochastically forms in one of two elliptically polarised states. The spin-up state is shown with a solid line, and the spin-down state with a dashed line. As the bias is increased, the two bistable solutions become more linearly polarised. At the highest voltages, bistability is lost and the condensate forms in the linearly polarised state of highest energy. For large negative bias, the linear polarisation is horizontal, while for large positive bias it is vertical.

This behaviour can be well reproduced within the spin bifurcation model by adding an additional energy and dissipation splitting due to the applied voltage:

$$\begin{aligned}\frac{d\Psi}{dt} = &\left[-g(S) - i\left(\left(\alpha_1 + \alpha_2\right)S + \left(\alpha_1 - \alpha_2\right)S_z\sigma_z\right)\right]\Psi \\ &-\frac{1}{2}\left(\gamma_s - i\,\varepsilon_s\right)\left(\cos(2\theta_s)\,\sigma_x + \sin(2\theta_s)\,\sigma_y\right)\Psi \\ &-\frac{1}{2}\left(\gamma_U - i\,\varepsilon_U\right)\left(\cos(2\theta_U)\,\sigma_x + \sin(2\theta_U)\,\sigma_y\right)\Psi\end{aligned} \tag{4-7}$$

where $\Psi = \{\psi_\uparrow, \psi_\downarrow\}$, σ_i are the Pauli matrices and $g(S)$, α_1, α_2, S_z and S are the same as before. The splitting terms have now been generalised to be along arbitrary directions of the sample, parametrised by θ_s for the strain splitting (γ_s, ε_s), and θ_U for the voltage-induced

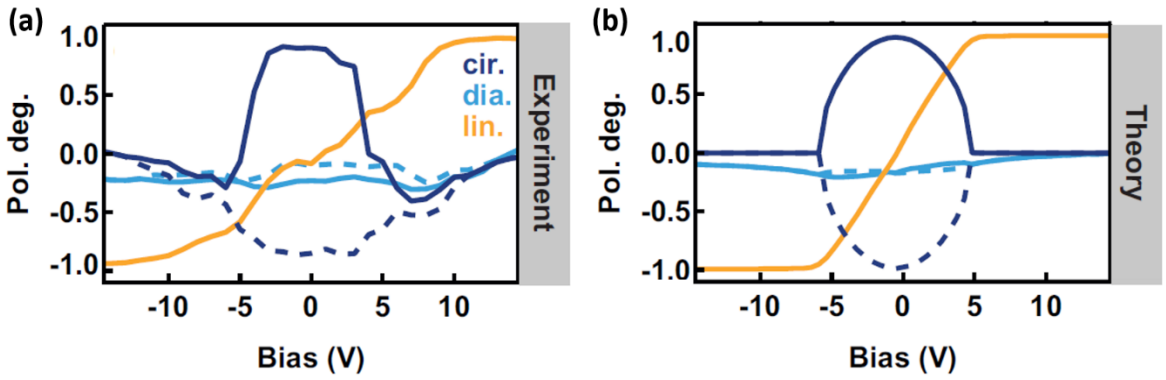

Figure 4.11 **Electrical control of spin bifurcation. (a)** Experimentally measured condensate polarisation components. **(b)** Simulated condensate spin using the splitting from Figure 4.10b. Taken from [104]. Parameter values are $\alpha_1 = 0.015\text{ps}^{-1}$, $\alpha_2 = -0.5\alpha_1$, $\Gamma_p = 0.2\text{ps}^{-1}$, $\Gamma_X = 0.1\Gamma_p$, $R = 0.1\text{ps}^{-1}$, $\varepsilon_s = 0.045\text{ps}^{-1}$, $\varepsilon_U = 0.0135\text{ps}^{-1}/V \times U$, $\gamma_{s,u} = 0.05\varepsilon_{s,u}$

splitting (γ_U, $\varepsilon_U \propto bias$). Experimentally, θ_s would vary along the sample according to local strain distributions, while $\theta_U = 0$ would be fixed to the $[110]$ and $[1\bar{1}0]$ crystal axes.

Using the experimentally measured voltage-induced splitting (Figure 4.10), numerical simulation of Equation (4-7) shows strong agreement with the experimental results (Figure 4.11). To achieve agreement between theory an experiment, $\theta_s = -25^\text{o}$ and $\theta_U = 1.3^\text{o}$ (the cryostat was slightly tilted) were used. At zero bias, there are two solutions with a strong degree of circular polarisation. As the bias is increased, the solutions become more linearly polarised until the bistability is lost and the only stable state is linearly polarised. These results can be understood within the spin bifurcation by recalling that the bifurcation occurs above a critical condensate occupation:

$$S_c = \frac{\gamma^2 + \varepsilon^2}{\alpha\,\varepsilon}$$

where ε and γ are taken along the axes of maximum splitting. Ignoring the small strain splitting, ε and γ increase linearly with external voltage, hence so does S_c. This means that for constant pumping power, if the system is above the bifurcation threshold at zero-bias, it will transition to below the bifurcation threshold above a certain bias. This is what is happening in Figure 4.11, where at zero bias the condensate shows spin bifurcated states which disappear as the bias is increased. The theory predicts that the condensation at high voltages occurs in the linearly polarised state of *higher energy* (and lower dissipation).

4.3.1 Spin flips and hysteresis

In this section, the electrical control of the polarisation is used to create a spin switch, with sub-femtojoule switching energies. The discussion so far has been limited to a situation where the nonresonant pumping is spin balanced, creating equal populations of spin-up and spin-down excitons. At 0V, this occurs for any linear polarisation of the pump. At nonzero bias, however, spin balanced pumping requires the laser to be aligned along either the [110] or [1$\bar{1}$0] crystal axes. The reason for this is that the Pockels effect creates birefringence in the sample, with these two axes being the major and minor axes of the refractive index ellipse. Any linear polarisation not aligned with these axes will acquire some degree of circularity while travelling through the DBRs, and will hence create spin-imbalanced exciton populations in the quantum wells.

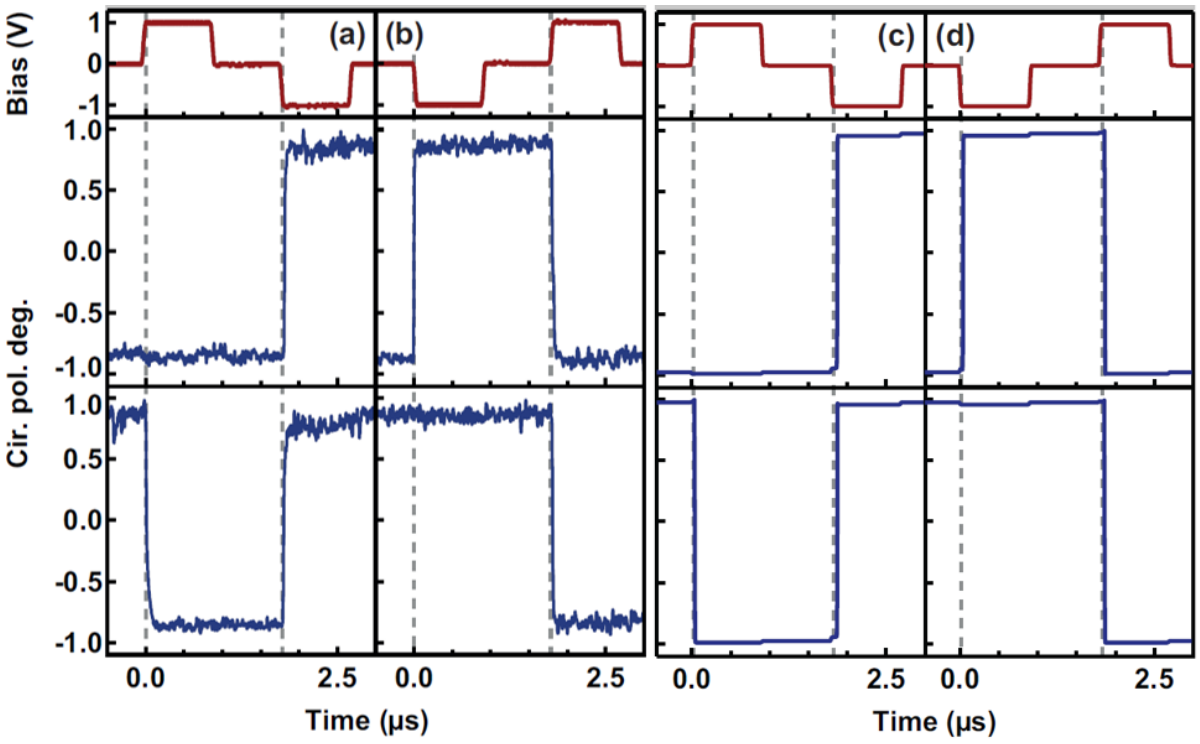

Figure 4.12 **Electrical spin switching.** Effect of two different pulse sequences (top row) on circular polarisation starting spin down (middle row) or spin up (bottom row). **(a-b)** Experimentally measured degree of circular polarisation. **(c-d)** Simulated circular polarisation using Eq. (4-7). Taken from [104]. The parameter values are the same as in Figure 4.11, adding a difference in the pumping terms between spin-up ($P + \Delta P$) and spin-down ($P - \Delta P$) components proportional to the applied field $\Delta P/P = -0.002 \times U$

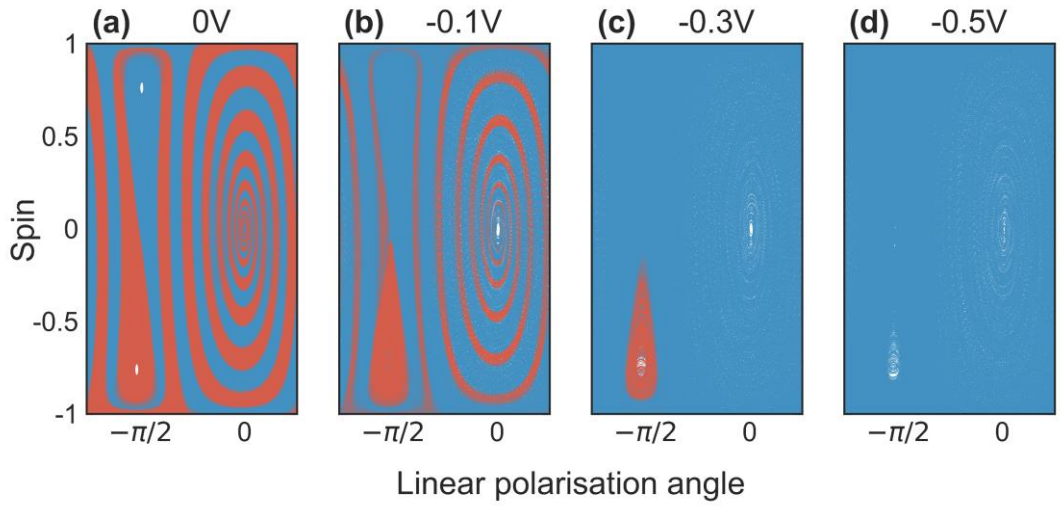

Figure 4.13 **Basins of attraction.** Condensate spin trajectories for 1000 initial points on the Poincare sphere surface, for four applied voltages **(a-d)**. Trajectories are blue or red depending on whether they end up in the spin-up or spin-down attractor

This spin imbalance breaks the parity symmetry and strongly affects the condensate steady states. Figure 4.12a,b shows the effect of two different voltage pulse sequences on the condensate: a +1V pulse followed by a -1V pulse, or vice versa. The positive voltage pulse creates a spin-down imbalance, while the negative pulse creates a spin-up imbalance. Before the pulses are applied, the condensate is stochastically in either a spin-down (top row) or a spin-up state (bottom row). The spin-down imbalance created by the +1V pulse has no effect on the condensate if it is in the spin-down state, but triggers a spin switch if it is in the spin-up state. The reverse occurs for the -1V pulse: it doesn't affect the spin-up state, but spin switches the spin-down state. Note that the condensate stays in the spin-switched state after the voltage has been turned off. The spin bifurcation theory can reproduce the switching caused by the pulse sequences (Figure 4.12c,d), by using a spin imbalance linearly proportional to the applied voltage. From numerical simulations, this is estimated to be $0.002V^{-1}$, which can easily be caused by the birefringence of the Pockels effect.

The spin switching occurs over timescales faster than the rise time of the electrical pulse (~50ns in this experiment) and faster than the time resolution of our PMTs (~2ns) indicating that the spin switching is a non-adiabatic process. To understand this non-adiabaticity, it is useful to look at the basins of attraction of the two spin bifurcated solutions and see how they change with applied voltage. The basin of attraction of a fixed point is the region in phase space for which all trajectories end up at the fixed point. For the purposes here, the full phase

space can be flattened to the surface of the Poincare sphere (Figure 4.13, see also Sec. 4.2.3). At zero applied voltage, the two basins of attraction occupy equal areas. As a voltage is applied, one of the basins grows while the other one shrinks, until it fully disappears. If the condensate starts in the down state (red) at zero bias, it will remain in that state until the basin of attraction disappears. When the basin completely disappears, the condensate will evolve towards the only remaining attractor, at a speed given by the polariton spin dynamics. In this sense, the transition is non-adiabatic and has nothing to do with the external bias.

The changes to the basins of attraction can also be used to understand the hysteretic behaviour of the spin switching (Figure 4.14). A voltage of approximately ± 0.3V is enough to make a basin of attraction disappear and force the condensate into a specific spin (Figure 4.14a). For $-0.3 < V < 0.3$, both basins co-exist and the polarisation depends on the history of the condensate. Hysteresis is observed when ramping the voltage backwards and forwards, which is well reproduced by simulations (Figure 4.14b). At stronger voltages the condensate forms in a linearly polarised state like before (Figure 4.11). Further work is needed to fully characterise the spin switching, including the influence of pump power, trap size, sample position and voltage ramp speed on the required switching voltages and hysteresis widths. Nevertheless, the work presented in [104] demonstrates that this proof-of-principle spin-switch can easily compete with state-of-the-art electronic switches.

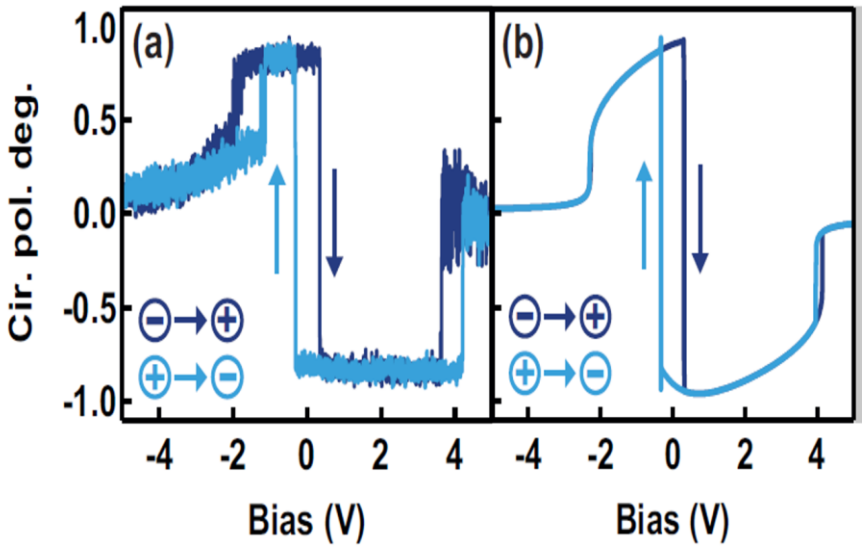

Figure 4.14 **Spin hysteresis with voltage. (a)** Measured circular polarisation for a ramp-up pulse (dark blue) followed by a ramp-down pulse (light blue). **(b)** Simulations for same conditions. Taken from [104]

4.4 Conclusion

This chapter has shown how optically trapped condensates can display new spin properties. Spontaneous condensate magnetisation into either one of two well defined circularly polarised states was shown to happen at a critical threshold S_c above condensation. This behaviour is crucially dependent on the spatial separation of the condensate and the exciton reservoirs and disappears if a very weak exciton reservoir is created on top of the condensate.

The phenomenology has been explained as a parity-breaking spin bifurcation. The theory relies on two different ingredients. First, a splitting of linearly polarised modes in energy and in dissipation, with the higher energy mode having the longest lifetime. And second, a spin-asymmetry of the polariton-polariton nonlinearities ($\alpha_1 \neq \alpha_2$). A connection was made between the spin bifurcation and general concepts of self-trapping.

Finally, electric fields have been used to control the splitting of the linearly polarised modes and hence control the condensate spin. Slight spin imbalances caused by the voltage-induced birefringence were shown to cause spin flips. Hysteresis of the spin with applied voltage demonstrated a reliable spin switch.

Chapter 5 Spin flips and dynamical instability

This chapter explores the stability of spin bifurcated optically trapped condensates to changes in trap size and pump laser power.[4] It is found that number fluctuations from the scattering of reservoir excitons can destabilise the condensate and cause a spin flip. Single-shot streak camera imaging is used to measure individual spin flips with an average flip speed of 250ps. The spin flip rate is found to be exponentially sensitive to the condensate occupation, decreasing immediately after the spin bifurcation, but increasing again at higher powers. Tuning over at six orders of magnitude of spin flip rates is experimentally demonstrated, and the possibility of tuning over 10^{10} is discussed.

The spin bifurcation theory is extended to include fluctuations and cross-spin feeding from the reservoir. The experimentally measured flip rate and polarisation steady states are well reproduced by fitting the ratio of cross- to co-spin feeding from the exciton reservoirs to be ~0.6. This contrasts with previous literature, which has generally assumed this ratio to be 0 or 1. The cross-spin feeding destabilises the spin bifurcation, and frequency combs and chaotic behaviour are predicted to occur.

5.1 Stochastic spin flips

In the previous chapter, optically trapped condensates were shown to form in elliptically polarised states. These spin bifurcated condensates were shown to be stable over many seconds and to stochastically choose their handedness. At some sample positions however, the condensate appears to be unpolarised in time-averaged measurements. Time-resolved measurements reveal this to be due to fast stochastic spin flips. One possible cause for spin flips is thermal noise, and spin flips can occur for temperatures higher than 15K. [103] But

[4] This work has been published in [132]. Experimental work was done with Dr. H. Ohadi

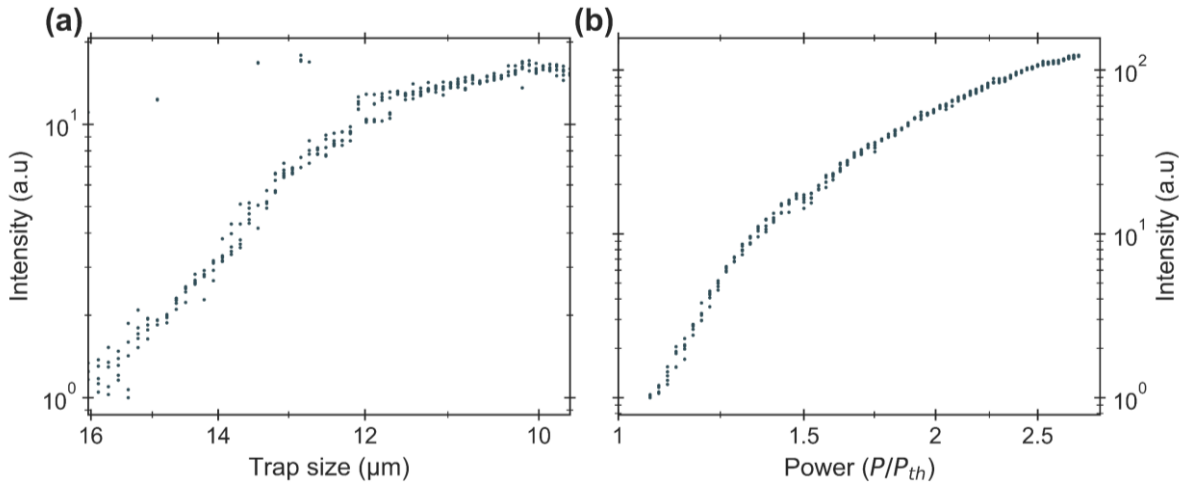

Figure 5.1 **Condensate occupation**. Normalised PL intensity as a function of **(a)** trap size (at constant power $1.4P_{th}$, 22mW) and **(b)** pump power (at constant trapsize 12μm)

even at the lowest temperatures, the spin bifurcated states are not always stable for long times. This section explores how the spin-flip rate and the spin bifurcated solutions depend on the optical trap size and the nonresonant power, demonstrating the need for a more complex description of the polarisation states.

Condensates are created in a square-shaped optical trap and the nonresonant pump is modulated into 5ms pulses. In one experiment the side of the square trap is varied between ~9.5μm and ~16μm keeping the power constant (22mW, which corresponds to $1.4P_{th}$ for a 12μm trap). In another, the trap is kept at 12μm and the amplitude of the laser pulses is varied between $1.1P_{th}$ and $2.7P_{th}$. In both experiments, five condensates are created at each experimental condition. The PL is polarisation-resolved in the circular basis and recorded on PMTs, so that the spin bifurcated states and the spin flip rate between them can be measured. The SLM phase pattern to create the square trap is calculated using the Direct Superposition algorithm instead of the usual MRAF algorithm, as it allows for much finer control of the trap size.

Increasing the laser power or decreasing the trap size increases the condensate occupation, as monitored in the PL intensity. For the largest traps, the condensate is just above threshold, and as the trap is made smaller the condensate intensity increases exponentially at first, slowing down the increase for traps smaller than ~12μm (Figure 5.1a). The reason for the increase in intensity with smaller traps is an increase in the spatial overlap between the condensate and the exciton reservoirs, leading to higher gain. The dependence of the intensity

on the pump power is similar: a fast increase at the lower powers that slowly saturates as the power is increased (Figure 5.1b).

It is not just the condensate occupation that shows similarities between the trap size and power dependencies, so do the condensate spin and spin flips rates. For some parameters the condensate is stable for the duration of the nonresonant pulse and remains in a single polarisation state (Figure 5.2a), but in most circumstances spin flips can be observed (Figure 5.2b,e,f). Changes to the polarisation states can be seen in a map of the probability of having a certain degree of circular polarisation at any given time (Figure 5.2c,g). For small occupation (trap>13.7μm or $P < 1.2P_{th}$), there is a single state with no circular polarisation. At a critical occupation (spin bifurcation) two elliptically polarised states appear, with a small degree of circular polarisation. These states are not very stable and have flip rates of the order of 100MHz (Figure 5.2d,h). As the occupation increases, the spin bifurcated states become more circularly polarised and the flip rate decreases exponentially over 5-6 orders of magnitude. At even higher occupations these trends are reversed: the degree of circular polarisation starts to decrease and the flip rate to increases again, albeit slower, over the same range.

The changes in flip rate can be intuitively understood from the evolution of the spin states. When the two bifurcated steady states are close to each other on the Poincare sphere (small $|S_z|$), any source of noise can easily cause spin flips. As $|S_z|$ increases and the two states move further apart in the Poincare sphere, it is harder for any noise to destabilise the condensate. Hence one would expect the flip rate to be minimum when the degree of circular polarisation is largest, and the flip rate to increase as $|S_z|$ decreases, which are exactly the trends of Figure 5.2. While any source of noise could be causing the spin flips (thermal, exciton scattering, free-carrier scattering, laser intensity noise, etc.), it will be shown in the next section that it is enough to consider fluctuations of the exciton-reservoir feeding the condensate to qualitatively reproduce the data.

For traps between 11.7μm and 13.1μm, most of the condensate realisations showed no spin flipping and hence the extracted flip rate is just an upper limit. It was for these trap sizes that stability over seconds was demonstrated in Chapter 4, suggesting a $> 10^8$ variation in the flip

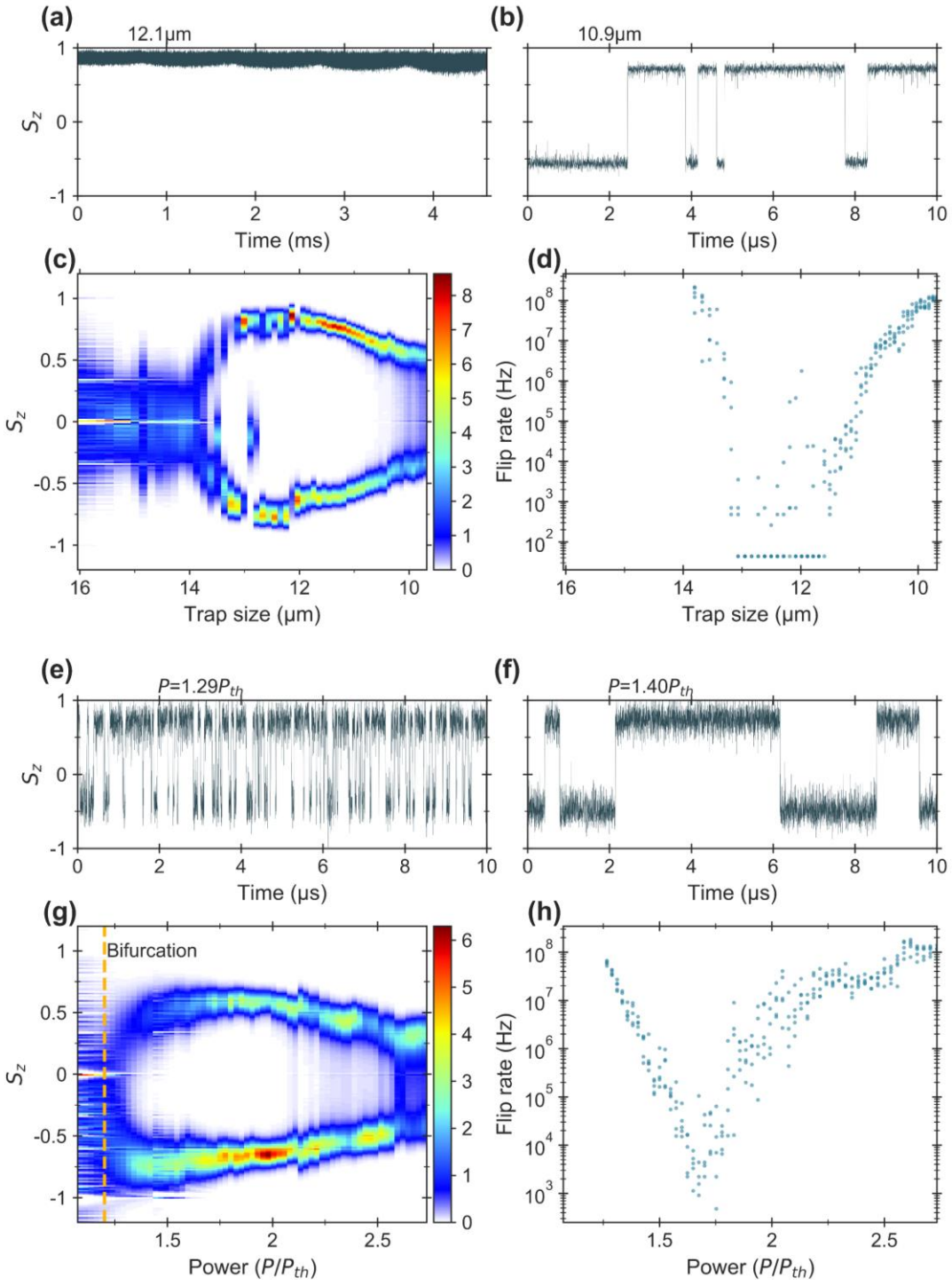

Figure 5.2 **Trap size dependence** (P =20mW). Example spin traces with **(a)** no spin flips and **(b)** a few spin flips. **(c)** 2D map of probability of having a specific S_z versus trap size, extracted from 10 experimental realisations. **(d)** Extracted flip rate vs power. No spin flips were observed for some realisations between 11.7μm and 13.1μm **Power dependence** (12μm trap). Example spin traces with **(e)** many spin flips and **(f)** a few spin flips. **(g)** 2D map of probability of having a specific S_z versus power, extracted from 10 experimental realisations. Larger spin noise at low powers ($< 1.3P_{th}$) arises from weak emission just above condensation threshold (P_{th}). **(h)** Extracted flip rate vs power.

rate, rather than just 5-6 orders of magnitude. The power dependence experiment, however, showed at least one spin flip in each trace in contrast with the trap size dependence and with Chapter 4. There are two explanations for this apparent contradiction. First, the larger spin flipping in the power dependence could be due to the pump laser becoming multimode for short periods of time, which strongly affects the polarisation states (Sec. 4.1). This argument could also explain why, for traps between 11.7μm and 13.1μm, some realisations show no spin flipping while others show MHz flip rates. The second explanation is that changing the trap size and changing the pump power are not completely equivalent processes, and that the changing overlaps between the condensate and the pump laser affect more than just the effective gain. Further work studying the full trap size and power dependence could clarify this issue.

Nevertheless, the qualitative change of the polarisation states and the flip rate with condensate occupation are clear and can be divided in two regimes. First, at a critical occupation two elliptically polarised states appear with a very fast flip rate, and as the occupation increases the states become more circularly polarised and the flip rate decreases by many orders of magnitude. Second, the trends reverse and the degree of circular polarisation decreases while the flip rate increases again over many orders of magnitude.

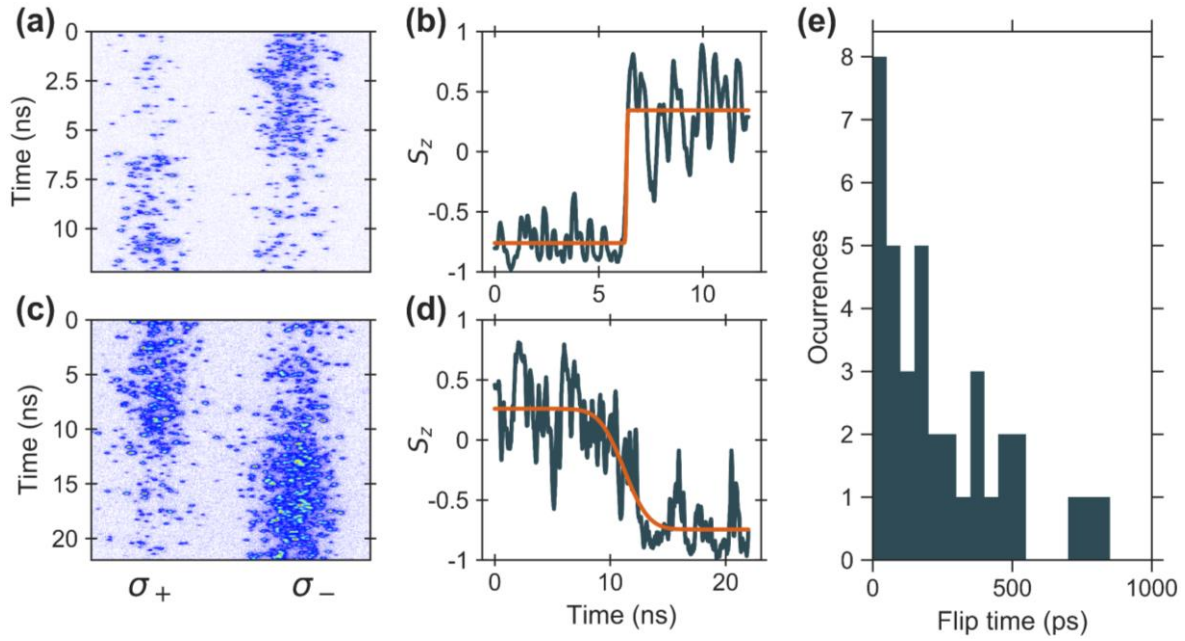

Figure 5.3 **Spin flip time. (a,c)** Raw streak image and **(b,d)** extracted spin trace of a short flip (52±1ps) and a long flip (4.2±0.1ns) respectively **(e)** Histogram of fitted flipping duration times at highest streak resolution.

Finally, the timescales on which individual spin flips occur are shown in Figure 5.3. Measurements were done on the streak camera in single-shot mode, allowing stochastic spin flips to be measured without the need for an external synchronised trigger. While the maximum time resolution of the streak in synchroscan mode is 2ps, the comparatively smaller signal-to-noise in these single-shot images (Figure 5.3a) results in a time resolution of 20ps. Experiments were done at a power and trap size with low flip rates to easily identify and isolate individual spin flips. The raw image of a spin flip with a measured flip time of 52 ± 1ps is shown in Figure 5.3a. The flip time is estimated by fitting an error function to the horizontally-binned spin trace (Figure 5.3b), and extracting the time taken to go from 10% to 90% of the full spin flip (the standard deviation is extracted from the fitting). This procedure does not take into account experimental errors due to shot-noise, and the extracted flip times and errors are strongly affected by shot-noise. Nevertheless, we can arrive at a good estimate for the true flip time by repeating this procedure for many well-isolated spin flips. The average spin flip time is 250ps and the distribution of spin flip times is shown in Figure 5.3e.

There are two other interesting features of the data for which more spin flips need to extract significant conclusions. The first is that approximately 20% of spin flips seem to occur faster than 50ps, a timescale comparable to the polariton lifetime (7ps) and shorter than the coherence time of the condensate (~100ps). Such fast flips are also reproduced in our simulations and could occur since spin dynamics are dominated by polariton nonlinearities, which can be faster than the polariton lifetime. [133] The second is that a non-negligible number of spin flips occur over significantly longer timescales, with some spin flips taking multiple ns (at a lower streak camera resolution in Figure 5.3c-d). Such long times are possibly due to multiple spin flips or oscillations that cannot be time resolved.

5.2 Mean-field theory and dynamical instability

The evolution of the polarisation states with condensate occupation shown in the previous section has very close similarities to that predicted by the spin bifurcation of the previous chapter (see Figure 4.6). For small occupations, the condensate is unpolarised in the circular basis and two elliptically polarised states emerge at a critical occupation. This transition is the

spin bifurcation transition from a linearly polarised state into two symmetry-breaking states at a critical occupation S_c. The increase of the degree of circular polarisation with increasing occupation is well reproduced by the previous bifurcation theory, where the spin bifurcated solutions move towards the poles of the Poincare sphere in the limit of strong pumping.

However, the decrease of circular polarisation for high occupation seen in Figure 5.2 cannot be accounted for in a simple spin bifurcation. Two effects could explain the phenomenon. First, Coulomb screening could lead to a decrease in the effective nonlinearities α_1/α_2 and of the circular polarisation at high powers. However, polariton densities are kept sufficiently low (~10^{10}cm^{-2}) for Coulomb screening to be negligible. [22] The second effect is a spin-asymmetric saturation of the condensate wavefuction. This can be included in the spin bifurcation via a spinor reservoir $n_{\uparrow/\downarrow}$ and spin-dependent feeding rates from the reservoirs to the condensate ($R_{s/o}$):

$$\frac{dn_\uparrow}{dt} = P - \Gamma_x n_\uparrow - (R_s|\psi_\uparrow|^2 + R_o|\psi_\downarrow|^2)n_\uparrow \,,$$

$$\frac{dn_\downarrow}{dt} = P - \Gamma_x n_\downarrow - (R_s|\psi_\downarrow|^2 + R_o|\psi_\uparrow|^2)n_\downarrow \,,$$

$$\begin{aligned}\frac{d\psi_\uparrow}{dt} = &\left[\frac{1}{2}(R_s n_\uparrow + R_o\, n_\downarrow - \Gamma_p) - \frac{i}{2}(\alpha_1|\psi_\uparrow|^2 + \alpha_2|\psi_\downarrow|^2)\right]\psi_\uparrow - \frac{1}{2}(\gamma - i\,\varepsilon)\psi_\downarrow \\ &+ dW_\uparrow \,,\end{aligned} \tag{5-1}$$

$$\begin{aligned}\frac{d\psi_\downarrow}{dt} = &\left[\frac{1}{2}(R_s\, n_\downarrow + R_o\, n_\uparrow - \Gamma_p) - \frac{i}{2}(\alpha_1|\psi_\downarrow|^2 + \alpha_2|\psi_\uparrow|^2)\right]\psi_\downarrow - \frac{1}{2}(\gamma - i\,\varepsilon)\psi_\uparrow \\ &+ dW_\downarrow\end{aligned}$$

where R_s is the same-spin feed rate and R_o is the opposite-spin feed rate. The other addition to the spin bifurcation model of Equation (4-1) has been a stochastic fluctuation term with $dW_{\uparrow\downarrow}$ being two independent complex Gaussian random variables with variance $\langle dW_{\uparrow,\downarrow}{}^\dagger dW_{\uparrow,\downarrow}\rangle = dt\left(R_s n_{\uparrow,\downarrow} + R_o\, n_{\downarrow,\uparrow}\right)$, where dt is the time step. This term arises from the simulation of polariton condensates using stochastic quantum methods. [78,106,134,135] Equation (5-1) is also an extension of mean field models used in the literature, where R_o has been generally assumed to be negligible [82,117,136] or simply equal to R_s. [106]

It is important to keep in mind that this model is phenomenological and R_s/R_o do not directly correspond to exciton scattering constants. They account for feeding and saturation of the condensate wavefunction coming from exciton-exciton scattering, biexciton formation, [119–121] or other microscopic processes. Numerical simulation of Equation (5-1) as a function of pump power shows good agreement with the experimental dependence on condensate occupation (Figure 5.4). The wavefunction is evolved for 100μs, with ten different initial conditions. Polarisation traces are extracted (Figure 5.4a-b) and the flip rate measured. The only fitting parameter is the ratio R_o/R_s, with the rest of the values used being the same or similar to those used in the previous chapter.

With $R_o/R_s \sim 0.6$, good qualitative agreement with the experimental data is observed. A linearly polarised solution splits into two elliptical ones at $P = 1.2P_{th}$ (Figure 5.4c), with a 10GHz flip rate (Figure 5.4d), much higher than the experimental resolution. As the power is

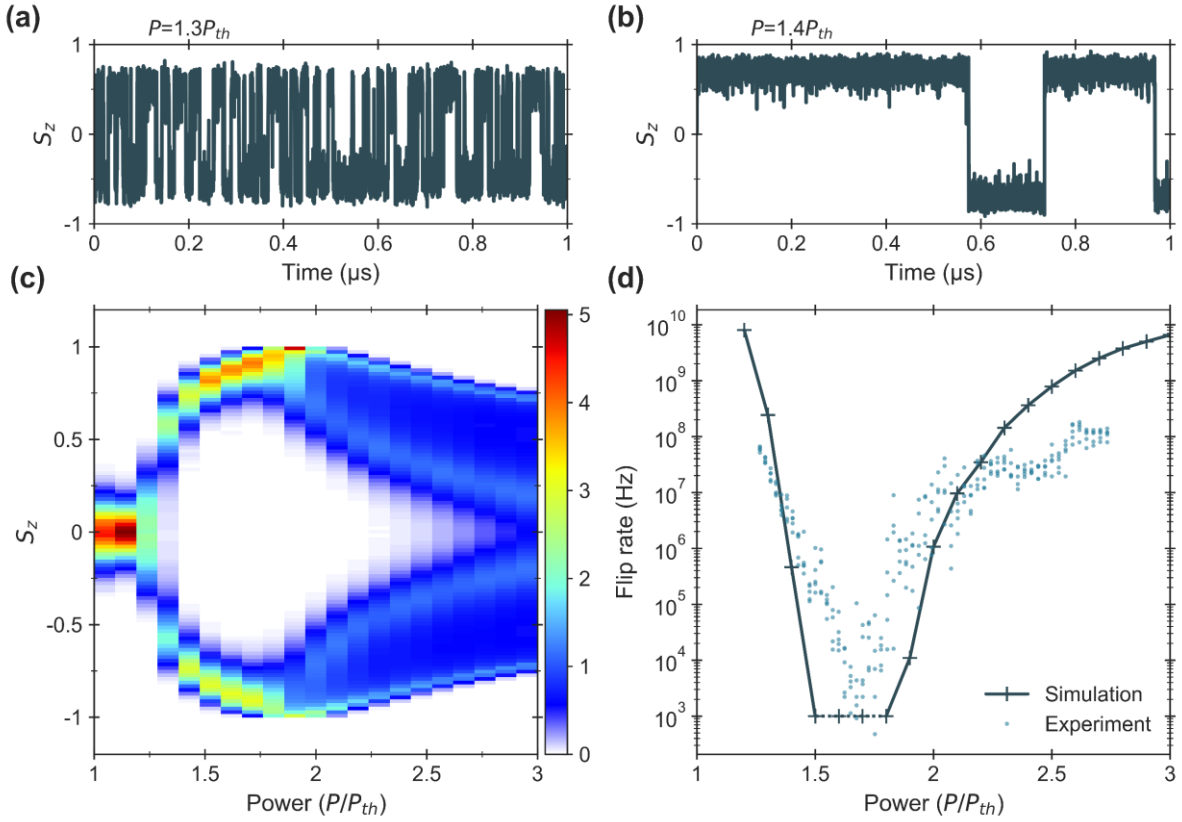

Figure 5.4 **Simulated power dependence.** Example spin traces from model showing **(a)** fast and **(b)** slow flip rates. **(c)** 2D probability density of S_z vs power. **(d)** Extracted flip rate vs power. No spin flips were observed between $1.5P_{th}$ and $1.8P_{th}$ for the simulated time ranges (dashed). Parameter values are $\alpha_1 = 0.01\text{ps}^{-1}$, $\alpha_2 = -0.5\alpha_1$, $\Gamma_p = 1\text{ps}^{-1}$, $\Gamma_x = 0.1\Gamma_p$, $R_s = 0.1225\text{ps}^{-1}$, $R_o = 0.6R_s$, $\varepsilon = 0.1\text{ps}^{-1}$, $\gamma = 0.1\varepsilon$

increased, the degree of circular polarisation increases and the flip rate decreases by almost 10^7. Between $P = 1.5P_{th}$ and $P = 1.8P_{th}$, the simulations showed no spin flips so the extracted flip rate is just an upper limit. From $P = 1.8P_{th}$, the two solutions broaden and their average degree of polarisation decreases while the flip rate increases again.

5.2.1 Frequency combs and chaos

It is instructive to explore the steady states of Equation (5-1) in the absence of noise and for a larger range of pumping powers than could easily be accessible experimentally (Figure 5.5). Plotting the flattened surface of the Poincare sphere (Figure 5.5b) makes it possible to easily visualise the spin steady states. As before, with increasing power a single linearly-polarised state ($P = 1.125P_{th}$) splits into two circularly polarised states ($P = 1.25P_{th}$), which rapidly develop strong circular polarisation, moving towards the poles of the Poincare sphere. A further increase of the pump power leads to the two circularly polarised steady states transforming into limit cycles ($P = 1.875P_{th}$) through a Hopf bifurcation. These oscillations increase in amplitude as the power is increased ($P = 2.25P_{th}$), until they merge into a single limit-cycle ($P{\sim}2.8P_{th}$, red line). This final limit cycle corresponds to oscillations around the linearly-polarised state of lowest energy ($P = 4.75P_{th}$).

Another way of looking at the changing steady states is by looking at their Fourier spectra (Figure 5.5c,d). Trivially, both the linearly polarised state at low power and the spin bifurcated states have no frequency components. The first limit cycles that appear at $P = 1.875P_{th}$ have a frequency comb spectrum with longest period ~30ps, and the higher harmonics become stronger at higher power ($P = 2.25P_{th}$). This is much faster than the experimental resolution and explains why no broadening into limit cycles is seen in the experiment. At the merging of the two limit cycles ($P{\sim}2.8P_{th}$, red line), the Fourier spectra does not show any structure, but has components at all frequencies. This is indicative of chaotic behaviour and is explored below. At the highest powers, the limit-cycle also has a frequency comb spectrum that is period-doubled ($P = 4.75P_{th}$).

At the merging of the limit cycles, a dynamical instability occurs and the polarisation dynamics of the condensate become chaotic (Figure 5.6). The time traces of the circular

polarisation are a random succession of positive and negative peaks every ~50ps. Trajectories that start very close to each other diverge exponentially away from each other in phase space, indicating a positive Lyapunov exponent and proving that the system is truly chaotic. [137] The chaotic strange attractor (Figure 5.6c) shows small oscillations in intensity, coupled with large oscillations across the Poincare sphere (S_z-θ plane).

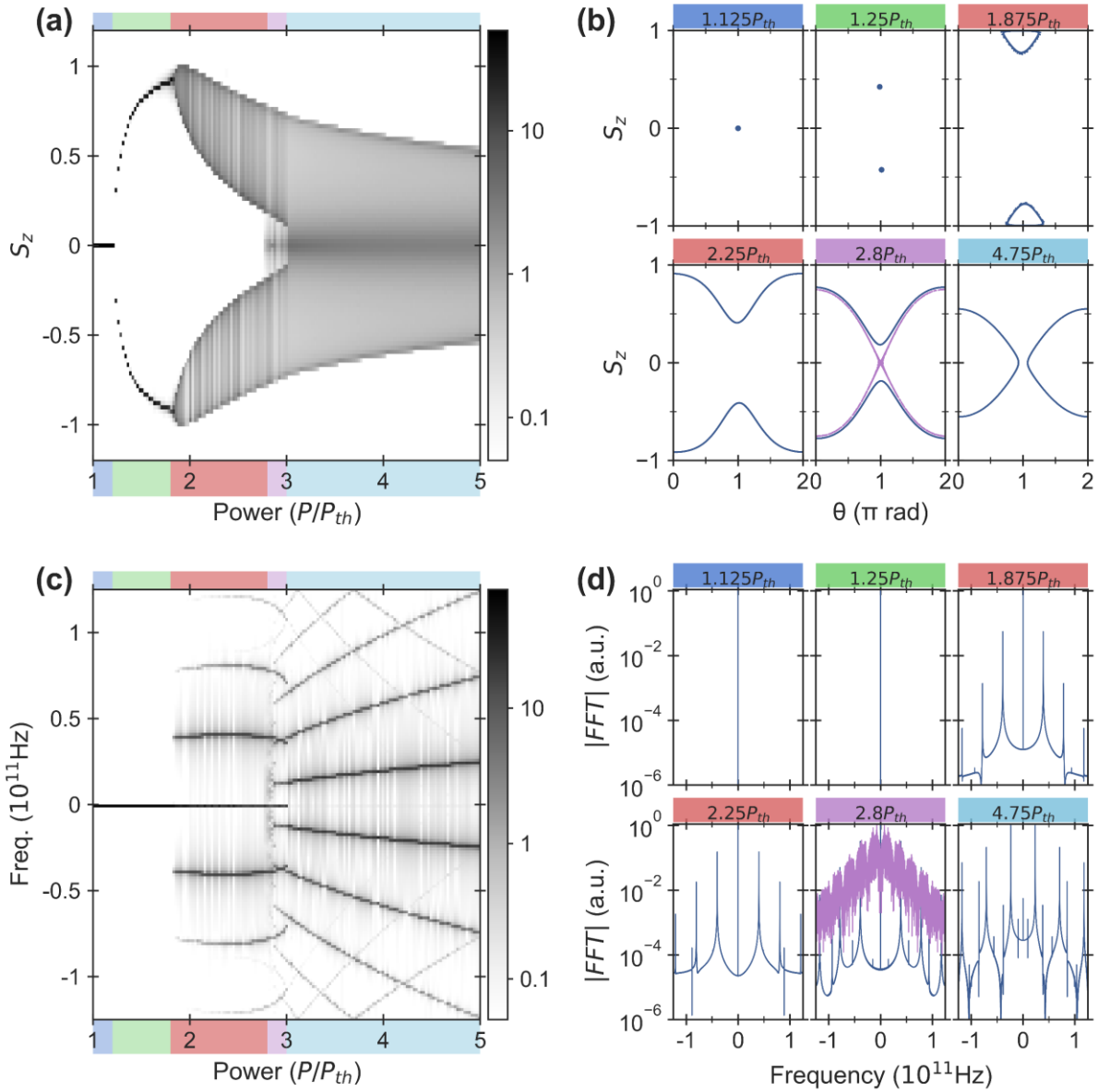

Figure 5.5 **Simulations with no noise. (a)** 2D probability density of S_z versus power. Colour-coded regions mark linearly-polarised (blue), spin-bifurcation (green), limit cycle (red), chaotic (purple), and period-doubling (cyan) phases. **(b)** Flattened surface of the Poincare sphere: vertical is z-coordinate in Poincare space (degree of circular polarisation), while horizontal corresponds to azimuthal angle (direction of linear polarisation component). **(c)** Fourier transform spectra versus power.**(d)** Normalised Fourier spectra.

By thinking in terms of the self-trapped solutions described in Sec. 4.2.3, Figure 5.5 can be qualitatively understood as a hierarchical succession of three different terms dominating the dynamics in Equation (5-1): the spin asymmetry of the nonlinearity (α=α1−α2), the energy splitting (ε), and the dissipation splitting (γ). Immediately after the bifurcation, all three terms lead to stable, elliptically-polarised fixed-point steady states. As the power is increased, γ becomes negligible and the system undergoes a Hopf bifurcation into effectively conservative spin dynamics around the self-trapped solutions. As the power is further increased, the spin asymmetry in the nonlinearity becomes negligible compared to the spin asymmetry in the feeding (R_s/R_o). With only ε left, the dynamics are effectively linear and conservative with oscillations around the lowest energy linearly polarised mode.

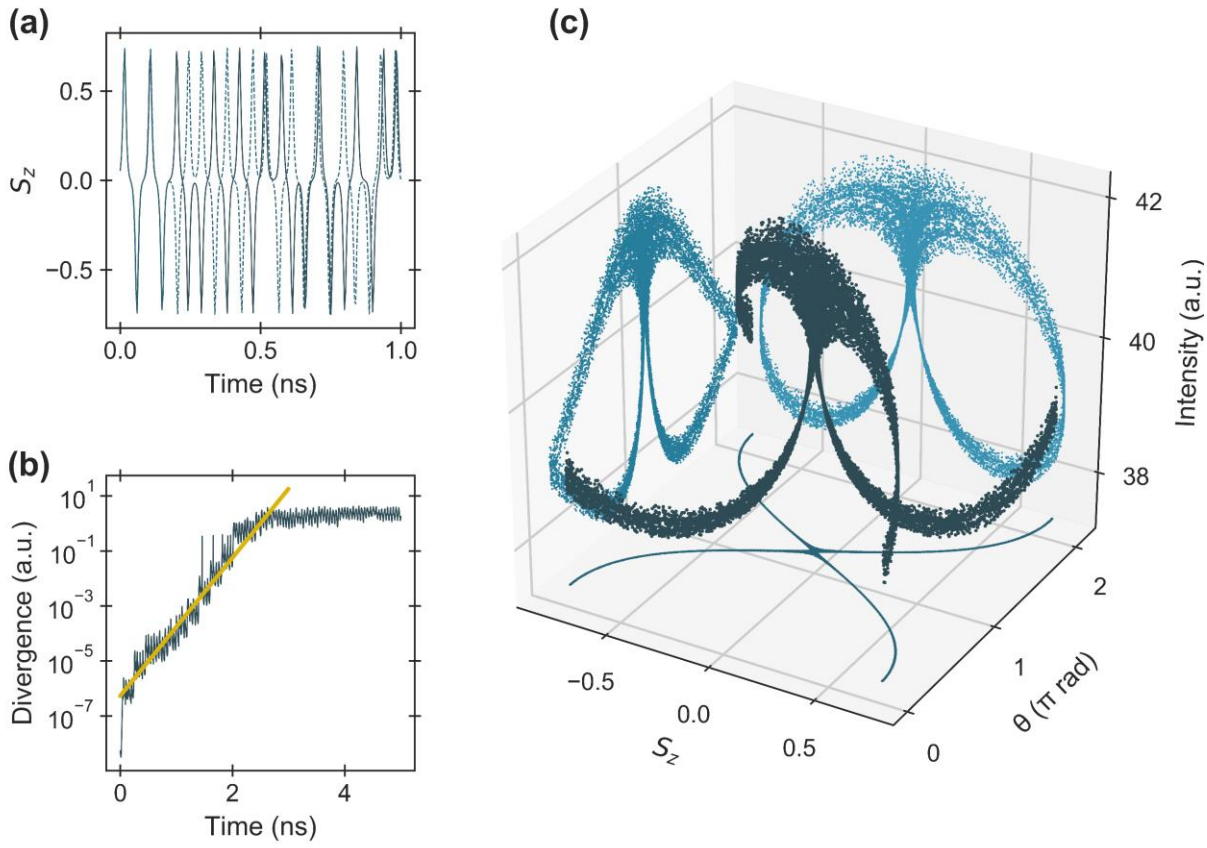

Figure 5.6 **Chaos. (a)** Two time-traces of the degree of circular polarisation that start very close to each other in phase-space. **(b)** Exponential divergence of nearby trajectories, normalised to the size of the strange attractor. An initial point on the attractor is chosen, and then the average separation as a function of time of a cloud of nearby points is simulated. **(c)** Strange attractor in phase-space.

5.3 Conclusion

The stability of spin bifurcated states was studied with varying trap sizes and powers. The spin flip rate was measured to vary by at least six orders of magnitude, from 100s of Hz, to 100s of MHz, with a very strong, non-monotonous dependence on the condensate occupation. Individual spin flips were time resolved, with an average flip time of 250ps. Good agreement between simulations and experiment was found using a modified spin bifurcation model, where the ratio of cross-/co-spin scattering was ~ 0.6, in contrast with the literature values where it has generally been assumed to be 0 or 1. Further work studying the detuning dependence of this ratio could determine the influence of biexcitons in the phenomenological cross-spin scattering rates. The simulations also predict the existence of self-sustained polarisation chaos, a first for nonresonantly pumped polaritons. Further work exploring the dependence of the polarisation states on *both* power and trap size could yield further insight into the origins of noise and disentangle spatial effects (e.g. exciton/free carrier diffusion) from the density effects studied here.

An interesting application of this chapter is the possibility of using trapped polariton condensates as random number generators. Since the spin flipping is stochastic, sampling the handedness of the polarisation at fixed intervals produces a series of binary random numbers, where the sampling is limited by the spin flip rate. Current state-of-the-art RNGs using laser diode chaos has sampling rates reaching a few GHz. [138] This is at least an order of magnitude larger than the experimentally-limited measurements presented here, but given simulated flip rates reaching 10GHz and individual flips possibly occurring faster than 50ps, future work might place polariton condensates on par with some state-of-the-art random number generators.

Chapter 6 Nonresonant bistability

Bistability – the existence of two stable states for the same system parameters – is frequently observed in the emission of quasi-resonantly injected polaritons as the pump power is scanned. The pump is slightly blue-detuned from the polariton line, so that at low powers, the injection efficiency is very low and the polariton occupation is very small. As the power and occupation are increased, the polariton-polariton nonlinearities cause a blueshift in the polariton line. This brings the pump laser closer into resonance, causing a further increase in the occupation, which causes a further blueshift. It is this positive feedback that causes the bistability and hysteresis of the polariton emission, which has found applications in the study of polariton hydrodynamics [43], dynamical phase transitions [53], and squeezing [51] to name a few. Additionally, the polarisation dependence of polariton nonlinearities leads to polarisation multistability, [48–50,121] which can be used for the creation of spin memories, [133] logic gates, [139] or switches. [140]

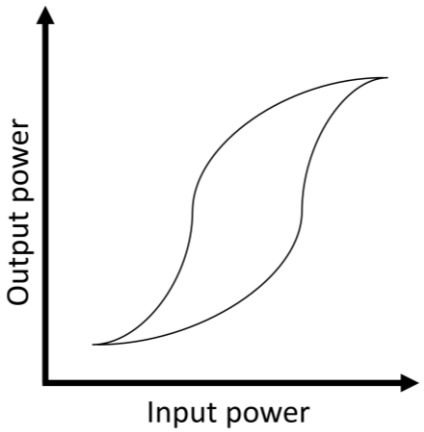

Figure 6.1 Typical hysteresis loop

Despite all this work, resonant optical injection is relatively difficult to implement and scale for applications. Hence there is a strong drive to create bistable polariton systems that are pumped nonresonantly. An example of this is the polarisation bistability caused by electric-field induced birefringence of section 4.3.1. Other demonstrations have also relied on applied electric fields, which can cause intensity bistability due to density-dependent lifetimes of electron-hole tunnelling [36,141]. Theoretical schemes have been proposed to induce polariton bistability through a modulational instability, [142] strongly saturated absorption [143] or between condensate wavefunctions of different parity. [144]

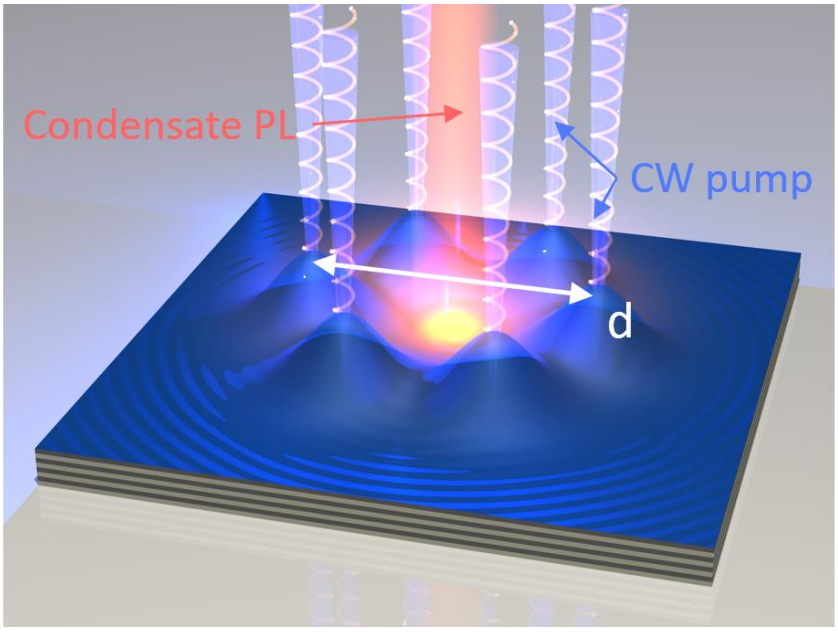

Figure 6.2 **Optical trapping**. The elliptically polarised nonresonant pump is arranged in a hexagon of diameter d. The free-carriers and exciton reservoirs created by the pump blueshift the energy levels, creating a trapping potential for the condensate PL

In this chapter, the spin and occupation of nonresonantly pumped trapped condensates are studied as a function of pump ellipticity.[5] Two distinct and unusual effects are presented: spin inversion – the formation of condensates with elliptical polarisation (spin) of the opposite handedness to that of the nonresonant pump – and spin/intensity bistability with pump power. Both effects had been previously reported by other research groups in similar microcavity samples, [145,146] but were attributed to an interplay of linear polarisation splitting and reservoir nonlinearities within a zero-dimensional model. By studying the dependence of these effects on pump ellipticity and trap size, we reveal that these two phenomena (1) are strongly trap-size dependent, (2) can only be observed within a certain range of pump ellipticity, (3) can be observed independently from each other, and (4) are position-dependent. The zero-dimensional models used in [145,146] provide only partial agreement with these results, for which there is no conclusive explanation yet.

[5] This work is being prepared for publication. Numerical simulations were performed by H. Sigurdsson

6.1 Spin and intensity hysteresis

In the previous two chapters, the nonresonant pumping was presented as 'spin-balanced' i.e. the pump had no specific handedness and the condensate had no pre-determined handedness. This is simplification of the observed behaviour. Although the pump laser is linearly polarised, strain-induced birefringence in the DBRs can cause it to acquire some circular component (like the electrically-induced birefringence discussed in 4.3.1). This ellipticity is partially preserved in the relaxation to the polariton energy, and causes a preference of either spin up or spin down polariton condensates. Which handedness is preferred depends on the sample position and linear polarisation direction, and my previous experiments countered this imbalance by rotating the linear polarisation direction of the pump to cancel the birefringence and create spin-balanced condensates (see also 4.2.2). Nonetheless, some evidence of slight imbalance between the spin-up and spin-down states can already be seen in Figure 5.2, where **(c)** preferred S_z>0 and **(g)** S_z<0.

Now, the parity symmetry is explicitly broken by pumping the condensate with polarised light of varying ellipticity (S_P). Below threshold, the large spin-relaxation [147] means that the PL from the exciton cloud always has very small degree of circular polarisation (<5%) even for fully circular pumping. Above the condensation threshold, however, the condensate spin is strongly dependent on the spin of the nonresonant pump (Figure 6.3a). Even a very small degree of ellipticity in the pump (S_P~0.5%) can lead to strongly circularly-polarised condensates (Figure 6.3c inset). The condensate is imaged on the streak camera, and the nonresonant laser pulses are ramped (linearly increasing power over 5μs).

For large pump ellipticities ($|S_P| > |S_c| = 0.22$, dashed line in Figure 6.3c), the condensate always forms in a spin polarised state of the same sign as that of the pumping, independent of pump power. For smaller pump ellipticities however, the condensate and pump handedness are the same only when below a certain power ($P < P_{inv}$, arrowhead in Figure 6.3a). Above this threshold, the condensate spin is of the opposite sign to that of the pumping. In addition to this condensate spin inversion with power, we observe that at low pump powers ($P < P_{inv}$) there is an additional sharp change in the condensate spin as a function of pump spin. At a critical pump spin S_c an *increase* in the ellipticity of the pumping leads to a *decrease* in the

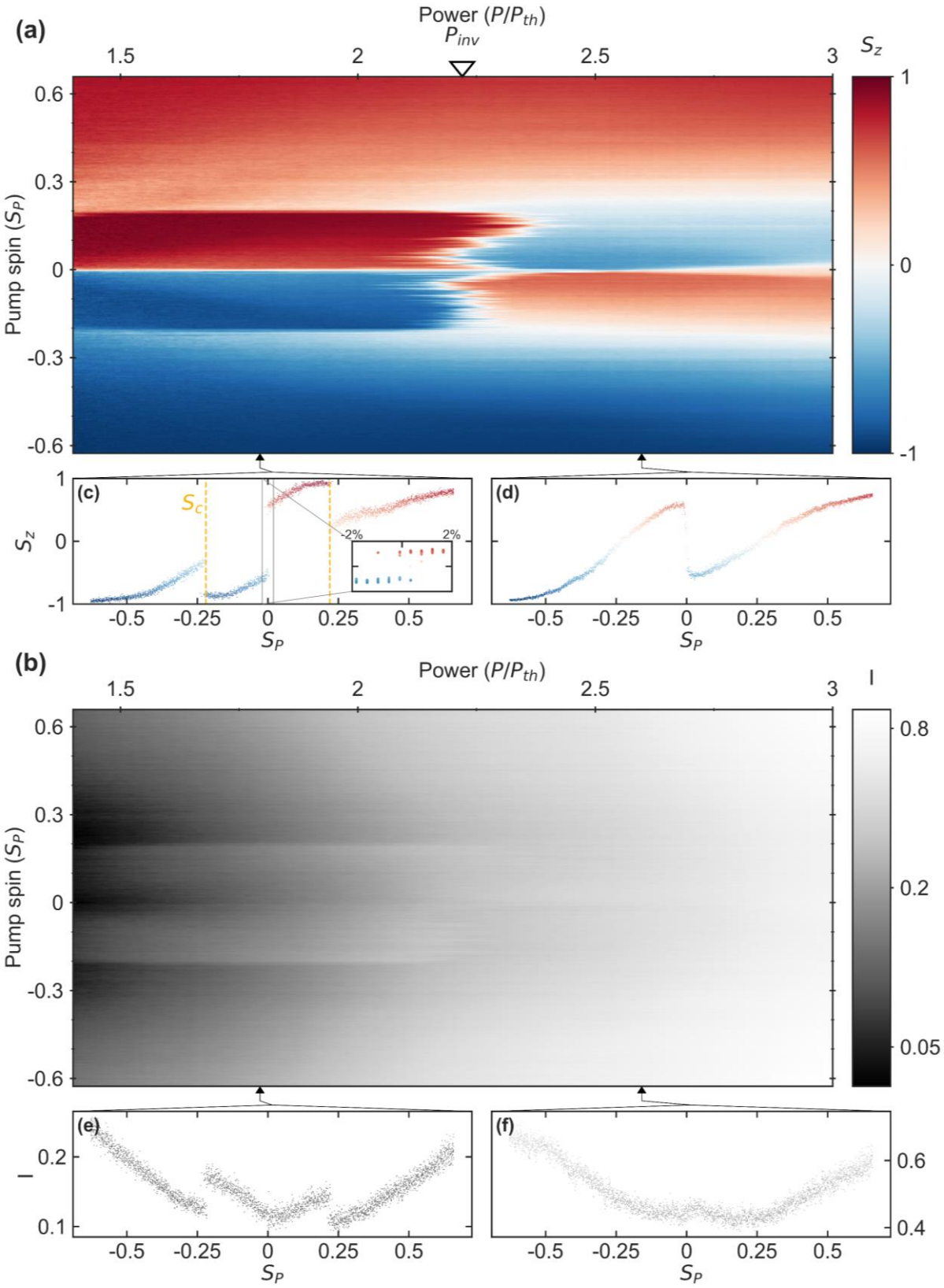

Figure 6.3 **Spin inversion and collapse**. **(a)** Average condensate circular polarisation S_z and **(b)** log intensity I for 10 realisations, as a function of pump circular polarisation S_P and power P. It is normalised to the largest observed intensity. Cross-sections of **(c,d)** S_z and **(e,f)** I for $P = 1.8P_{th}$ and $2.6P_{th}$, respectively.

ellipticity of the condensate. The magnitude of the condensate spin is very high ($S_z > 0.8$) below S_c but drops to $S_z \sim 0.3$ when S_P is just larger than S_c. This leads to three sharp transitions of the condensate spin versus pump spin (Figure 6.3c), while at high pump powers, the condensate spin has only a single sharp transition when the sign of the handedness changes (Figure 6.3d). Other than these sharp transitions, the condensate polarisation S_z changes monotonically with pump polarisation S_P.

The intensity of the emitted light/condensate occupation also varies with both pump power and ellipticity (Figure 6.3b). As expected, the occupation increases with increasing power, but it also unexpectedly increases with increasing pump circularity (Figure 6.3f). This implies pumping/relaxation is more efficient in the presence of a single spin component. This contrasts with previous literature where the presence of both spins allowed the relaxation to overcome the bottleneck. [75] The spin inversion (P_{inv}) and the spin collapse (S_c) can also be seen in the intensity of the emitted light. Just below either of these thresholds, the condensate occupation is fractionally larger than above them (Figure 6.3e). The change in occupation at P_{inv} looks more like a small plateau rather than a decrease (Figure 6.4h,l), and we will see later that it can be reproduced in simulations. The change at S_c, however, cannot be reproduced in simulations and is much more drastic, with the occupation dropping by 30% with a small increase in pump circularity. This is a strong indication that the relaxation dynamics of the excitons and free carriers has a significant spin dependence, possibly due to biexciton formation.

By using triangular nonresonant pulses (linearly increasing and decreasing in power over 10μs), hysteresis can be observed in both polarisation (Figure 6.4a) and intensity (Figure 6.4g). The inversion power P_{inv} (open arrowheads Figure 6.4a) depends on whether the power is being ramped up or down. Hysteresis is present for all pump spin up to the spin collapse ($S_c > |S_P| > 0.01$). The polarisation hysteresis width remains relatively unchanged by S_P (Figure 6.4b-f), but the width of the intensity hysteresis increases with pump circularity (Figure 6.4h-l). Additionally, the two polarisation states between which hysteresis occurs are not necessarily of the opposite handedness (ramp down in Figure 6.4b,f), indicating that the origin of the hysteresis is independent from the spin inversion.

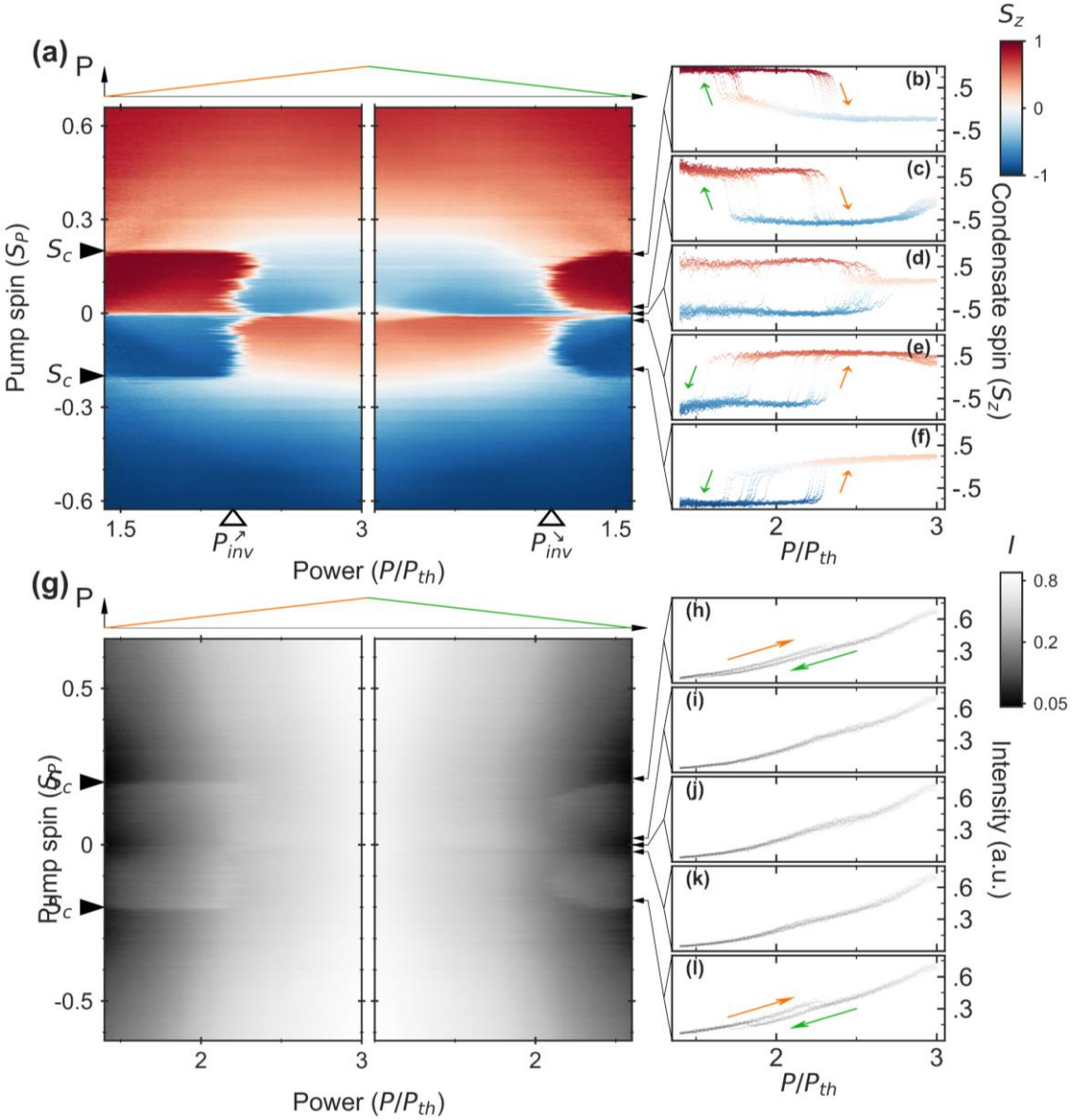

Figure 6.4 **Polarisation and intensity hysteresis**. Average circular polarisation **(a)** and log intensity **(g)** as a function of pump power and circularity, for triangular laser pulses. Hysteresis loops of circular polarisation **(b-f)** and intensity **(h-l)** versus power, for S_P=0.19 **(a,h)**, 0.02 **(b,i)**, 0 **(c,j)**, -0.02 **(d,k)**, and -0.18 **(f,l)** The white regions in **(a)** are the regions of zero average circular polarisation. They can be due to either the condensate being unpolarised in the circular basis or to different realisations having opposite spins as in **(d)**

In the limit of linearly polarised pumping we recover the results from the previous chapters (Figure 6.4d). The condensate stochastically forms in either a spin up or a spin down state with equal probability (Chapter 4). Once the condensate is formed, noise induces spin flips between the two spin states before they collapse into a linearly polarised state at higher powers (Chapter 5). The dynamical instability to a linearly polarised state can also be seen in Figure 6.4a for slightly elliptical pumping ($|S_P| < 0.02$) and high powers ($P > 2.5P_{th}$).

6.1.1 Trap size and position dependence

The observed spin inversion and hysteresis have strong dependencies on the optical trap size (d in Figure 6.2). Previously, the regions of brighter emission and stronger circular polarisation were bounded by two critical thresholds P_{inv} and S_c. However, changes in the trap size reveal that these unusual regions (U) can have more complicated boundaries in the P-S_P plane (Figure 6.5), which radically shift even for diameter changes of <10%.

For smaller trap sizes (Figure 6.5a), the bright regions U exist for all values of pump spin and down to the lowest pump power at the condensation threshold (P_{th}). These regions display hysteresis in both spin and intensity with pump power, and it is possible to observe hysteresis without spin inversion (black arrowhead Figure 6.5). As the trap size increases, the U regions shrink: they no longer occur for all values of pump spin, nor do they occur down to the condensation threshold (Figure 6.5b). This shrinking continues as the trap size is increased, until the U manifold becomes so unstable that only some condensate realisations explore it, leading to unpolarised regions in the average polarisation (Figure 6.5c). For sufficiently large trap sizes, U disappears completely.

While the bright regions shrink and disappear, the regions where spin inversion occurs grow, and occur for a larger range of powers and pump ellipticities. For smaller trap sizes the spin

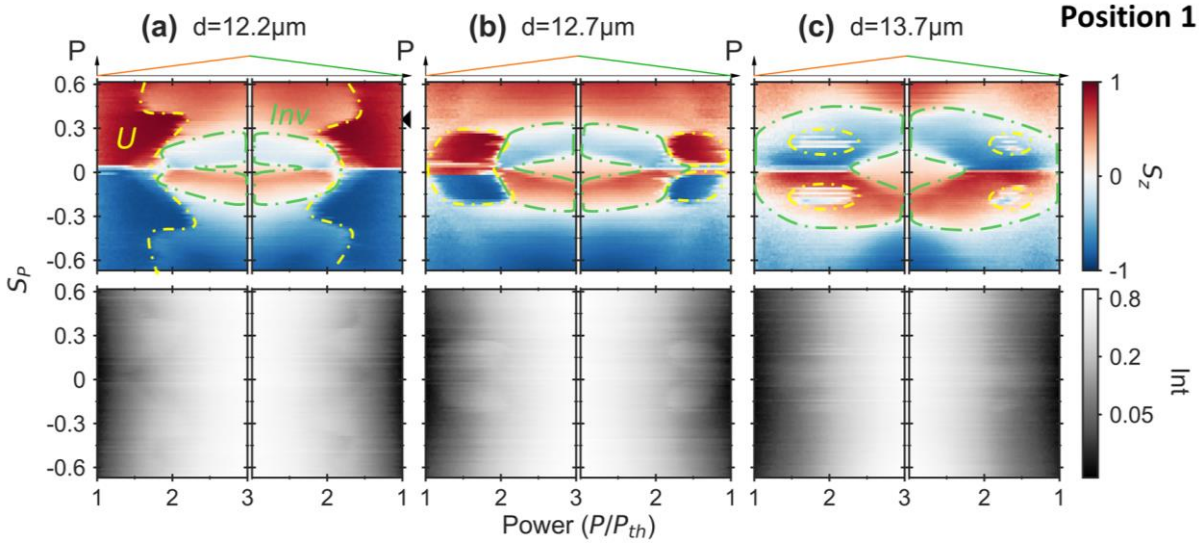

Figure 6.5 **Trap size dependence**. Average polarisation (top row) and intensity (bottom row) as functions of pump circularity and power, for three different trap sizes **(a-c)**. Yellow dashed lines are a guide to the eye marking the unusual regions U. Green dashed lines mark the spin inversion regions.

inversion only occurs at powers above the threshold at a critical power P_{inv}. For large traps however, the spin inversion can occur even at condensation (Figure 6.5c). Simultaneously, spin inversion is observed for a larger range of pump ellipticities (S_P) as the trap size increases. In contrast with the bright regions U, the spin-inverted regions never show any hysteresis with pump power.

The specific shape of the bright regions and the spin-inverted regions, and their dependence on trap size, differs at different sample positions (Figure 6.6). For some sample positions and trap sizes, much higher powers are needed to observe spin inversion (Figure 6.6a). In other positions, the smallest trap sizes do not present any spin inversion (d=10.7μm Figure 6.6b).

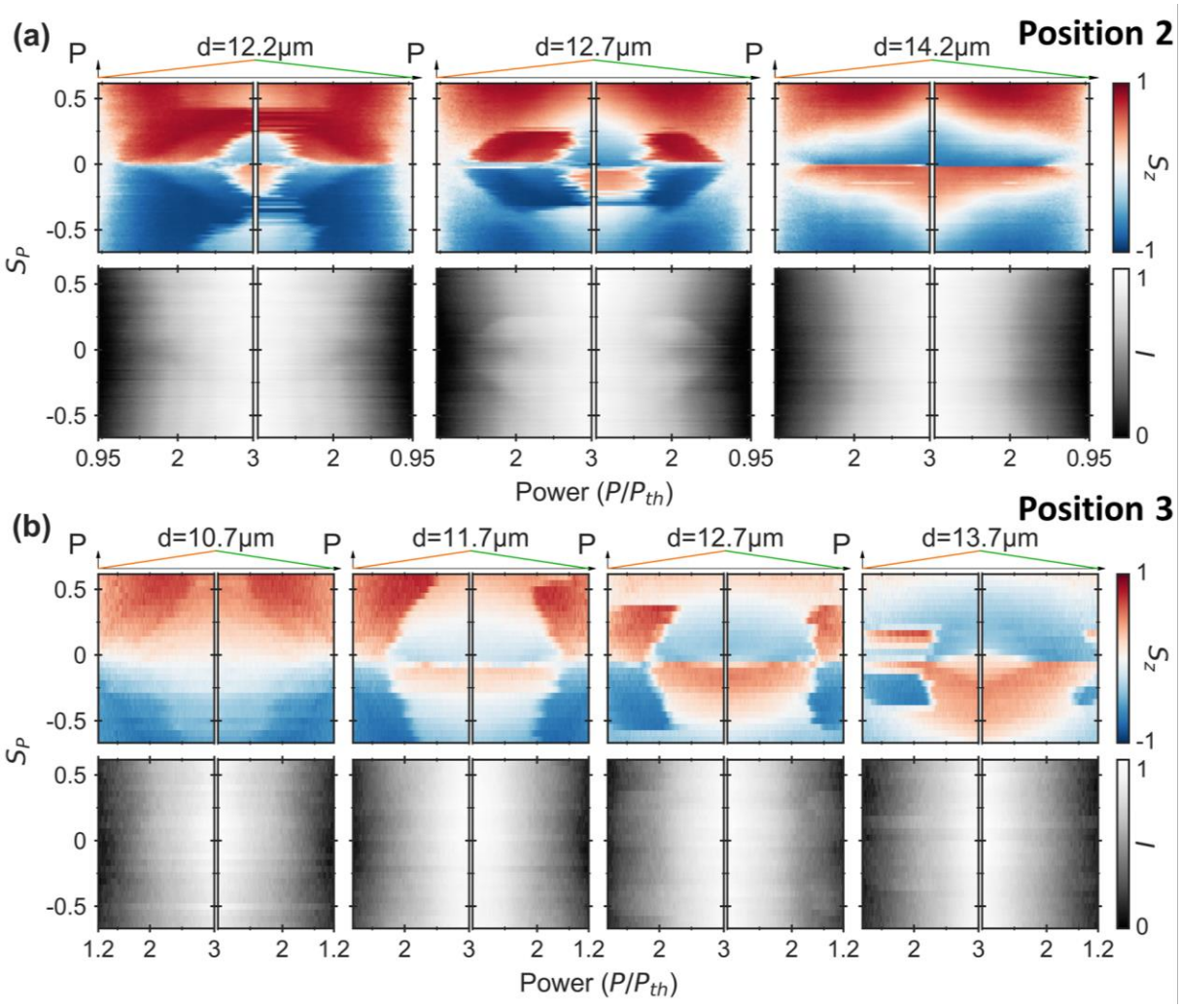

Figure 6.6 **Sample position dependence**. Same as Figure 6.5, but at two different sample positions **(a)** and **(b)**. The slight asymmetry between $S_P > 0$ and $S_P < 0$ is likely due to a small birefringence in the DBRs, causing a slight change to the input polarisation.

The length scale over which these changes occur is relatively small: moving the sample a few tens of microns can lead to significant variation in the specific power, pump spin and trap size dependences. Hence, sample disorder is playing some role in driving spin inversion and/or hysteresis. However, there is no measurable disorder in the sample's polariton PL or energy on the length scales of the condensate, indicating that the disorder is not directly affecting the condensate. Despite the variability with sample position, the main qualitative dependence on trap size remains. For the smallest traps, the strongly polarised, bright, hysteretic regions are largest and spin inversion can even disappear. As the trap size is increased, the hysteretic regions shrink and only appear for a finite range of pump powers and pump spin magnitudes, while the spin inversion region grows. Finally, for the largest traps, the bright hysteretic regions disappear completely and only spin inversion remains.

6.1.2 Spatial profiles

So far, the spatial degrees of freedom of the condensate have been averaged over by imaging on the streak camera. To measure the polariton spatial profiles, the nonresonant laser is chopped into short (0.5-1μs), square (1ns rise-time) pulses of variable amplitude. Ten condensates realisations are made and their spatially-resolved PL is imaged on the CCD. From these images, the condensate polarisation and occupation are extracted by spatially averaging over a 5μm diameter circle around the centre of the condensate. Although the pulses are not ramped, both the spin inversion and the unusual regions U can still be seen in the spatially-averaged polarisation and intensity maps (Figure 6.7b), as well as the general trend of the U regions disappearing for larger trap sizes.

Although the polarisation and occupation have a strong dependence on spatial properties (trap size and sample position), their profiles are unaffected by changes in power or pump circularity (Figure 6.7a). It might appear as if the spin and intensity profiles increase in spatial extent with increasing power (clearly seen for trap size 13.7μm), but this can be accounted for by an increase of the signal-to-noise on the CCD. Hence, the profiles remain the same independently of pump spin (4,5) and of whether the condensate is in a spin-inverted region (2,4,6,8) or in a U region (1,3,7).

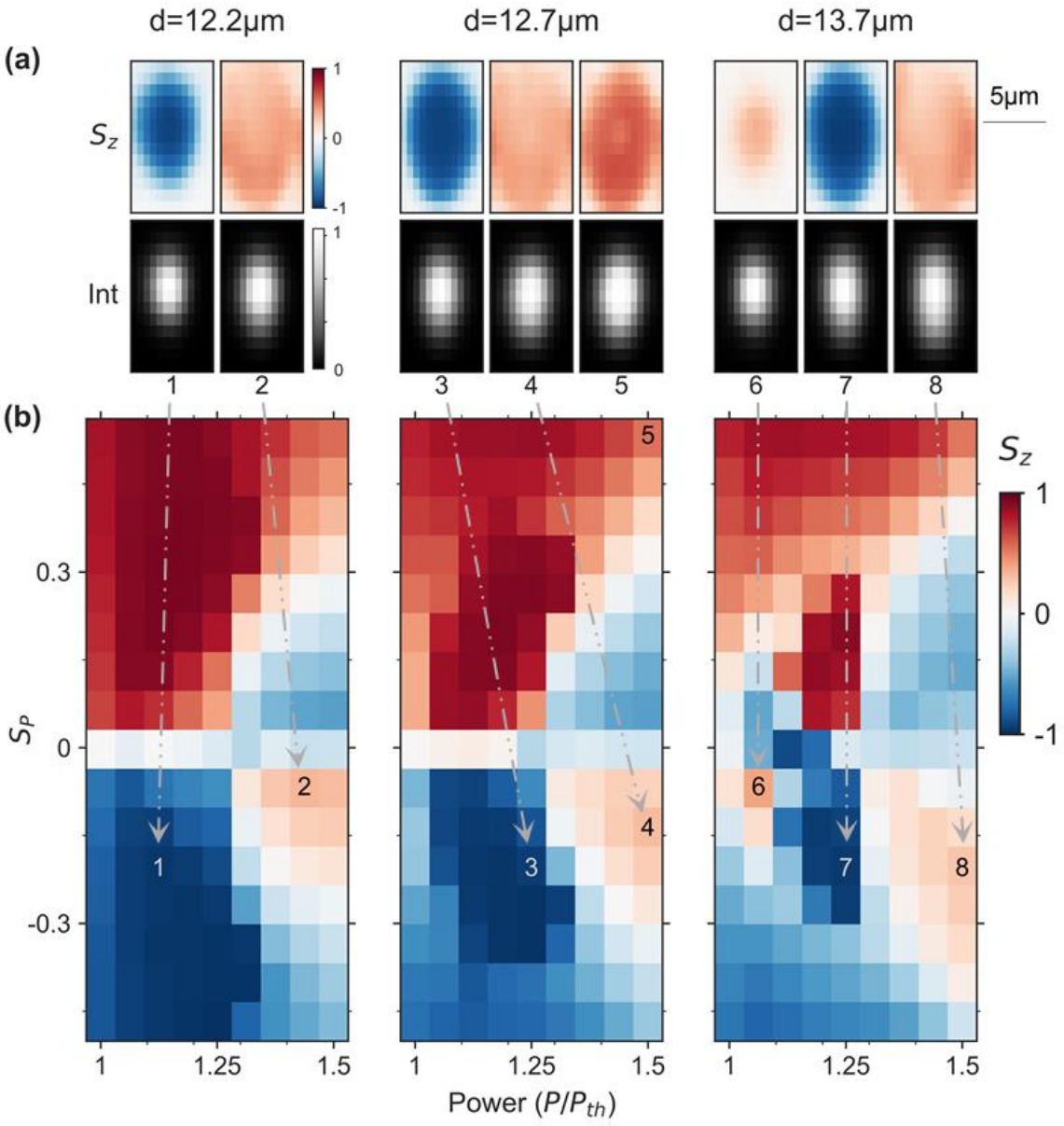

Figure 6.7 **Spatial profiles**. **(a)** Example polarisation and intensity images. **(b)** Average circular polarisation extracted from the images, for three different trap sizes as a function of pump circularity and power, for 10 condensate realisations.

6.1.3 Energy

Optically trapped condensates can easily condense in higher order trap modes instead of the Gaussian-like ground state, due to a competition of trapping and gain. [88,97,148] Such multimode behaviour lies beyond the simple single-mode theories of the previous two chapters. Hence, before moving on to discuss possible explanations for this phenomenology, the polariton energy spectra are measured. Condensates are created with square 100μs pulses, and the PL is polarisation-resolved in the circular basis and measured through a 60μeV

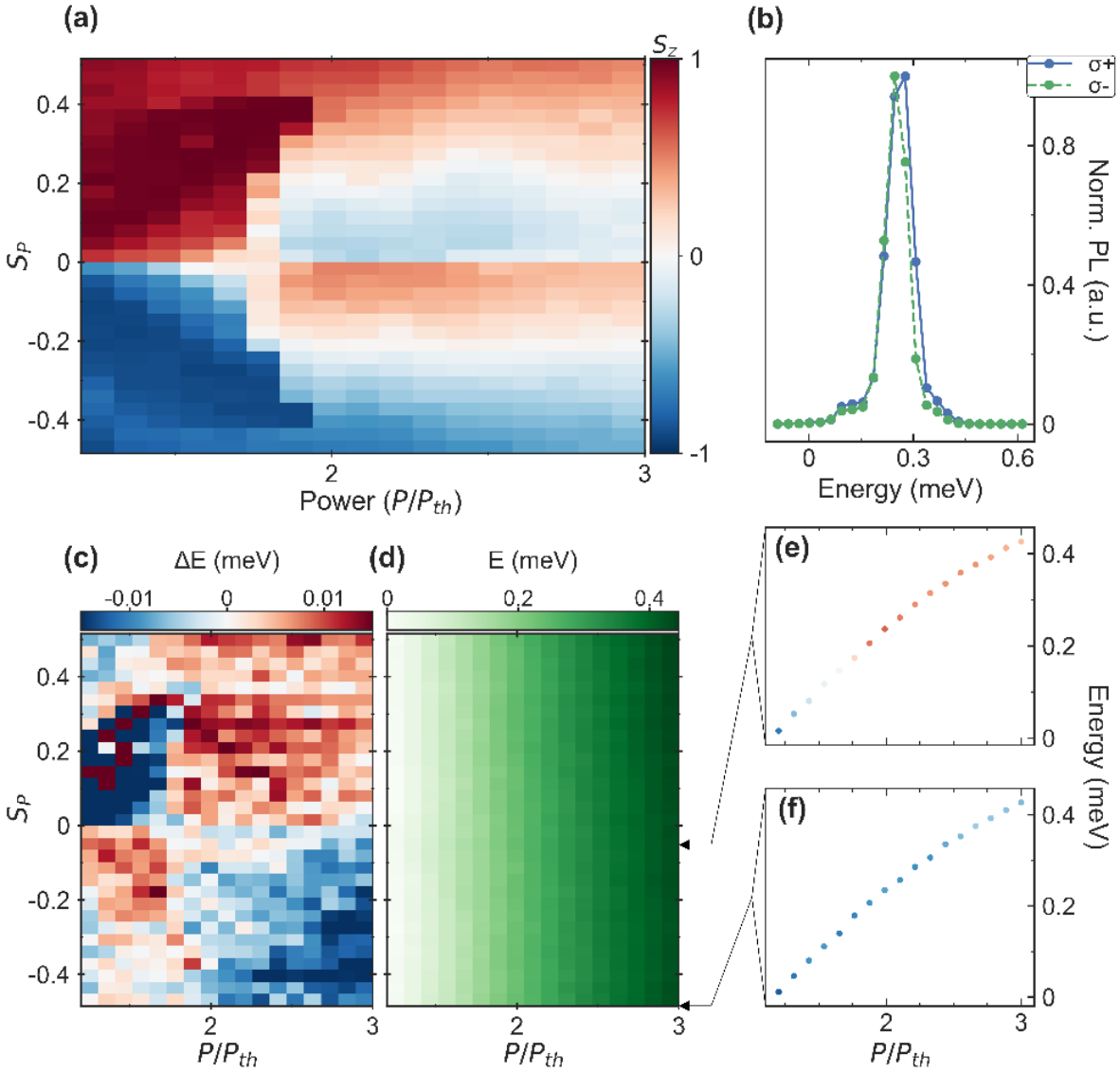

Figure 6.8 **Condensate energies**. **(a)** Average spin extracted from the polarisation resolved spectra. **(b)** Example traces showing small energy splitting between σ_+ and σ_- Energy splitting **(c)** and average energy **(d)** as a function of power and pump ellipticity. Average energy versus power for **(e)** $S_P = -0.05$ and **(f)** $S_P = -0.48$

resolution spectrometer. This maximum resolution is broadened due to unmatched NAs at the input, leading to linewidths ~70μeV. The polariton energy is extracted by least-square fitting a gaussian to the spectra, and there is no evidence of higher-energy modes being present (Figure 6.8b).

The energy blueshifts by ~400μeV from $1.2P_{th}$ to $3P_{th}$ (Figure 6.8d), with a slightly sub-linear dependence on power (e,f) that is independent of pump ellipticity and shows no correlation with the unusual regions U or the spin inversion. The energy difference between σ_+ and σ_- is always less than one sixth of the linewidth/one third of a CCD pixel, so it could be argued that there is no measurable energy difference. However, the fitted data shows some correlation between the energy difference and the U regions (Figure 6.8c). Two clear trends can be seen. Firstly, at high power, the condensate component of the same handedness as the pump has a higher energy, independently of which component has a higher occupation. This trend was also observed in multiple datasets at different sample positions, providing further confirmation. It makes sense intuitively that the polariton mode of the same handedness as

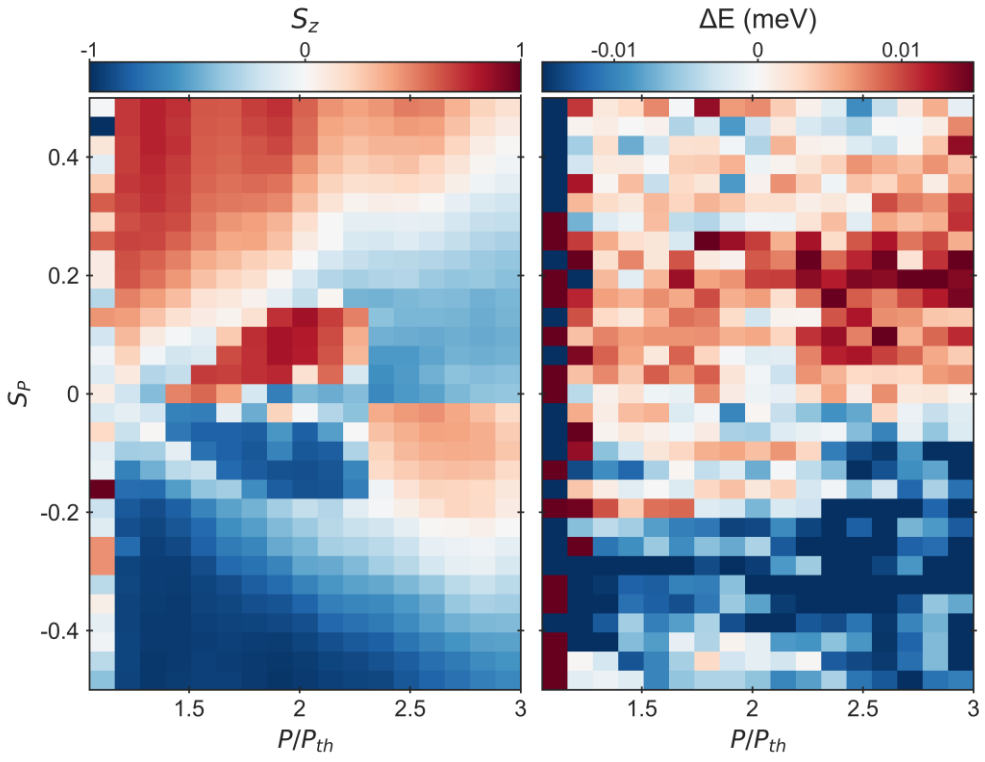

Figure 6.9 **Condensate energy splitting**. **(a)** Average spin extracted from the polarisation resolved spectra. **(b)** Energy splitting between σ_+ and σ_-, showing that the inversion of splitting sign does not always occur.

the pump would have higher energy, as the interactions with the exciton reservoir are expected to be stronger for the same spin. [149] Secondly, in the unusual regions U, this trend is inverted, meaning that the component with higher occupation, and of the same handedness as the pump, has *lower energy*. This redshift is completely counterintuitive, but it must be taken with a dose of scepticism, since the splittings are very small and have not been seen in other similar datasets (Figure 6.9). Given that one of the polarisation components is always very weak in U, it is possible that this redshift is just an artefact of the fitting procedure (in multiple positions in $0 < S_P < 0.3$ and $1.2 < P/P_{th} < 1.75$ the signal was so weak that the fitting failed).

In summary, the spin inversion and hysteresis do not require higher-order trap modes, and there is no conclusive correlation with the circular component energies. Further experiments resolving the energy in a different polarisation basis, and for a larger range of trap sizes and sample positions could prove whether polarisation splittings are playing a role in driving the spin inversion or the bistability.

6.2 Insufficient Gross-Pitaevskii and possible extensions

Two of the results presented so far, namely spin inversion and polarisation hysteresis, have been recently observed in similar semiconductor microcavities by the group of Lagoudakis in Southampton. [145,146] Both effects were attributed to the interplay between energy splitting of linear polarisation modes and reservoir nonlinearities. This explanation was backed by numerical simulation of Gross-Pitaevskii equations similar to those in previous chapters, but now including reservoir nonlinearity (g_1 and g_2):

$$\begin{aligned} \frac{dn_\uparrow}{dt} &= P_\uparrow - \Gamma_x n_\uparrow - (R_s|\psi_\uparrow|^2 + R_o|\psi_\downarrow|^2)n_\uparrow \,, \\ \frac{dn_\downarrow}{dt} &= P_\downarrow - \Gamma_x n_\downarrow - (R_s|\psi_\downarrow|^2 + R_o|\psi_\uparrow|^2)n_\downarrow \,, \end{aligned} \tag{6-1}$$

$$\frac{d\psi_\uparrow}{dt} = \frac{1}{2}\left[\left(R_s n_\uparrow + R_o\, n_\downarrow - \Gamma_p\right) - i(\alpha_1|\psi_\uparrow|^2 \;+\; \alpha_2|\psi_\downarrow|^2 + g_1 n_\uparrow + g_2 n_\downarrow)\right]\psi_\uparrow$$
$$-\frac{1}{2}(\gamma - i\,\varepsilon)\psi_\downarrow + dW_\uparrow\,,$$

$$\frac{d\psi_\downarrow}{dt} = \frac{1}{2}\left[(R_s\, n_\downarrow + R_o\, n_\uparrow - \Gamma_p) - i\,(\alpha_1|\psi_\downarrow|^2 \;+\; \alpha_2|\psi_\uparrow|^2 + g_1 n_\downarrow + g_2 n_\uparrow)\right]\psi_\downarrow$$
$$-\frac{1}{2}(\gamma - i\,\varepsilon)\psi_\uparrow + dW_\downarrow$$

Numerically solving Eq. (6-1) using 800ns triangular pump pulses for varying pump circularity $(P_\uparrow - P_\downarrow)/(P_\uparrow + P_\downarrow)$, can indeed reproduce some of the experimental behaviour (Figure 6.10). As noted in [145,146], both spin inversion and spin bistability that are similar to experiment can be seen as long as $R_s > R_o$ and $g_1 > g_2$. The model also reproduces the increase in occupation with increasing S_P, although the effect is smaller than in the experiment. The position dependence of the inversion threshold could also be explained if the feeding rate $(R_{s/o})$, reservoir $(g_{1/2})$ or polariton $(\alpha_{1/2})$ nonlinearities are assumed to vary with sample position. [145]

The first clear difference with experiment is that the absolute values of pump circularity for which spin inversion occurs are much smaller (~0.06 in simulations compared to ~0.2-0.5 in experiments), but this could simply be due to spin relaxation from the nonresonant pump. However, there are some qualitative differences that question the validity of the model altogether:

- The simulations show that the circular polarisation in the spin-inverted regions decreases with pump circularity (Figure 6.10d-f), while the *opposite* trend is observed in experiment. Simulations also show no sharp transition of the condensate spin when changing the handedness of the pump.
- While one could argue that the simulations show some semblance of unusual regions U, they occur for all values of pump circularity and do not show a critical spin collapse S_c or complicated boundaries.
- The width of the simulated hysteresis loops grows with S_P (Figure 6.10b,c), which is not the case in the experiment.

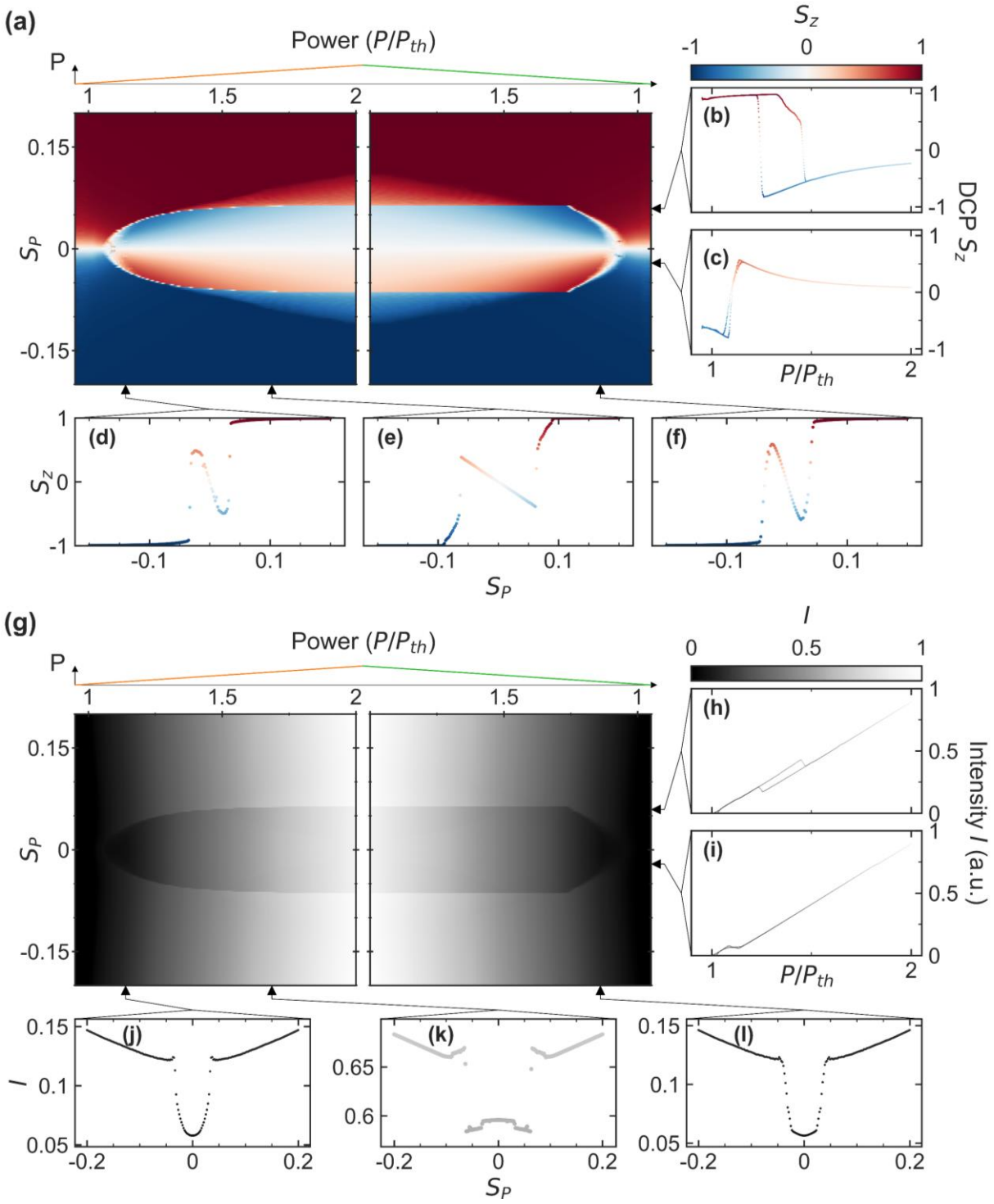

Figure 6.10 **Simulations**. Average spin **(a)** and intensity **(g)** over 100 realisations, for power being ramped up and down over 800ns. Polarisation and intensity versus pump power – S_P =0.06 **(b,h)** and -0.02 **(c,i)** – and pump circularity – P/P_{th} =1.14 **(d,f,j,l)** and 1.69, **(e,k)**. Parameter values are $\alpha_1 = 0.011\text{ps}^{-1}$, $\alpha_2 = -0.5\alpha_1$, $g_s = 0.025\text{ps}^{-1}$, $g_o = -0.1g_s$, $\Gamma_p = 0.15\text{ps}^{-1}$, $\Gamma_X = 0.7\Gamma_p$, $R_s = 0.001\text{ps}^{-1}$, $R_o = 0.6R_s$, $\varepsilon = 0.06\text{ps}^{-1}$, $\gamma = 0.1\varepsilon$

- No energy difference between ↑ and ↓ is present in the simulations.
- Finally, while the experiment always displays spin bifurcation in the limit of linearly-polarised pumping (Figure 6.4d), the simulations do not. This is because spin inversion and hysteresis require $R_s > R_o$ and $g_1 > g_2$, which are conditions that suppress the spin bifurcation.

These qualitative differences between experiment and theory could not be accounted for with a scan of parameter values (ongoing) and indicate that the zero-dimensional model of Eq. (6-1) is missing some relevant dynamics. Additional terms accounting for energy splittings between circular polarizations, or spin relaxation between reservoirs, are all found to be unable to explain these discrepancies. Simulations including the spatial degrees of freedom of polaritons and TE-TM splitting, are found to be qualitatively the same as Figure 6.10. At present therefore, new spin dynamics have been observed in the condensate, but they are yet to be understood.

6.3 Conclusion

This chapter showed spin inversion and hysteresis in polarisation and intensity. A detailed dependence on pump power, circularity and trap size demonstrated that these effects can be observed independently from each other. Spin inversion can occur without hysteresis and hysteresis occurs in connection with unusual regions U of brighter emission and stronger degree of circular polarisation. This indicates that both effects have two independent origins. Despite the condensate spin and intensity being strongly dependent on spatial properties – trap size and sample position – the condensate profiles show no spatial features and condensation always happens in the ground state. Spatial features were also not seen in the below-threshold PL and energy. Small splittings are observed between circular polarisation components, likely due to reservoir nonlinearities, but no conclusive correlation is found with spin inversion or hysteresis.

Both spin inversion and nonresonant bistability have been recently explained within a zero-dimensional, single-mode, mean-field theory. [145,146] This theory is successful in reproducing spin inversion and hysteresis but is unable to qualitatively or quantitatively

capture their dependence on pump circularity, the complex boundaries of the unusual regions U, or their dependence on trap size and sample position.

Although there is no conclusive explanation yet, it is likely that the origin of the spin inversion and/or hysteresis requires consideration of spatial degrees of freedom and of spatial inhomogeneities. Given that no spatial inhomogeneities can be seen in the PL at the polariton emission energy (above or below threshold) it is likely that the spatial dynamics are occurring at higher energies (exciton reservoirs/free carriers) or in dark states (biexcitons/dark excitons). A possible explanation could be that as the exciton reservoirs diffuse, TE-TM splitting causes a spin-precession of their spin. The resultant spin rings could have complicated overlaps with the condensate wavefunction, leading to different spins dominating the gain. The fact that there are no oscillations with pump power, circularity or trap size makes this explanation unlikely. Another explanation could be for the relaxation efficiency to be spin dependent, which is supported by the dependence of the condensate occupation on pump ellipticity. This could lead to competing relaxation paths and bottlenecks that could have complicated dependencies on power and spin. [73,74] Such relaxation paths might need to include the effects of biexcitons and dark excitons. Finally, it is possible that the nuclear spin polarisation is playing some role in the formation of bistability. The circularly polarised pumping could be driving an alignment of the nuclear spins, which would then explain the unusual regions polarisation and energy. However, further analysis is needed to fully determine which of these effects is the driving force behind the spin inversion and the bistability.

Chapter 7 Coupled condensates

Quantum simulators – devices designed to emulate arbitrary quantum systems – promise to transform the way we approach emergent phenomena in condensed matter physics. [6,150] Although there is a variety of physical implementations for a quantum simulators, [6–9,151] the use of lattices has become a common feature as they intuitively map to the geometry of solids. Polariton lattices are promising candidates for quantum simulation due to their large, tuneable nonlinearities, the spontaneous emergence of quantum states, and the possibility of integration into semiconductor devices. A variety of techniques have been developed to create potential landscapes for polaritons, [15] and implemented in a variety of lattice geometries, from simple square [10,12,14,152,153] and hexagonal [13,154,155] to Kagome [156] and Lieb [157–159] lattices. This chapter explores the possibility of using a patterned nonresonant pump to create lattices of controllably-coupled, optically-trapped condensates.[6] The advantage of this approach is the dynamic creation of the lattice, which allows different geometries to be studied on a single microcavity and the possibility of actively countering spatial disorder.

The first section demonstrates the building-block of any lattice: two controllably coupled condensates. Tunnelling between spin bifurcated condensates causes their spins to be correlated and two phases are observed depending on the sign of the correlation: ferromagnetic and antiferromagnetic. A controllable transition between these two phases is demonstrated by tuning the shape of laser pattern, and an extension of the models used in previous chapters is able to capture the main phenomenology. The second section of this chapter focuses on larger spin chains. A controllable transition between magnetic phases is observed for a 4-condensate closed chain and is well reproduced within the mean-field

[6] Part of this work has been published in [160,161]. Experimental and simulations work was done with Dr. H. Ohadi

model. In larger chains, spin domains are shown to be strongly affected by sample disorder, impeding the observation of controllable transitions and severely limiting the scalability of a simple approach. Finally, a random search algorithm is shown to be able to counteract sample disorder, demonstrating the flexibility of patterned nonresonant fields for lattice creation.

7.1 Ferromagnetic-antiferromagnetic transition

The building block of any lattice is two coupled sites. The optical pattern used to create two coupled condensates is shown in Figure 7.1. Ten spots are arranged in two adjacent hexagons to create two condensation centres. The pattern is made using MRAF, and the middle two pump spots (the barrier, b) have variable amplitude.

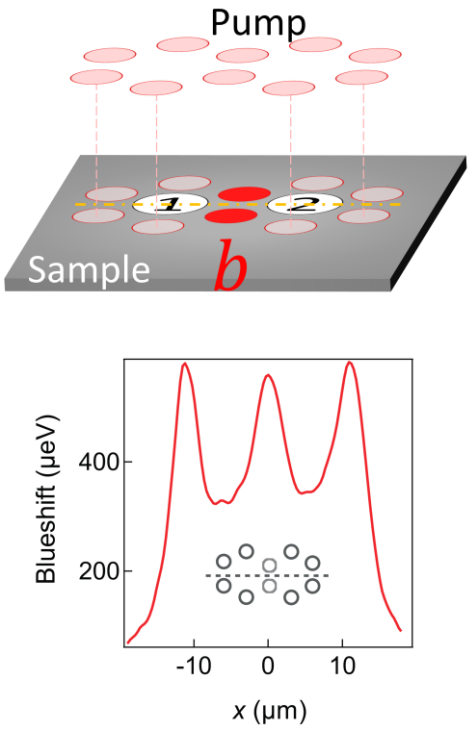

Figure 7.1 **Schematic pumping geometry**. The two middle spots (b) have a variable amplitude relative to the other spots, creating a variable energy potential between the two condensates. For b of similar intensity to the rest of the pattern the barrier is measured to be $\sim 200 \mu eV$. Modified from [161]

The two trapped condensates each exhibit a spin bifurcation (Chapter 4): above a critical occupation they magnetise and stochastically choose their handedness (↑ or ↓). For sufficiently large hexagons, the two condensates behave as two independent condensates and four spin configurations are observed: $\uparrow -\uparrow$, $\uparrow -\downarrow$, $\downarrow -\uparrow$ and $\downarrow -\downarrow$. As the hexagons are made smaller, the condensates still magnetise but their polarisations become correlated (Figure 7.2). Two main configurations are observed: ferromagnetic (F) and antiferromagnetic (AF). When the condensates are ferromagnetic their polarisations correlate leading to each realisation stochastically being either $\uparrow -\uparrow$ or $\downarrow -\downarrow$. When they are antiferromagnetic the two states are $\uparrow -\downarrow$ and $\downarrow -\uparrow$. Given that most of the polarisation dynamics occurs in the circular basis, a useful way of visualising the steady states is by

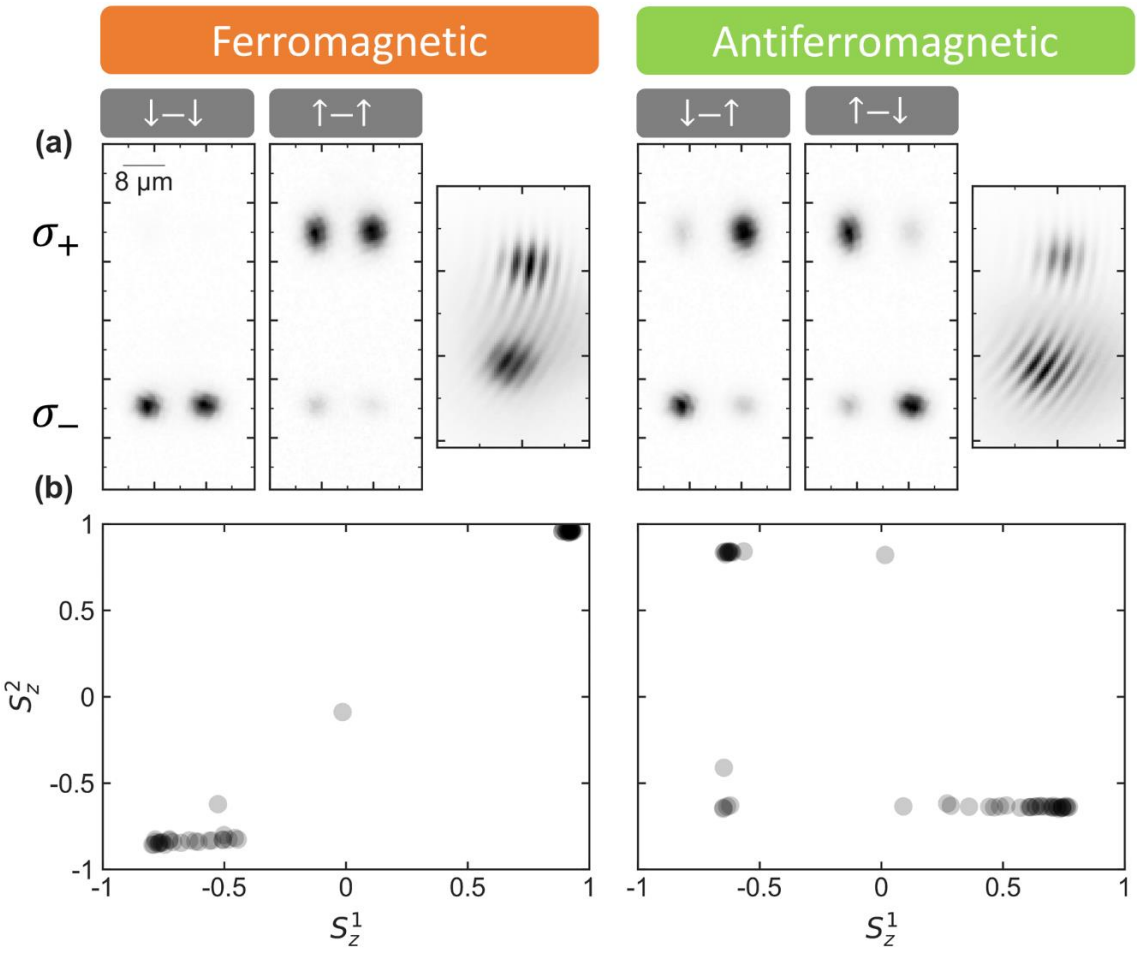

Figure 7.2 **Coupled spins**. **(a)** Polarisation-resolved real-space images of the polariton PL. The slight distortion in the σ_- component is due to the Wollaston prism. The fringe images are obtained in σ_+ by using an expanded condensate as a phase reference. **(b)** Circular polarisation of one condensate versus the other, extracted from CCD images of 50 realisations.

plotting the degree of circular polarisation of one condensate versus the other (S_z^2 vs S_z^1, Figure 7.2b). In such a plot, it becomes clear that most of the condensate realisations really do end up in either one of two states and that the correlation between the condensates spins is strong.

In addition to the spins being correlated, the two condensates also display phase coherence. An expanded image of one of the condensates is overlapped with both, leading to interference fringes (Figure 7.2a-b). Not all realisations, for constant experimental conditions, show strong fringe contrast and some realisations show no fringes at all. The fact that some show any phase coherence at all means that, to some degree, the coupling between the condensates is coherent. Extracting quantitative phase information from the interference images is made

quite difficult by the phase curvature of the reference field (due to misalignment). But qualitatively speaking, ferromagnetic condensates are in phase, while antiferromagnetic condensates have a phase difference between $\pi/2$ and π. [161,162]

The correlation between the spins does not necessarily imply that they are coupled in the steady state. The correlation could arise due to transient coupling during the condensation process, that is then frozen into the steady state due to the stability of these trapped condensates. This was tested by resonantly exciting the condensate on the right with a right-circularly polarised laser and time-resolving the σ_+ PL of each condensate on PMTs (Figure 7.3). The resonant pulse causes a spin flip of both condensates, even though it has no spatial overlap with the condensate on the left. This proves that the two condensates are spin coupled, not just phase coherent and spin correlated.

By changing the nonresonant pump pattern, it is possible to controllably transition between the FM and AFM regimes. The relative intensity of the two middle spots (b in Figure 7.1) is changed from 0.2 to 1.3, while the rest of the pattern is kept constant. The real-space PL is

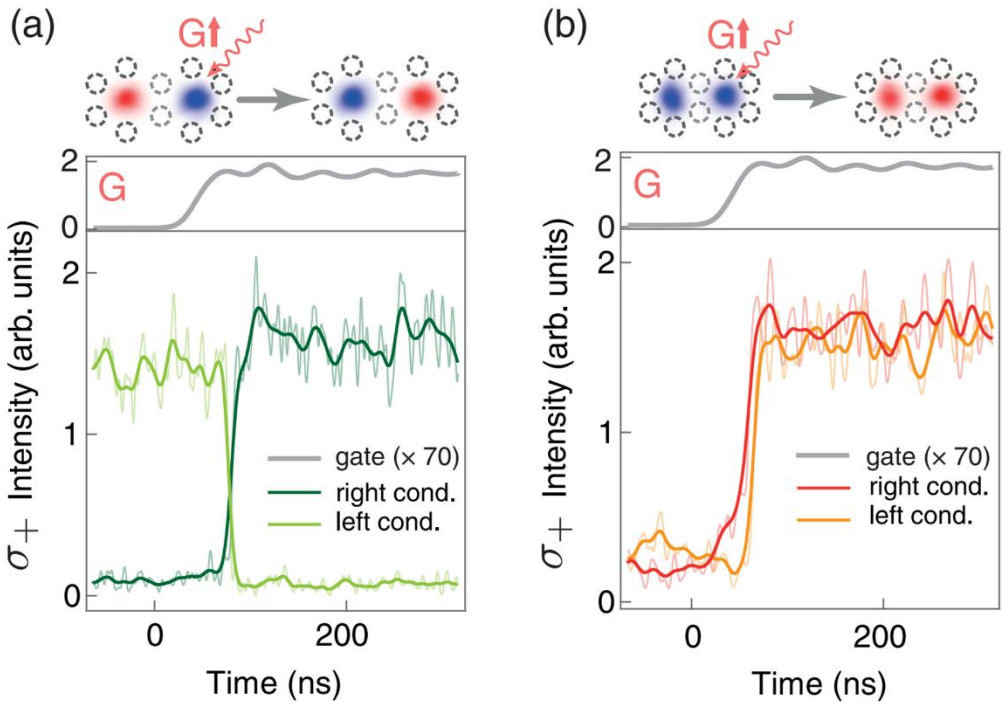

Figure 7.3 **Coupled spin flips**. Time-resolved, σ_+ PL of two coupled condensates. A weak, resonant, σ_+ gate G is applied on the right, σ_- condensate. The condensate pair switches from ↑↓ to ↓↑ in **(a)** the AFM state and from ↓↓ to ↑↑ in **(b)** the FM state. [161]

recorded on the CCD and the circular polarisation of both condensates is measured for 50 realisations at each barrier value (Figure 7.4a,b). Changing the intensity of the two middle spots also changes the condensate occupation and, for low barriers ($b < 0.25$), the condensates are unpolarised in the circular basis since they are below the spin bifurcation threshold (c-i, purple). As the barrier and the condensate occupation is increased, the two condensates bifurcate with correlated spins but instead of two isolated ferromagnetic states, there is a continuum of states along the $S_z^2 = S_z^1$ line (c-ii, blue). This continuum is likely an artefact due to time-averaging over a small number of spin flips during the 10μs CCD exposure, similar to Chapter 5 but with correlated spin flips in this case. Further increase in b

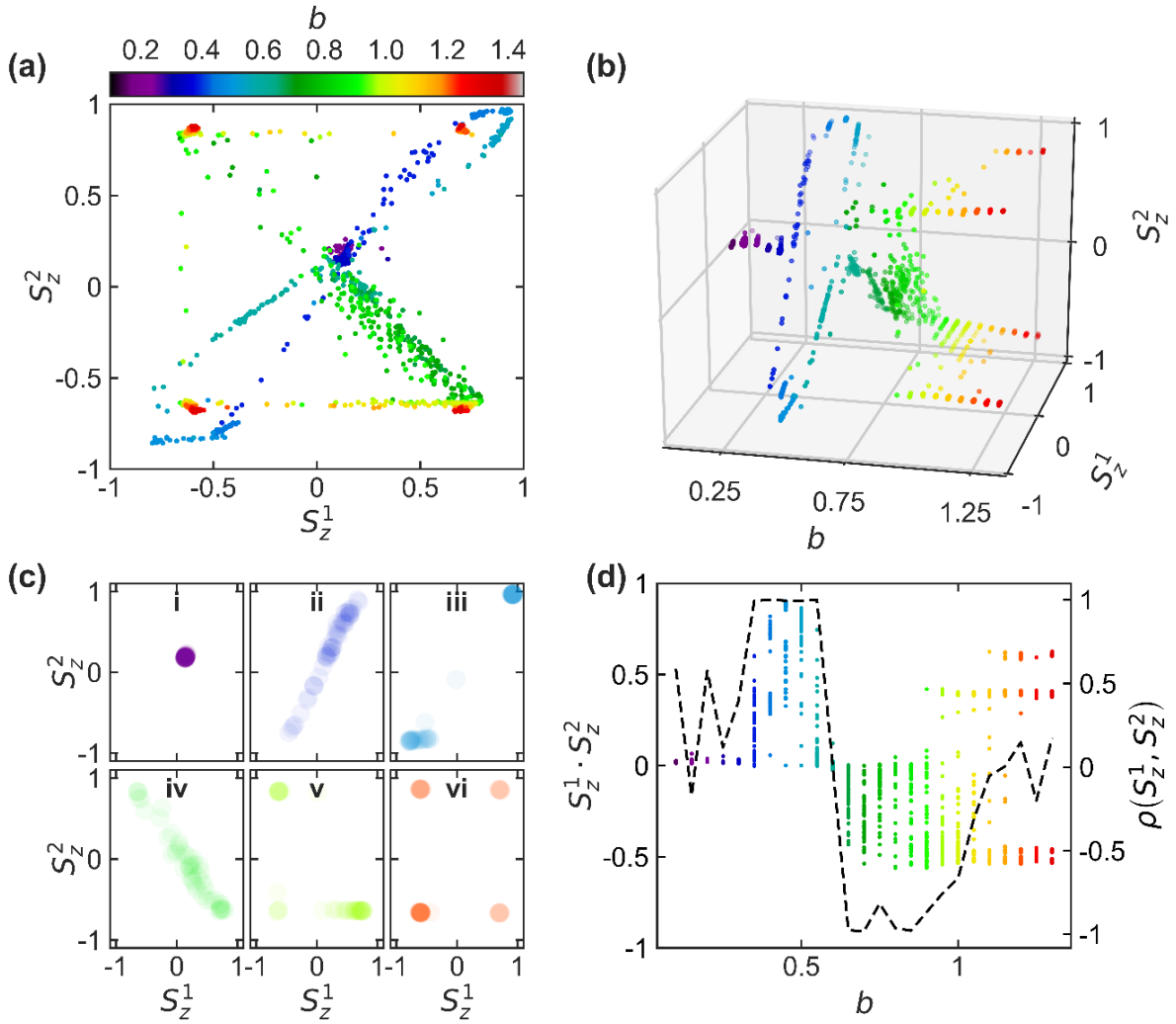

Figure 7.4 **Barrier dependence**. At each barrier value, 100 condensate realisations are made and imaged on a CCD, from which the condensate circular polarisation are extracted. **(a,b)** Circular polarisation of one condensate versus the other $S_z^{1,2}$ for all values of relative barrier strength b (colour coded). **(c)** S_z^1 vs S_z^2 for b =0.2 (i), 0.35 (ii), 0.45 (iii), 0.85 (iv), 0.95 (v), and 1.2 (vi). **(d)** $S_z^1 \cdot S_z^2$ and Pearson correlation (dashed) between S_z^1 and S_z^2 as a function of barrier

leads to a stabilisation of the ferromagnetic states and all realisations are in either $\uparrow -\uparrow$ or $\downarrow -\downarrow$ (c-iii, light blue). At $b = 0.6$ there is a transition and the correlation between the spins changes sign. Again, spin flips lead to a continuum of states along the $S_z^2 = -S_z^1$ line (c-iv, green), which stabilise into a clear antiferromagnetic state at larger $b{\sim}0.9$ (c-v, light green). Finally, at the highest barriers, the two condensates uncouple and behave as two independent spin-bifurcated states (c-vi, red).

The transition from FM to AFM can be clearly seen by looking at $S_z^2 \cdot S_z^1$ (Figure 7.4d). Below the spin bifurcation all realisations trivially have $S_z^2 \cdot S_z^1 = 0$. Above the bifurcation threshold, the value of this product varies each condensate realisation. However, all realisations have $S_z^2 \cdot S_z^1 > 0$ for FM and $S_z^2 \cdot S_z^1 < 0$ for AF, with $S_z^2 \cdot S_z^1 = 0$ in between. Hence at the transition between FM and AF, the condensates look unpolarised in the circular polarisation basis. Such unpolarised emission does not occur when transitioning from AFM to uncoupled at higher barriers. Instead, some realisations simply start occurring with $S_z^2 \cdot S_z^1 > 0$, and they become equally likely to the $S_z^2 \cdot S_z^1 < 0$ realisations in the limit of uncoupled condensates. The trend in $S_z^2 \cdot S_z^1$ is matched by the Pearson correlation between the spins.

7.1.1 Josephson coupling

The phase coherence between condensates strongly implies that coherent tunnelling is the underlying physical mechanism behind the spin correlation (Figure 7.2, Figure 7.3). This tunnelling is assumed to be spin-preserving, since the wavevectors $k{\sim}0$ and distances ${\sim}10\mu m$ involved are too small for LT spin precession. [23,116] Such spin-preserving Josephson coupling would intuitively lead to a ferromagnetic state in which energy is minimised when both condensates have the same spin, but the nature of the AFM state is harder to understand. Extending Eq. (4-1) to account for two, Josephson-coupled condensates:

$$\frac{d\Psi^{(1)}}{dt} = \left[g\left(S^{(1)}\right) - \frac{i}{2}\left((\alpha_1 + \alpha_2)\, S^{(1)} + (\alpha_1 - \alpha_2) S_z^{(1)} \sigma_z\right) - \frac{1}{2}(\gamma - i\,\varepsilon)\sigma_x\right]\Psi^{(1)} - J\,\Psi^{(2)} \tag{7-1}$$

$$\frac{d\Psi^{(2)}}{dt} = \left[g\left(S^{(2)}\right) - \frac{i}{2}\left((\alpha_1+\alpha_2)\,S^{(2)} + (\alpha_1-\alpha_2)S_z^{(2)}\sigma_z\right) - \frac{1}{2}(\gamma - i\,\varepsilon)\sigma_x\right]\Psi^{(2)} - J\,\Psi^{(1)}$$

$$g\left(S^{(n)}\right) = P - \Gamma - \eta\left|\psi^{(n)}\right|^2$$

where the adiabatic reservoir limit has been applied, J is the coherent coupling and the rest of the parameters are the same as before. For simplicity, the spin dependent saturation discussed in Chapter 5 has been ignored and the saturation of each condensate has been assumed to be independent of each other. The reservoir nonlinearities of Chapter 6 have also been ignored

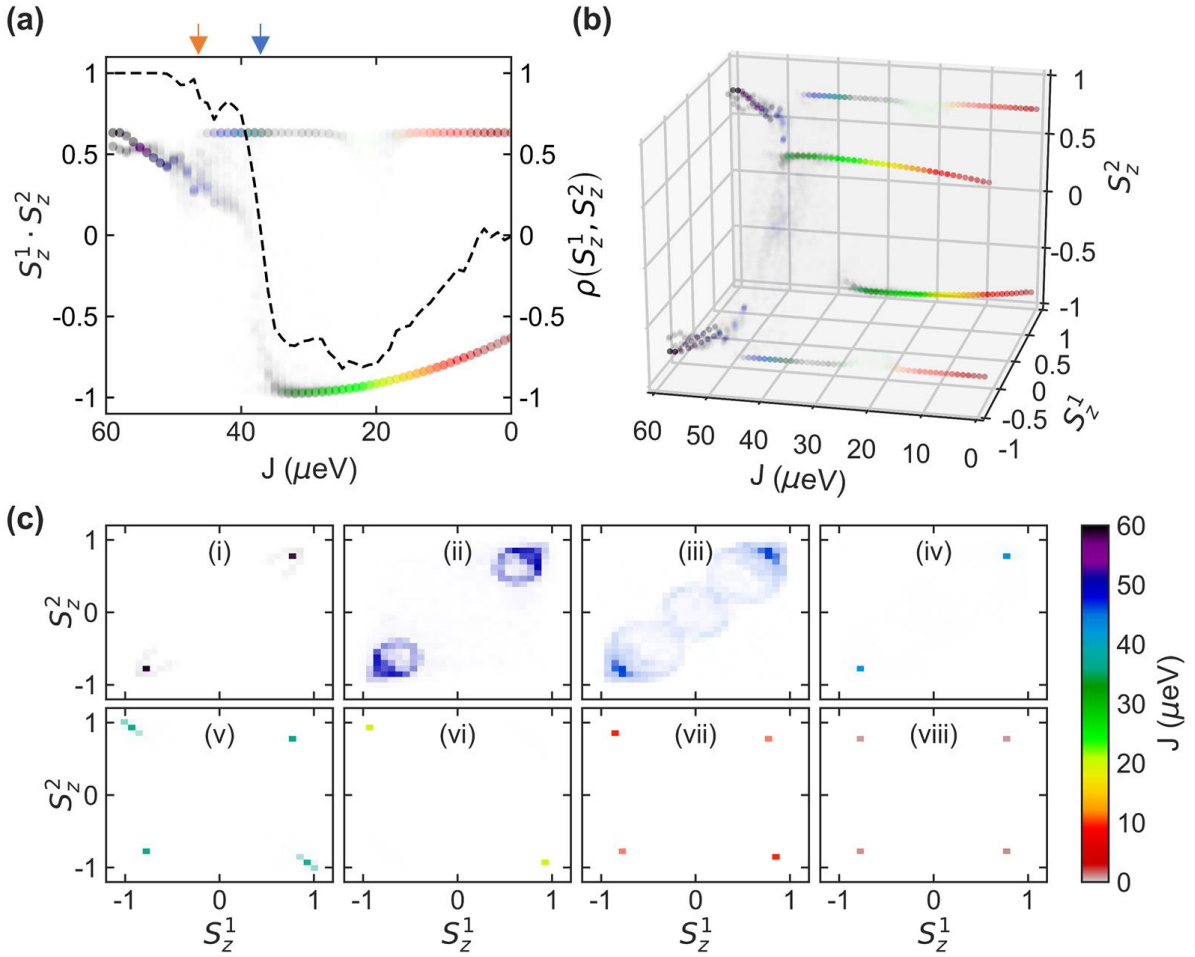

Figure 7.5 **Josephson coupling**. **(a-b)** Circular polarisation of both condensates $S_z^{1/2}$ as a function of coherent coupling J. **(c)** S_z^1 vs S_z^2 for J = (i) 59, (ii) 50, (iii) 46, (iv) 42, (v) 36, (vi) 19, (vii) 9, (viii) and 0μeV. Simulations are run for 4ns and with 1000 different initial conditions. Parameter values are $\alpha_1 = 0.01\text{ps}^{-1}$, $\alpha_2 = -0.5\alpha_1$, $\Gamma_p = 0.1\text{ps}^{-1}$, $\Gamma_X = 0.1\Gamma_p$, $R_s = 0.1\text{ps}^{-1}$, $\varepsilon = 0.04\text{ps}^{-1}$, $\gamma = 0.2\varepsilon$

since the pumping is spin balanced. The Josephson coupling constant was estimated by energy resolving the below threshold PL (for $b = 1$) and measuring the potential depth $V = 200\mu eV$ (Figure 7.1). Approximating this barrier as a square barrier leads, via a WKB approximation, to $J{\sim}4\ V\ e^{-L\sqrt{2\ m\ V}/\hbar} \approx 30\mu eV$. [129]

Although the potential depth is linearly dependent on the barrier, extracting a quantitative dependence between J and b is beyond the scope of this chapter, since an increase in the barrier also leads to an increased separation between the condensates L (see 7.1.2). For qualitative comparison, it will be assumed that the Josephson constant J is inversely related to the barrier b, and that the relationship is monotonic. The results of simulating Equation (7-1) for different J are shown in Figure 7.5.

The Pearson correlation between the spins $\rho(S_z^1, S_z^2)$ has a similar trend to that observed in experiment (Figure 7.5a). At high J (low b), the two condensate polarisations are correlated in a ferromagnetic state. As the J is reduced, the correlation decreases and changes sign, transforming into an antiferromagnetic state. In the limit of $J \to 0$, the two condensates uncouple and the correlation goes to 0. Hence the simple addition of a spin-preserving Josephson coupling can reproduce the existence of an AFM state and the condensate transition from uncoupled to AFM to FM as the coupling is increased.

Despite the qualitative agreement of experimental and simulated Pearson correlations, the simulations display a more complicated phenomenology than is observed in experiment. Two transitions can be distinguished: a transition from AFM to FM at $J{\sim}\varepsilon = 35\mu eV$ (blue arrow) and a transition to self-trapped solution at $J{\sim}50\mu eV$ (orange arrow), where the two condensates have unequal populations (not shown). Hence, at the strongest couplings (Figure 7.5c-i), the solutions are not just self-trapped in spin (through the spin bifurcation) but also self-trapped in the more conventional sense. [52,129] These spatially self-trapped states were not observed in the dataset of Figure 7.4, but there is some experimental evidence for their existence. Additionally, the simulations display very complicated limit cycle behaviour, involving all seven degrees of freedom in Equation (7-1). The projection of such an oscillation onto the circular polarisations plane is Figure 7.5c-iii. Including the spatial degrees of freedom of polaritons does not qualitatively change the results presented here. The

transition between FM and AFM states with barrier height is qualitatively reproduced, further confirming the results of Figure 7.5. Oscillations between the densities of the two condensates and competition between in-phase and out-of-phase spatial modes are also seen. Such simulations are very computationally intensive and achieving numerical convergence is not trivial, so extracting meaningful information from them is beyond the scope of this chapter.

There are other differences between experiment and simulations other than the limit cycles. Firstly, the degree of polarisation of the AFM state increases with increasing J (Figure 7.5a). Secondly, the range of J for which only the AFM is present is very small (18-25μeV). Thirdly, at the transition between the AFM and the FM state, both solutions are stable in the simulations (Figure 7.5c-v), which is not the case in the experiment. These differences might point towards the need to expand Equation (7-1) to include shot noise and spin-dependent saturation as discussed in Chapter 5, or possibly to include sources of incoherent coupling between the two condensates, possibly through a shared reservoir. Additionally, better quantitative agreement might be achieved if an accurate relationship between J and b is developed as well as a careful power dependence and parameter optimisation of Equation (7-1). Nevertheless, coherent coupling is enough to qualitatively explain the spin behaviour of two coupled condensates, and this understanding will be used in 7.2 to build condensate spin chains.

7.1.2 Unexplained phenomenology and experimental issues

The first issue in trying to reproduce theoretically the experimental results presented above is that not all sample positions behave equally. Keeping a constant laser pattern, different sample positions will show AF, FM or uncoupled condensates. Some positions will show FM or AFM condensates independently of barrier height. At some positions, one of the condensates will be unpolarised, likely due to spin flips as in Chapter 5. At other positions, the interplay between birefringence, the spin inversion of Chapter 6, and the coupling leads to different handedness and correlations being preferred at different powers (Figure 7.6). There is of yet no detailed understanding of exactly what role each of these parameters plays, other

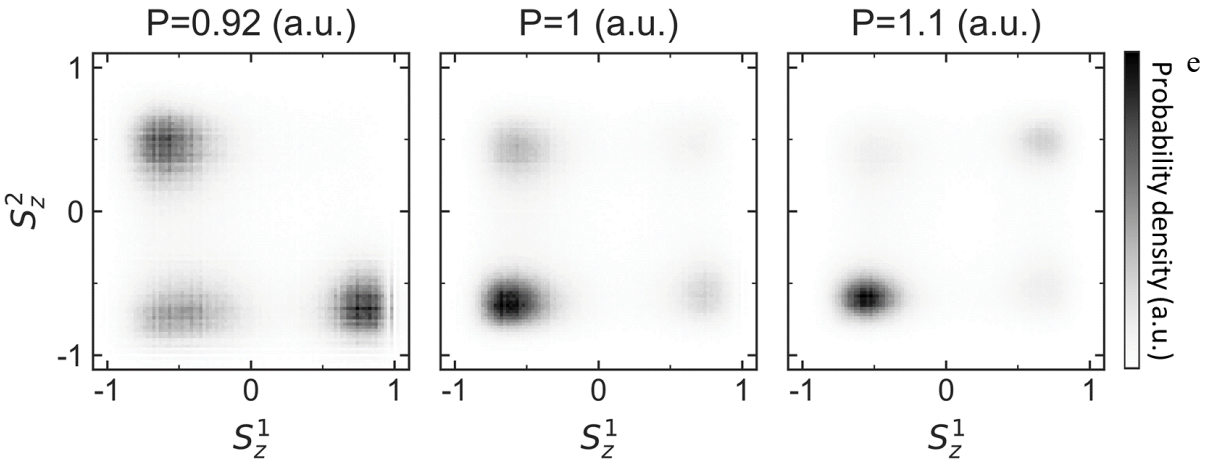

Figure 7.6 **Power dependence**. Experimental transition between AFM and FM states by changing the power P by 20%. Both condensates have a preference for left-handed emission $S_z < 1$. The circular polarisation of 1000 condensate realisations is measured on PMTs, from which these probability maps are extracted.

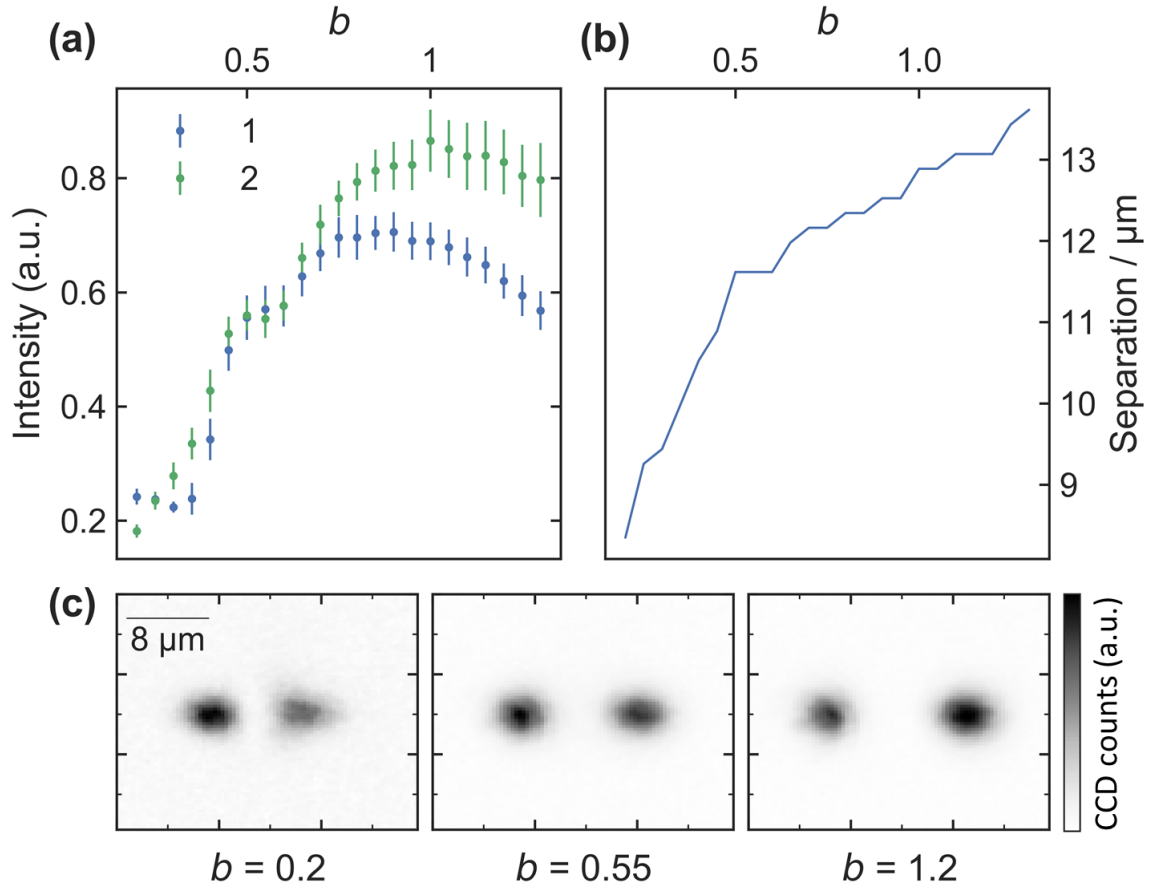

Figure 7.7 **Population imbalance**. **(a)** Occupation of left (1) and right (2) condensates as a function of barrier. **(b)** Distance between the condensate centers. **(c)** Real-space, CCD images of the condensate intensity

than their relation to sample disorder in the spin-dependent polariton energy, birefringence and/or absorption.

In addition to the position dependence, the condensate coupling can be extremely sensitive to focus and alignment: a 1μm change in focus (smaller than the setup resolution) can make the stable configuration change from FM to AFM. Hence, although the FM-AFM transition was seen repeatedly, there is no way of achieving it fully reproducibly.

There is also a spatial dependence to the condensation landscape that is not understood. Firstly, as mentioned before, an increase of the barrier height leads to a larger separation between the condensates and an increased condensate occupation (Figure 7.7). Both these changes can be easily understood from the modified energy landscape (Figure 7.1) and the increased gain due to the higher density reservoir, respectively. However, the fact that the condensate occupations do not change symmetrically with increasing barrier is counterintuitive (Figure 7.7a). At low power, the left condensate is brighter, but at high power it is the right condensate (Figure 7.7c), although one would expect the middle two pump spots to provide the same gain to both sites. More counterintuitive still is that in some circumstances, an increase of the light intensity in the *right* part of the trapping pattern leads to an increase in the emission from the *left* condensate. This might be an indication that the gain landscape is more complicated and that the two condensates have a shared reservoir, or it might an indication that energy differences between the condensates play a role in the condensation dynamics, leading to polariton flows not accounted for in the simulations in the previous section.

Finally, there is also evidence of self-sustained polarisation oscillations between the two condensates (Figure 7.8). My experiments record the circular polarisation of both condensates in single-shot, streak camera images (as in Sec. 5.1). This creates four streak traces, with oscillating periods much longer than any typical polariton timescale (~0.3GHz in Figure 7.8b, but ~0.05-1GHz in general). The fact that these oscillations are not reproduced by any of the simulations we have performed questions the validity of Eq. (7-1). A possible extension is to consider reservoir-mediated coupling, where the heavier exciton mass could lead to slower interactions. There is also some experimental evidence that these oscillations

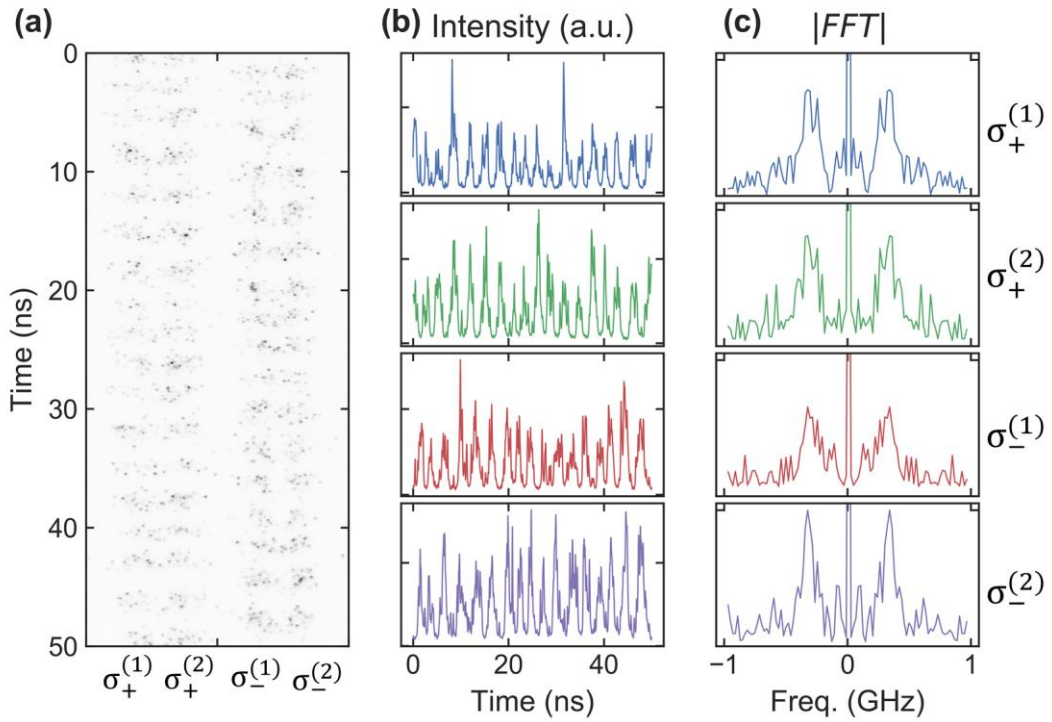

Figure 7.8 **Slow spin oscillations**. **(a)** Raw, single-shot streak image of circular polarisation components of both condensates. **(b)** Integrated time traces from the streak image, showing that both condensates spin flip simultaneously. **(c)** FFT amplitudes of each of the streak traces, showing 0.3GHz oscillations.

occur at the transition between FM and AFM, so the slow timescales could be a dynamical effect: a critical slowing down. [137] Oscillations at the transition between FM and AFM also explain why the condensates look unpolarised in time averaged measurements (Figure 7.4). Despite the open questions as to the origin of these oscillations, the fact remains that self-sustained polarisation oscillations have not been seen before in polariton condensates before and are a paradigmatic example of the complex nonlinear dynamics experienced by this system.

7.2 Spin chains

Following the demonstration of controllable coupling between two condensates, the next natural step was to realise larger condensates arrays. Two different geometries were initially explored but were trumped by the experimental difficulties highlighted in the previous section. Firstly, one dimensional condensate chains were made to study the propagation of excitations i.e. to trigger a spin flip at a chain edge and watch how quickly it arrived at the

other end. This could have answered some of the open questions about the nature of the coupling between condensates. Achieving controllable coupling for such chains was made impossible because changing the barrier between one pair of condensates leads to a change in occupation that leads to a change in the coupling of the next pair of condensates. The second geometry attempted was three condensates at the vertices of a triangle. For a situation where each pair of condensates was AF, such an arrangement would lead to geometric spin frustration. The critical dependence of frustration on spatial disorder, either present in the sample or in the laser pattern, required a level of control not experimentally available.

A geometric arrangement that does show controllable and repeatable behaviour is shown in Figure 7.9. The nonresonant pump is shaped into a 3×3 square array of laser beams, creating

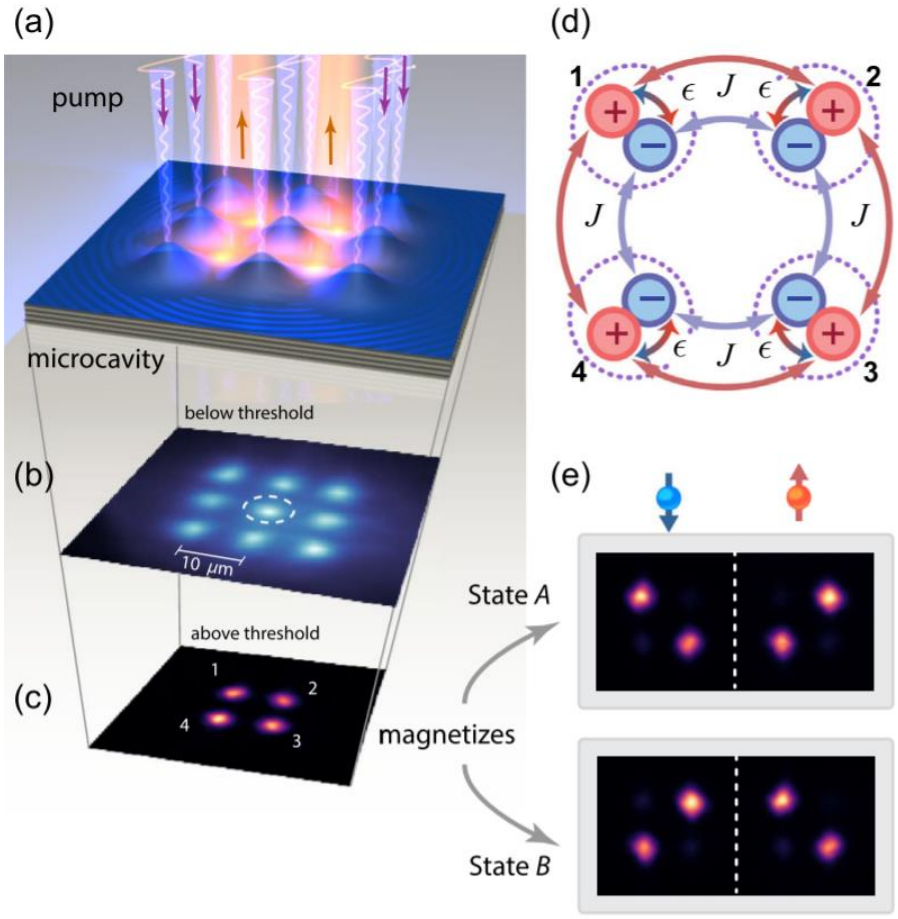

Figure 7.9 **Four coupled condensates**. **(a)** Schematic of a linearly-polarised pump (blue) creating four sites from which the condensate PL radiates (orange). **(b)** Below threshold polariton PL showing the location of the pump spots. **(c)** Above threshold PL. **(d)** Schematic of the relevant couplings: intra-site ε and inter-site J. **(e)** Two available states when all condensates are AFM. Taken from [160]

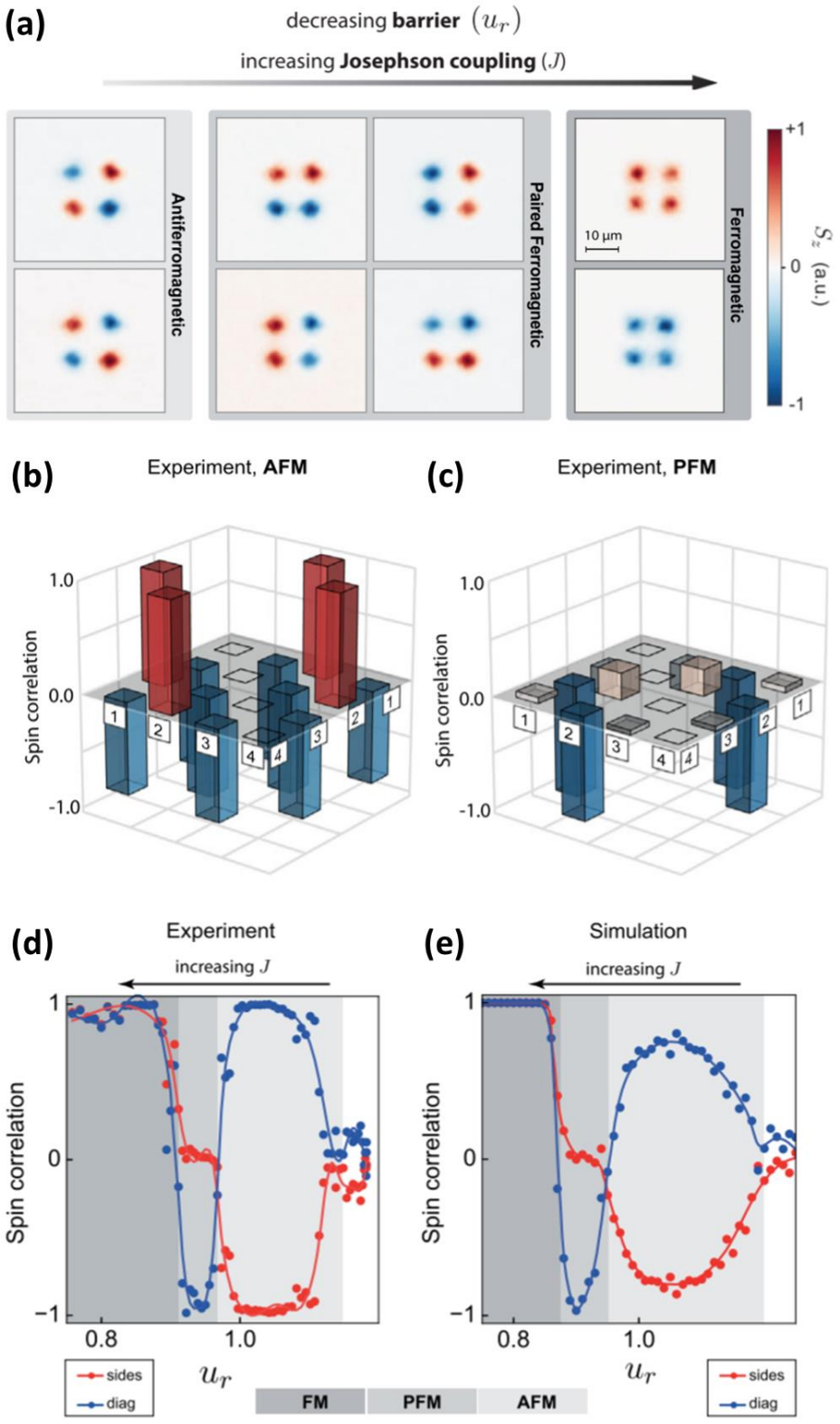

Figure 7.10 **Barrier dependence of magnetic order**. **(a)** Real-space images of the spin states for AFM, PFM and FM chains. Pearson correlation matrix for 100 realisations in AFM **(b)** or PFM **(c)** regimes. Experimental **(d)** and simulated **(e)** barrier dependence of the Pearson correlation between adjacent sites (red) and diagonal sites (blue). Modified from [160]

a 2×2 array of condensation sites. The symmetry of the pattern means that a single parameter – the intensity of the middle spot – can be used to simultaneously tune the coupling between all four pairs of condensates, avoiding the pitfalls of 1D chains. Conceptually, this arrangement is a straightforward extension of two coupled condensates: the spin components at each site are coupled via linear polarisation energy splitting ε, while neighbouring sites are coupled with a spin preserving tunnelling J.

The phenomenology is generally the same as in the two-condensate case (Figure 7.10a). When the relative intensity of the middle spot (u_r) is strong, the potential barrier between adjacent condensates is high. The spins are uncoupled and each site behaves as an independent spin bifurcated condensate. As u_r is reduced and the coupling increases, the spins anticorrelate and form an antiferromagnetic state. For small u_r, the coupling is so strong that all four condensates are in the same spin (the ferromagnetic state). However, in between AFM and FM, a new phase appears, that we call paired ferromagnetism (PFM). The system can adopt one of four possible spin configurations, rather than the two available for FM or AFM. This new phase is a direct consequence of the increased degrees of freedom in the larger chain, and an extensive numerical study of its properties can be found in [162].

As in the two-condensate case, the Pearson correlation between circular polarisations is a useful way of visualising the magnetic transitions. The 4×4 correlation matrix $C_{nm} = \rho(S_z^n, S_z^m)$ has elements numbered as in Figure 7.9c. The average C_{nm} after 100 realisations in the AFM and PFM regimes are shown in Figure 7.10b and c, respectively. In the AFM phase, neighbouring sites are anticorrelated, while the sites on the diagonals are correlated. In PFM, neighbouring sites are uncorrelated (on average) while sites on the diagonals are anticorrelated. Assuming the underlying symmetry of the pump relates to the symmetry of the solutions, the six independent elements of C_{nm} can be reduced to two: the average correlation between neighbours and the average correlation between diagonals. Plotting these two correlations as a function of u_r (Figure 7.10d) clearly shows the transition from FM, to PFM, to AFM, to uncorrelated phases. The finite range of values of u_r for which PFM appears means that this state is not simply a transition between FM and AFM, but a phase in its own right.

Qualitative agreement between the experiment and simulations is also achieved (Figure 7.10e). The simulated equations are an extension of Eq. (7-1) including the spatial degrees of freedom of polaritons. The precise form of the equations – such as whether to include the exciton reservoir dynamics, the spin dependence of the saturation or the reservoir nonlinearities – does not matter for the purposes of this chapter, since only qualitative agreement is sought:

$$\frac{d\Psi}{dt} = [g(S) - \gamma\sigma_x]\Psi - \frac{i}{2}(1 - i\Lambda)\left[((\alpha_1 + \alpha_2)\,S + (\alpha_1 - \alpha_2)S_z\sigma_z) - \varepsilon\sigma_x - \frac{\nabla^2}{2m} + V\right]\Psi \qquad (7\text{-}2)$$

$$g(S) = P - \Gamma - \eta|\Psi|^2$$

where m is the polariton mass, $\Lambda \propto P \ll 1$ is a phenomenological constant that accounts for energy relaxation, and V is the potential landscape. The potential is proportional to the spatially dependent pump P, which is shaped like in the experiment (Figure 7.9b). The middle pump spot intensity is varied, leading to the same magnetic transitions observed in experiment. As before, the agreement is qualitative and the limitations of the theory and the disagreements with experiment raised in the previous section remain.

To end this section, a larger, eight-condensate spin chain is studied. The pump is shaped into a 4×4 array of spots, creating a 3×3 array of condensation sites. An additional pump spot is placed on top of the middle site, preventing the formation of a trapped condensate at the pattern centre (Figure 7.11a). This leads to a closed chain of eight, coupled condensates (Figure 7.11b). The larger spatial extent of this geometry makes it much more sensitive to sample disorder and there is generally no magnetic order across the chain. Indeed, a 5μeV disorder potential in the simulations of Eq. (7-2) is enough to break the symmetry in both the intensity and polarisation of the chain: not all the condensates have the same intensity and there is no predominant magnetic order. The lack of a single parameter that can control the coupling between all the sites makes it impossible to controllably tune between different magnetic regimes. However, it is possible to use a random search algorithm to find a pump pattern that can counteract the spatial inhomogeneity and create FM or AFM chains. The

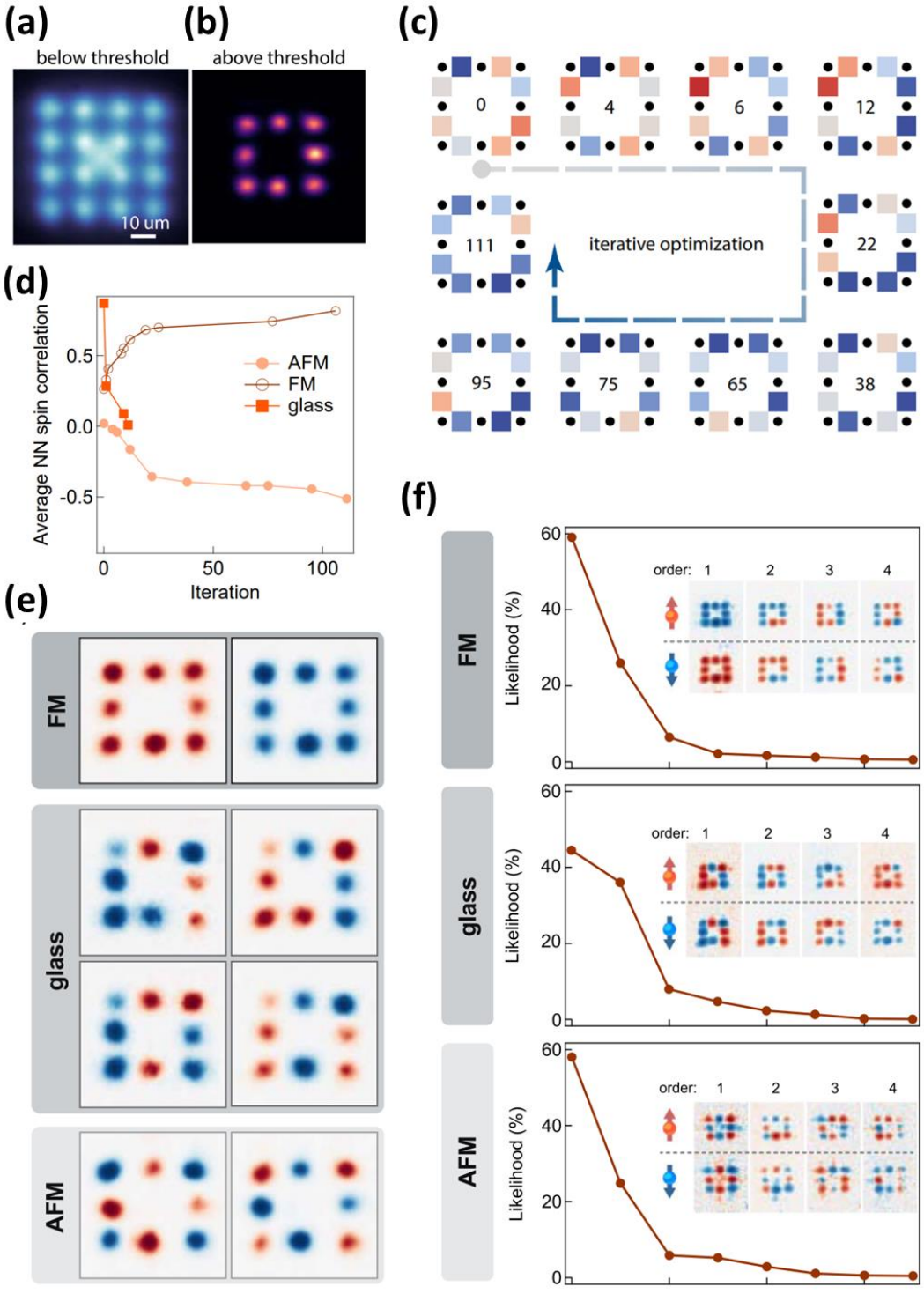

Figure 7.11 **Spin chains and iterative optimisation**. Real-space images of the polariton PL **(a)** below and **(b)** above threshold. **(c)** Diagram of the iterative optimisation. The black dots are the condensate positions, the colour of the squares in between corresponds to the degree of correlation (blue is anticorrelated, red is correlated). **(d)** Average nearest-neighbour correlation as a function of iteration step for three different algorithm targets. **(e)** Real-space spin states after optimisation. **(f)** Extracted PCA components and probabilities after optimisation. Modified from [160]

starting position is a nominally uniform intensity pattern, which in general leads to a glassy spin chain (Figure 7.11c). The average, nearest-neighbour Pearson correlation of such a chain is $\rho = 0$. The desired final state is either a FM chain ($\rho = 1$) or AFM chain ($\rho = -1$). At each step of the iteration, a 10% random noise is added to the intensities of the pump spots, 100 condensate realisations are recorded and the average NN-Pearson correlation is calculated. If the correlation is closer to the desired one, the modified intensity pattern is used as the starting point of the next iteration. Otherwise, the iteration is simply repeated. After a few tens of iterations (which take a few minutes), the chains become FM or AFM (Figure 7.11d).

Despite the iterative algorithm, the average nearest neighbour correlation in the spin chain is much smaller than that observed for the two- or four-condensate case. This is because, unlike before, the states of the system are more complicated and needs to be treated probabilistically. Previously, the condensates would end up in one of two states (↑↑ or ↓↓ for FM and ↓↑ or ↑↓ for AFM) or one of four states for PFM. Now, even if most realisations show ferromagnetism or antiferromagnetism, some realisations will be glassy, i.e. there is not always predominant magnetic order throughout the chain (Figure 7.11e). To quantify the magnetic order of a chain, *principal component analysis* (PCA) is used. Given many CCD images of the polarisation resolved PL, PCA extracts a few base images/components that represent the different spin configurations. Each component comes with an associated probability of occurrence, so that for an FM/AFM state after iterative optimisation, the first component accounts for 60% of the data (Figure 7.11f). This means that 60% of the realisations are in a pure FM/AFM state. The second component has a much smaller probability ~25%, and shows that a quarter of the realisations have a single defect at the bottom right of the pattern. For a glassy state, the first two (or more) components have similar probabilities, showing no predominance of a specific magnetic configuration.

Improvements in the search algorithm – different target functions or directed searches – could lead to stronger correlations and purer states. However, there is a fundamental limit arising from how the pattern itself is created. As mentioned in Chapter 3, there is a trade-off between the smoothness of the intensity pattern and how much of the initial light is directed to the pattern. Since the initial pump power is finite, there is a fundamental disorder in the created

SLM pattern that leads to a few μeV energy difference between condensate sites. Hence, the iterative algorithm can counteract some of the fixed sample disorder, but cannot get rid of the disorder in the optical pattern.

7.3 Conclusion

This chapter was a first step towards creating lattices of optically trapped polariton condensates. A proof-of-principle demonstration of two controllably coupled condensates was presented. A phase transition from a ferromagnetic phase – correlated circular polarisations – to an antiferromagnetic phase – anticorrelated circular polarisations – was demonstrated by controlling the amount of nonresonant light between the two condensates. This was linked to a change in the coherent coupling between the sites and a change of the barrier height created by the nonresonant excitation. For high barriers, the condensates are uncoupled. At low barriers, they are ferromagnetic. In between, the condensates are antiferromagnetic. This is supported by qualitative agreement with mean-field simulations including a spin-preserving Josephson coupling between two spinor modes.

While the coherent coupling between condensates explains a large part of the observed phenomena, open questions remain regarding the condensation dynamics of coupled, optically trapped condensates. The first relates to the spatial dynamics of condensation and how the condensate occupations are affected by the distribution of intensity in the pump pattern. The second is the unexplained, long-period, spin oscillations between the two sites. These oscillations are the first demonstration of self-sustained polarisation oscillations in a polariton system. They are not reproduced by the simulations and their timescales cannot be easily attributed to any known polariton energy scale.

Despite these difficulties, the magnetic phase transition from FM-AFM was also seen for a 2×2 array of condensates, with the appearance of a new phase in between FM and AFM: paired ferromagnetism. This controlled phase transition gets quenched by disorder in larger condensate chains: different magnetic domains are pinned to the specific potential landscape of their environment. To overcome this, an iterative random search algorithm was applied

allowing the observation of both FM and AFM phases in a 3×3 chain. This demonstrates the flexibility of using patterned nonresonant fields to overcome sample limitations.

Looking ahead, improved ways of counteracting spatial disorder need to be found to be able to create larger spin lattices. Three options are discussed. Firstly, one should move away from a random search algorithm, as it does not provide any real understanding of the underlying dynamics. Measuring the sample potential landscape below threshold and actively counteracting it could be one alternative. Secondly, smoother intensity patterns could be created with the SLM. If the current roughness is improved by an order of magnitude, the optically-induced disorder would become sufficiently small for larger spin chains to be created. However, this would require much higher laser power (~20W at 750nm) or a more efficient way of nonresonantly injecting carriers in the cavity. Thirdly, in order to counteract spatially dependent birefringence, the patterning of the pump light should be extended to include polarisation. [163]

Chapter 8 Conclusion

In this thesis, the spin and lattice properties of optically trapped polariton condensates were investigated, with the aim of using spatial laser patterning techniques in the development of polaritonic lattices.

In the first part of this thesis (Chapter 4, Chapter 5 and Chapter 6), the focus was solely on spin properties of individual trapped condensates. The separation between the condensate and the exciton reservoirs lead to the observation of a spin bifurcation: the formation of elliptically polarised condensates under linearly polarised pumping. This symmetry-breaking transition was attributed to energy and dissipation splitting between linearly polarised polariton modes, linking it to weak lasing and self-trapping. A zero-dimensional mean-field model that accurately reproduced the experimental phenomenology was developed, and was used to explain how applied electric fields could modify the condensate spin and form a low-energy spin switch.

In Chapter 5, the influence of noise on the spin-bifurcated steady states was studied. Stochastic spin flipping was observed and a controllable variation of the flip rate over many orders of magnitude demonstrated as a function of pump power and trap size. Single shot imaging of individual spin flips demonstrated that spin flips occurs at an average speed of 250ps, although they could potentially be faster than 50ps. The zero-dimensional model of the previous chapter was extended to include fluctuations from, and spin-dependence of, the stimulated scattering between the condensate and excitonic reservoirs. This modification allowed qualitatively agreement with the experimental behaviour at lower powers, and predicted frequency combs and chaotic spin dynamics that have not yet been observed at higher powers.

Whereas Chapter 4 and Chapter 5 used linearly polarised pump light, Chapter 6 studied trapped condensates under elliptically polarised pumping. The spin of the condensates was

shown to be strongly dependent on that of the pump, and two unexpected and counterintuitive observations were made. The first was spin inversion at high powers, the formation of condensates with the opposite handedness to the pump. The second observation was that the spin and intensity of the condensates are bistable and that hysteresis loops can be observed by sweeping the pump power. This bistability was shown to be strongly dependent on trap size, an effect that could not be captured within the previously developed model. This raises questions about the completeness of the model and points towards unexplored spatial spin dynamics of the exciton reservoirs, which will be the focus of future work.

Finally, Chapter 7 explored the dynamics of multiple, coupled trapped condensates. The spins of adjacent condensates were shown to couple when the potential barrier between them was sufficiently low. Two distinct spin states were observed: ferromagnetic and antiferromagnetic. By changing the pump pattern, a controllable transition between these two states was demonstrated. Phase coherence between the condensates showed that tunnelling between the condensates plays a role in the coupling between the condensates, and extending the model of Chapter 4 to include Josephson coupling between two polariton wavefunctions gave qualitative agreement with experiment. This same resonant coupling was used to understand the behaviour of a closed chain of four condensates, where a new, paired-ferromagnetic phase was observed. When attempting to create larger spin chains, it was found that spatial inhomogeneity made it impossible to create uniform magnetic phases, much less observe a transition between them. However, by carefully changing the pump pattern it was possible to overcome spatial disorder and create arbitrary magnetic phases, demonstrating the flexibility of using spatially patterned optical fields to create polariton lattices.

Looking forward, despite the proof-of-principle lattices in this thesis, using spatially patterned pump lasers on their own is unlikely to be a good approach for quantum simulation with polariton lattices. The level of control required for even the simplest quantum simulations is ruined by the large number of unknowns in the system, from the exact role of the reservoir spin to unexplained spatial dynamics in the formation of coupled condensates. Additionally, the extreme sensitivity of the phenomenology on the experimental configuration severely limits the reproducibility and scalability of experiments. Nonetheless,

the demonstration that spatially patterned lasers can dynamically counteract spatial disorder makes this technique a very useful tool to be used in combination with other methods of creating potential landscapes.

Three main hurdles need to be overcome for useful polariton quantum simulators. First, single-polariton nonlinearities need to be demonstrated for some of the more striking quantum effects, e.g strong many-body correlations. [5] In simple terms, the nonlinearity needs to be strong enough so that a single polariton causes an energy-shift larger than the linewidth, so that absorption of a single photon impedes the absorption of another photon of the same energy. Achieving such high nonlinearities will likely require using excitons with stronger interaction constants, either in different material systems or using excitons with a constant electric-dipole induced by an applied electric field. [164] The second hurdle is a better understanding of the role of spin in the relaxation and condensate formation process. In practice, it might be possible to ignore this hurdle in samples with stronger spin relaxation, either due to lower sample quality or induced by interaction with the reservoir. The final hurdle is achieving independent control of the energy and dissipation landscapes. Non-resonant fields simultaneously create real (energy) and imaginary (gain) potential landscapes, where the two parts are inherently intertwined and cannot be separated from each other. This complicates the interpretation of results and limits the types of lattices that can be created, but there are techniques that can overcome this issue. [15]

Appendix A Alignment procedure

A reproducible alignment procedure for the sample excitation (part 1 and 2 in Figure 3.1) is crucial to obtain many of the results in this thesis. It ensures that both birefringence due to non-perpendicular incidence, and pattern asymmetries are minimised.

1. Ensure the laser beam is collimated and going through the centre of all the optics, especially the SLM and lenses.
2. Remove the microscope objective and the bandpass filter.
3. With a cooled sample, ensure the laser is at normal incidence to the surface by aligning the back-reflection. Rough alignment can be done by moving the cryostat, but finer alignment needs to be done with the last mirror and the dichroic filter.
4. Step 3 changes the collection path, so a pair of mirrors after the dichroic filter (not shown in Figure 3.1) are used to realign the laser with the measurement paths. Record the position of the laser on the CCD.
5. Using a pair of irises and a lens tube, use the tip-tilt and x-y stages of the microscope objective mount to ensure the beam will go through the centre of the objective.
6. Add the objective back into the optical path. After focusing, the reflected laser beam should be in the same position on the CCD as it was without the objective, and should expand and contract symmetrically when changing the focus. If this is not the case, repeat step 5.
7. Add the bandpass filter to the optical path. Find the focal plane of the microcavity by looking at the PL and changing the position of the objective until QW defects come into focus.

Using only the SLM, make small modifications to the collimation by maximising the PL emission.

References

[1] Yu P and Cardona M 2010 *Fundamentals of Semiconductors: Physics and Materials Properties* (Berlin Heidelberg: Springer-Verlag)

[2] Dyakonov M I 2008 *Spin Physics in Semiconductors* (Berlin Heidelberg: Springer-Verlag)

[3] Brütting W 2006 *Physics of Organic Semiconductors* (John Wiley & Sons)

[4] Fraser M D, Höfling S and Yamamoto Y 2016 Physics and applications of exciton–polariton lasers *Nat. Mater.*

[5] Carusotto I and Ciuti C 2013 Quantum fluids of light *Rev. Mod. Phys.* **85** 299–366

[6] Buluta I and Nori F 2009 Quantum Simulators *Science* **326** 108–11

[7] Aspuru-Guzik A and Walther P 2012 Photonic quantum simulators *Nat. Phys.* **8** 285–91

[8] Bloch I, Dalibard J and Nascimbène S 2012 Quantum simulations with ultracold quantum gases *Nat. Phys.* **8** 267–76

[9] Houck A A, Tureci H E and Koch J 2012 On-chip quantum simulation with superconducting circuits *Nat Phys* **8** 292–9

[10] Cerda-Méndez E A et al 2010 Polariton Condensation in Dynamic Acoustic Lattices *Phys. Rev. Lett.* **105** 116402

[11] Lai C W et al 2007 Coherent zero-state and π-state in an exciton–polariton condensate array *Nature* **450** 529–32

[12] Kim N Y et al 2011 Dynamical d-wave condensation of exciton-polaritons in a two-dimensional square-lattice potential *Nat. Phys.* **7** 681–6

[13] Jacqmin T et al 2014 Direct Observation of Dirac Cones and a Flatband in a Honeycomb Lattice for Polaritons *Phys. Rev. Lett.* **112** 116402

[14] Winkler K et al 2015 A polariton condensate in a photonic crystal potential landscape *New J. Phys.* **17** 023001

[15] Schneider C, Winkler K, Fraser M D, Kamp M, Yamamoto Y, Ostrovskaya E A and Höfling S 2017 Exciton-polariton trapping and potential landscape engineering *Rep. Prog. Phys.* **80** 016503

[16] Griffiths D J 2004 *Introduction to Quantum Mechanics* (Upper Saddle River, NJ: Pearson Prentice Hall)

[17] Deng H, Haug H and Yamamoto Y 2010 Exciton-polariton Bose-Einstein condensation *Rev. Mod. Phys.* **82** 1489–537

[18] Kavokin A V, Baumberg J J, Malpuech G and Laussy F P 2017 *Microcavities* (Oxford, New York: Oxford University Press)

[19] Hecht E 2016 *Optics* (Boston: Pearson)

[20] Panzarini G et al 1999 Exciton-light coupling in single and coupled semiconductor microcavities: Polariton dispersion and polarization splitting *Phys. Rev. B* **59** 5082–9

[21] Byrnes S J 2016 Multilayer optical calculations *ArXiv160302720 Phys.*

[22] Tsotsis P, Eldridge P S, Gao T, Tsintzos S I, Hatzopoulos Z and Savvidis P G 2012 Lasing threshold doubling at the crossover from strong to weak coupling regime in GaAs microcavity *New J. Phys.* **14** 023060

[23] Langbein W, Shelykh I, Solnyshkov D, Malpuech G, Rubo Y and Kavokin A 2007 Polarization beats in ballistic propagation of exciton-polaritons in microcavities *Phys. Rev. B* **75** 075323

[24] Kavokin A, Malpuech G and Glazov M 2005 Optical Spin Hall Effect *Phys. Rev. Lett.* **95** 136601

[25] Leyder C, Romanelli M, Karr J P, Giacobino E, Liew T C H, Glazov M M, Kavokin A V, Malpuech G and Bramati A 2007 Observation of the optical spin Hall effect *Nat. Phys.* **3** 628–31

[26] Kłopotowski Ł, Martín M D, Amo A, Viña L, Shelykh I A, Glazov M M, Malpuech G, Kavokin A V and André R 2006 Optical anisotropy and pinning of the linear polarization of light in semiconductor microcavities *Solid State Commun.* **139** 511–5

[27] Michalzik R 2013 *VCSELs: Fundamentals, Technology and Applications of Vertical-Cavity Surface-Emitting Lasers* (Berlin Heidelberg: Springer-Verlag)

[28] Weisbuch C, Nishioka M, Ishikawa A and Arakawa Y 1992 Observation of the coupled exciton-photon mode splitting in a semiconductor quantum microcavity *Phys. Rev. Lett.* **69** 3314–7

[29] Hopfield J J 1958 Theory of the Contribution of Excitons to the Complex Dielectric Constant of Crystals *Phys. Rev.* **112** 1555–67

[30] Maragkou M, Grundy A J D, Ostatnický T and Lagoudakis P G 2010 Longitudinal optical phonon assisted polariton laser *Appl. Phys. Lett.* **97** 111110

[31] Ménard J-M, Poellmann C, Porer M, Leierseder U, Galopin E, Lemaître A, Amo A, Bloch J and Huber R 2014 Revealing the dark side of a bright exciton–polariton condensate *Nat. Commun.* **5**

[32] Pau S, Björk G, Jacobson J, Cao H and Yamamoto Y 1995 Microcavity exciton-polariton splitting in the linear regime *Phys. Rev. B* **51** 14437–47

[33] Houdré R, Weisbuch C, Stanley R P, Oesterle U, Pellandini P and Ilegems M 1994 Measurement of Cavity-Polariton Dispersion Curve from Angle-Resolved Photoluminescence Experiments *Phys. Rev. Lett.* **73** 2043–6

[34] Bhattacharya P, Frost T, Deshpande S, Baten M Z, Hazari A and Das A 2014 Room Temperature Electrically Injected Polariton Laser *Phys. Rev. Lett.* **112** 236802

[35] Schneider C et al 2013 An electrically pumped polariton laser *Nature* **497** 348–52

[36] Amthor M et al 2015 Optical bistability in electrically driven polariton condensates *Phys. Rev. B* **91** 081404

[37] Stevenson R M, Astratov V N, Skolnick M S, Whittaker D M, Emam-Ismail M, Tartakovskii A I, Savvidis P G, Baumberg J J and Roberts J S 2000 Continuous Wave Observation of Massive Polariton Redistribution by Stimulated Scattering in Semiconductor Microcavities *Phys. Rev. Lett.* **85** 3680–3

[38] Baumberg J J, Savvidis P G, Stevenson R M, Tartakovskii A I, Skolnick M S, Whittaker D M and Roberts J S 2000 Parametric oscillation in a vertical microcavity: A polariton condensate or micro-optical parametric oscillation *Phys. Rev. B* **62** R16247–50

[39] Savvidis P G, Baumberg J J, Stevenson R M, Skolnick M S, Whittaker D M and Roberts J S 2000 Angle-Resonant Stimulated Polariton Amplifier *Phys. Rev. Lett.* **84** 1547–50

[40] Amo A et al 2009 Collective fluid dynamics of a polariton condensate in a semiconductor microcavity *Nature* **457** 291–5

[41] Marchetti F M and Szymańska M H 2012 Vortices in Polariton OPO Superfluids *Exciton Polaritons in Microcavities* Springer Series in Solid-State Sciences (Springer, Berlin, Heidelberg) pp 173–213

[42] Lerario G et al 2017 Room-temperature superfluidity in a polariton condensate *Nat. Phys.* **13** 837–41

[43] Amo A, Lefrere J, Pigeon S, Adrados C, Ciuti C, Carusotto I, Houdre R, Giacobino E and Bramati A 2009 Superfluidity of polaritons in semiconductor microcavities *Nat Phys* **5** 805–10

[44] Amo A et al 2011 Polariton Superfluids Reveal Quantum Hydrodynamic Solitons *Science* **332** 1167–70

[45] Cilibrizzi P, Ohadi H, Ostatnicky T, Askitopoulos A, Langbein W and Lagoudakis P 2014 Linear Wave Dynamics Explains Observations Attributed to Dark Solitons in a Polariton Quantum Fluid *Phys. Rev. Lett.* **113** 103901

[46] Sich M et al 2012 Observation of bright polariton solitons in a semiconductor microcavity *Nat. Photonics* **6** 50–5

[47] Baas A, Karr J P, Eleuch H and Giacobino E 2004 Optical bistability in semiconductor microcavities *Phys. Rev. A* **69** 023809

[48] Paraïso T K, Wouters M, Léger Y, Morier-Genoud F and Deveaud-Plédran B 2010 Multistability of a coherent spin ensemble in a semiconductor microcavity *Nat. Mater.* **9** 655–60

[49] Gippius N A, Shelykh I A, Solnyshkov D D, Gavrilov S S, Rubo Y G, Kavokin A V, Tikhodeev S G and Malpuech G 2007 Polarization Multistability of Cavity Polaritons *Phys. Rev. Lett.* **98** 236401

[50] Sarkar D et al 2010 Polarization Bistability and Resultant Spin Rings in Semiconductor Microcavities *Phys. Rev. Lett.* **105** 216402

[51] Boulier T et al 2014 Polariton-generated intensity squeezing in semiconductor micropillars *Nat. Commun.* **5** 3260

[52] Abbarchi M et al 2013 Macroscopic quantum self-trapping and Josephson oscillations of exciton polaritons *Nat. Phys.* **9** 275–9

[53] Rodriguez S R K et al 2017 Probing a Dissipative Phase Transition via Dynamical Optical Hysteresis *Phys. Rev. Lett.* **118** 247402

[54] Foot C J 2005 *Atomic Physics* (Oxford ; New York: Oxford University Press)

[55] Davis K B, Mewes M-O, Joffe M A, Andrews M R and Ketterle W 1995 Evaporative Cooling of Sodium Atoms *Phys. Rev. Lett.* **74** 5202–5

[56] Davis K B, Mewes M O, Andrews M R, van Druten N J, Durfee D S, Kurn D M and Ketterle W 1995 Bose-Einstein Condensation in a Gas of Sodium Atoms *Phys. Rev. Lett.* **75** 3969–3973

[57] Anderson M H, Ensher J R, Matthews M R, Wieman C E and Cornell E A 1995 Observation of Bose-Einstein Condensation in a Dilute Atomic Vapor *Science* **269** 198–201

[58] Keldysh L V and Kozlov A N 1968 Collective Properties of Excitons in Semiconductors *Sov. J. Exp. Theor. Phys.* **27** 521

[59] Imamog¯lu A, Ram R J, Pau S and Yamamoto Y 1996 Nonequilibrium condensates and lasers without inversion: Exciton-polariton lasers *Phys. Rev. A* **53** 4250–3

[60] Deng H, Weihs G, Santori C, Bloch J and Yamamoto Y 2002 Condensation of Semiconductor Microcavity Exciton Polaritons *Science* **298** 199–202

[61] Kasprzak J et al 2006 Bose–Einstein condensation of exciton polaritons *Nature* **443** 409–14

[62] Balili R, Hartwell V, Snoke D, Pfeiffer L and West K 2007 Bose-Einstein Condensation of Microcavity Polaritons in a Trap *Science* **316** 1007–10

[63] Kéna-Cohen S and Forrest S R 2010 Room-temperature polariton lasing in an organic single-crystal microcavity *Nat. Photonics* **4** 371–5

[64] Baumberg J J et al 2008 Spontaneous Polarization Buildup in a Room-Temperature Polariton Laser *Phys. Rev. Lett.* **101** 136409

[65] Pethick C J and Smith H 2008 *Bose-Einstein Condensation in Dilute Gases* (Cambridge ; New York: Cambridge University Press)

[66] Nitsche W H, Kim N Y, Roumpos G, Schneider C, Kamp M, Höfling S, Forchel A and Yamamoto Y 2014 Algebraic order and the Berezinskii-Kosterlitz-Thouless transition in an exciton-polariton gas *Phys. Rev. B* **90** 205430

[67] Tsintzos S I, Pelekanos N T, Konstantinidis G, Hatzopoulos Z and Savvidis P G 2008 A GaAs polariton light-emitting diode operating near room temperature. *Nature* **453** 372–5

[68] Piermarocchi C, Tassone F, Savona V, Quattropani A and Schwendimann P 1997 Exciton formation rates in GaAs/${\mathrm{Al}}_{\mathrm{x}}$${\mathrm{Ga}}_{1\mathrm{\ensuremath{-}}\mathrm{x}}$As quantum wells *Phys. Rev. B* **55** 1333–6

[69] Amand T, Dareys B, Baylac B, Marie X, Barrau J, Brousseau M, Dunstan D J and Planel R 1994 Exciton formation and hole-spin relaxation in intrinsic quantum wells *Phys. Rev. B* **50** 11624–8

[70] Oh I-K, Singh J, Thilagam A and Vengurlekar A S 2000 Exciton formation assisted by LO phonons in quantum wells *Phys. Rev. B* **62** 2045–50

[71] Sun Y, Wen P, Yoon Y, Liu G, Steger M, Pfeiffer L N, West K, Snoke D W and Nelson K A 2017 Bose-Einstein Condensation of Long-Lifetime Polaritons in Thermal Equilibrium *Phys. Rev. Lett.* **118** 016602

[72] Bajoni D, Senellart P, Lemaître A and Bloch J 2007 Photon lasing in GaAs microcavity: Similarities with a polariton condensate *Phys. Rev. B* **76** 201305

[73] Tassone F, Piermarocchi C, Savona V, Quattropani A and Schwendimann P 1997 Bottleneck effects in the relaxation and photoluminescence of microcavity polaritons *Phys. Rev. B* **56** 7554–63

[74] Tartakovskii A I, Emam-Ismail M, Stevenson R M, Skolnick M S, Astratov V N, Whittaker D M, Baumberg J J and Roberts J S 2000 Relaxation bottleneck and its suppression in semiconductor microcavities *Phys. Rev. B* **62** R2283–6

[75] Roumpos G, Lai C-W, Liew T C H, Rubo Y G, Kavokin A V and Yamamoto Y 2009 Signature of the microcavity exciton\char21{}polariton relaxation mechanism in the polarization of emitted light *Phys. Rev. B* **79** 195310

[76] Houdré R, Gibernon J L, Pellandini P, Stanley R P, Oesterle U, Weisbuch C, O'Gorman J, Roycroft B and Ilegems M 1995 Saturation of the strong-coupling regime in a semiconductor microcavity: Free-carrier bleaching of cavity polaritons *Phys. Rev. B* **52** 7810–3

[77] Byrnes T, Kim N Y and Yamamoto Y 2014 Exciton-polariton condensates *Nat. Phys.* **10** 803–13

[78] Wouters M, Carusotto I and Ciuti C 2008 Spatial and spectral shape of inhomogeneous nonequilibrium exciton-polariton condensates *Phys. Rev. B* **77** 115340

[79] Wouters M and Carusotto I 2007 Excitations in a Nonequilibrium Bose-Einstein Condensate of Exciton Polaritons *Phys. Rev. Lett.* **99** 140402

[80] Boyd R W and Prato D 2008 *Nonlinear Optics, Third Edition* (Amsterdam ; Boston: Academic Press)

[81] Annett J F 2004 *Superconductivity, Superfluids, and Condensates* (Oxford ; New York: Oxford University Press)

[82] Borgh M O, Keeling J and Berloff N G 2010 Spatial pattern formation and polarization dynamics of a nonequilibrium spinor polariton condensate *Phys. Rev. B* **81** 235302

[83] Wouters M, Liew T C H and Savona V 2010 Energy relaxation in one-dimensional polariton condensates *Phys. Rev. B* **82** 245315

[84] Wouters M 2012 Energy relaxation in the mean-field description of polariton condensates *New J. Phys.* **14** 075020

[85] Christmann G, Tosi G, Berloff N G, Tsotsis P, Eldridge P S, Hatzopoulos Z, Savvidis P G and Baumberg J J 2012 Polariton ring condensates and sunflower ripples in an expanding quantum liquid *Phys. Rev. B* **85** 235303

[86] Cristofolini P, Dreismann A, Christmann G, Franchetti G, Berloff N G, Tsotsis P, Hatzopoulos Z, Savvidis P G and Baumberg J J 2013 Optical Superfluid Phase Transitions and Trapping of Polariton Condensates *Phys. Rev. Lett.* **110** 186403

[87] Wertz E et al 2012 Propagation and Amplification Dynamics of 1D Polariton Condensates *Phys. Rev. Lett.* **109** 216404

[88] Askitopoulos A, Liew T C H, Ohadi H, Hatzopoulos Z, Savvidis P G and Lagoudakis P G 2015 Robust platform for engineering pure-quantum-state transitions in polariton condensates *Phys. Rev. B* **92** 035305

[89] Wertz E et al 2010 Spontaneous formation and optical manipulation of extended polariton condensates *Nat. Phys.* **6** 860–4

[90] Cilibrizzi P, Askitopoulos A, Silva M, Bastiman F, Clarke E, Zajac J M, Langbein W and Lagoudakis P G 2014 Polariton condensation in a strain-compensated planar microcavity with InGaAs quantum wells *Appl. Phys. Lett.* **105** 191118

[91] Wertz E, Ferrier L, Solnyshkov D D, Senellart P, Bajoni D, Miard A, Lemaître A, Malpuech G and Bloch J 2009 Spontaneous formation of a polariton condensate in a planar GaAs microcavity *Appl. Phys. Lett.* **95** 051108

[92] Tosi G, Christmann G, Berloff N G, Tsotsis P, Gao T, Hatzopoulos Z, Savvidis P G and Baumberg J J 2012 Geometrically locked vortex lattices in semiconductor quantum fluids *Nat. Commun.* **3** 1243

[93] Christmann G, Tosi G, Berloff N G, Tsotsis P, Eldridge P S, Zacharias Hatzopoulos, Savvidis P G and Baumberg J J 2014 Oscillatory solitons and time-resolved phase locking of two polariton condensates *New J. Phys.* **16** 103039

[94] Berloff N G, Silva M, Kalinin K, Askitopoulos A, Töpfer J D, Cilibrizzi P, Langbein W and Lagoudakis P G 2017 Realizing the classical *XY* Hamiltonian in polariton simulators *Nat. Mater.* **16** 1120–6

[95] Askitopoulos A, Ohadi H, Kavokin A V, Hatzopoulos Z, Savvidis P G and Lagoudakis P G 2013 Polariton condensation in an optically induced two-dimensional potential *Phys. Rev. B* **88** 041308

[96] Dreismann A, Cristofolini P, Balili R, Christmann G, Pinsker F, Berloff N G, Hatzopoulos Z, Savvidis P G and Baumberg J J 2014 Coupled counterrotating

polariton condensates in optically defined annular potentials *Proc. Natl. Acad. Sci.* **111** 8770

[97] Roumpos G, Nitsche W H, Höfling S, Forchel A and Yamamoto Y 2010 Gain-Induced Trapping of Microcavity Exciton Polariton Condensates *Phys. Rev. Lett.* **104** 126403

[98] Khan S and Türeci H E 2016 Non-Hermitian coupled-mode theory for incoherently pumped exciton-polariton condensates *Phys. Rev. A* **94** 053856

[99] Zhang H, Xie J, Liu J and Wang Y 2009 Elimination of a zero-order beam induced by a pixelated spatial light modulator for holographic projection *Appl. Opt.* **48** 5834–41

[100] Leonardo R D, Ianni F and Ruocco G 2007 Computer generation of optimal holograms for optical trap arrays *Opt. Express* **15** 1913–22

[101] Gaunt A L and Hadzibabic Z 2012 Robust Digital Holography For Ultracold Atom Trapping *Sci. Rep.* **2**

[102] Pasienski M and DeMarco B 2008 A high-accuracy algorithm for designing arbitrary holographic atom traps *Opt. Express* **16** 2176–90

[103] Ohadi H, Dreismann A, Rubo Y G, Pinsker F, del Valle-Inclan Redondo Y, Tsintzos S I, Hatzopoulos Z, Savvidis P G and Baumberg J J 2015 Spontaneous Spin Bifurcations and Ferromagnetic Phase Transitions in a Spinor Exciton-Polariton Condensate *Phys. Rev. X* **5** 031002

[104] Dreismann A et al 2016 A sub-femtojoule electrical spin-switch based on optically trapped polariton condensates *Nat. Mater.* **15** 1074–8

[105] Vladimirova M et al 2010 Polariton-polariton interaction constants in microcavities *Phys. Rev. B* **82** 075301

[106] Read D, Liew T C H, Rubo Y G and Kavokin A V 2009 Stochastic polarization formation in exciton-polariton Bose-Einstein condensates *Phys. Rev. B* **80** 195309

[107] Shelykh I A, Kavokin A V, Rubo Y G, Liew T C H and Malpuech G 2010 Polariton polarization-sensitive phenomena in planar semiconductor microcavities *Semicond. Sci. Technol.* **25** 013001

[108] Sala V G, Marsault F, Wouters M, Galopin E, Sagnes I, Lemaître A, Bloch J and Amo A 2016 Stochastic precession of the polarization in a polariton laser *Phys. Rev. B* **93** 115313

[109] Levrat J et al 2010 Pinning and Depinning of the Polarization of Exciton-Polariton Condensates at Room Temperature *Phys. Rev. Lett.* **104** 166402

[110] Ohadi H, Kammann E, Liew T C H, Lagoudakis K G, Kavokin A V and Lagoudakis P G 2012 Spontaneous Symmetry Breaking in a Polariton and Photon Laser *Phys. Rev. Lett.* **109** 016404

[111] Martín M D, Aichmayr G, Viña L and André R 2002 Polarization Control of the Nonlinear Emission of Semiconductor Microcavities *Phys. Rev. Lett.* **89** 077402

[112] Deng H, Weihs G, Snoke D, Bloch J and Yamamoto Y 2003 Polariton lasing vs. photon lasing in a semiconductor microcavity. *Proc. Natl. Acad. Sci. U. S. A.* **100** 15318–23

[113] Rubo Y G, Kavokin A V and Shelykh I A 2006 Suppression of superfluidity of exciton-polaritons by magnetic field *Phys. Lett. A* **358** 227–30

[114] Larionov A V, Kulakovskii V D, Höfling S, Schneider C, Worschech L and Forchel A 2010 Polarized nonequilibrium Bose-Einstein condensates of spinor exciton polaritons in a magnetic field *Phys. Rev. Lett.* **105** 256401

[115] Sturm C, Solnyshkov D, Krebs O, Lemaître A, Sagnes I, Galopin E, Amo A, Malpuech G and Bloch J 2015 Nonequilibrium polariton condensate in a magnetic field *Phys. Rev. B* **91** 155130

[116] Kammann E, Liew T C H, Ohadi H, Cilibrizzi P, Tsotsis P, Hatzopoulos Z, Savvidis P G, Kavokin A V and Lagoudakis P G 2012 Nonlinear Optical Spin Hall Effect and Long-Range Spin Transport in Polariton Lasers *Phys. Rev. Lett.* **109** 036404

[117] Shelykh I, Malpuech G, Kavokin K V, Kavokin A V and Bigenwald P 2004 Spin dynamics of interacting exciton polaritons in microcavities *Phys. Rev. B* **70** 115301

[118] Kasprzak J, Solnyshkov D D, André R, Dang L S and Malpuech G 2008 Formation of an Exciton Polariton Condensate: Thermodynamic versus Kinetic Regimes *Phys. Rev. Lett.* **101** 146404

[119] Takemura N, Trebaol S, Wouters M, Portella-Oberli M T and Deveaud B 2014 Polaritonic Feshbach resonance *Nat. Phys.* **10** 500–4

[120] Takemura N, Trebaol S, Wouters M, Portella-Oberli M T and Deveaud B 2014 Heterodyne spectroscopy of polariton spinor interactions *Phys. Rev. B* **90** 195307

[121] Wouters M, Paraïso T K, Léger Y, Cerna R, Morier-Genoud F, Portella-Oberli M T and Deveaud-Plédran B 2013 Influence of a nonradiative reservoir on polariton spin multistability *Phys. Rev. B* **87** 045303

[122] Aleiner I L, Altshuler B L and Rubo Y G 2012 Radiative coupling and weak lasing of exciton-polariton condensates *Phys. Rev. B* **85** 121301

[123] Rayanov K, Altshuler B L, Rubo Y G and Flach S 2015 Frequency Combs with Weakly Lasing Exciton-Polariton Condensates *Phys. Rev. Lett.* **114** 193901

[124] Zhang L et al 2015 Weak lasing in one-dimensional polariton superlattices *Proc. Natl. Acad. Sci.* **112** E1516–9

[125] Balili R, Nelsen B, Snoke D W, Reid R H, Pfeiffer L and West K 2010 Huge splitting of polariton states in microcavities under stress *Phys. Rev. B* **81** 125311

[126] Meier F and Zakharchenya B P 2012 *Optical Orientation* (Elsevier)

[127] Tarucha S, Okamoto H, Iwasa Y and Miura N 1984 Exciton binding energy in GaAs quantum wells deduced from magneto-optical absorption measurement *Solid State Commun.* **52** 815–9

[128] Raghavan S, Smerzi A, Fantoni S and Shenoy S R 1999 Coherent oscillations between two weakly coupled Bose-Einstein condensates: Josephson effects, $\ensuremath{\pi}$ oscillations, and macroscopic quantum self-trapping *Phys. Rev. A* **59** 620–33

[129] Shelykh I A, Solnyshkov D D, Pavlovic G and Malpuech G 2008 Josephson effects in condensates of excitons and exciton polaritons *Phys. Rev. B* **78** 041302

[130] Wouters M 2008 Synchronized and desynchronized phases of coupled nonequilibrium exciton-polariton condensates *Phys. Rev. B* **77** 121302

[131] Malpuech G, Glazov M M, Shelykh I A, Bigenwald P and Kavokin K V 2006 Electronic control of the polarization of light emitted by polariton lasers *Appl. Phys. Lett.* **88** 111118

[132] Redondo Y del V-I, Ohadi H, Rubo Y G, Beer O, Ramsay A J, Tsintzos S I, Hatzopoulos Z, Savvidis P G and Baumberg J J 2018 Stochastic spin flips in polariton condensates: nonlinear tuning from GHz to sub-Hz *New J. Phys.* **20** 075008

[133] Cerna R, Léger Y, Paraïso T K, Wouters M, Morier-Genoud F, Portella-Oberli M T and Deveaud B 2013 Ultrafast tristable spin memory of a coherent polariton gas *Nat. Commun.* **4** 2008

[134] Rubo Y G 2004 Kinetics of the polariton condensate formation in a microcavity *Phys. Status Solidi A* **201** 641–645

[135] Wouters M and Savona V 2009 Stochastic classical field model for polariton condensates *Phys. Rev. B* **79** 165302

[136] Ciuti C, Savona V, Piermarocchi C, Quattropani A and Schwendimann P 1998 Role of the exchange of carriers in elastic exciton-exciton scattering in quantum wells *Phys. Rev. B* **58** 7926–33

[137] Strogatz S 2000 *Nonlinear dynamics and chaos* (CRC Press)

[138] Sciamanna M and Shore K A 2015 Physics and applications of laser diode chaos *Nat. Photonics* **9** 151–62

[139] Liew T C H, Kavokin A V and Shelykh I A 2008 Optical Circuits Based on Polariton Neurons in Semiconductor Microcavities *Phys. Rev. Lett.* **101** 016402

[140] Amo A, LiewT. C. H., AdradosC., HoudreR., GiacobinoE., KavokinA. V. and BramatiA. 2010 Exciton-polariton spin switches *Nat Photon* **4** 361–6

[141] Bajoni D, Semenova E, Lemaître A, Bouchoule S, Wertz E, Senellart P, Barbay S, Kuszelewicz R and Bloch J 2008 Optical Bistability in a GaAs-Based Polariton Diode *Phys. Rev. Lett.* **101** 266402

[142] Kyriienko O, Ostrovskaya E A, Egorov O A, Shelykh I A and Liew T C H 2014 Bistability in microcavities with incoherent optical or electrical excitation *Phys. Rev. B* **90** 125407

[143] Karpov D V, Savenko I G, Flayac H and Rosanov N N 2015 Dissipative soliton protocols in semiconductor microcavities at finite temperatures *Phys. Rev. B* **92** 075305

[144] Tan E Z, Sigurdsson H and Liew T C H 2018 Parity bifurcations in trapped multistable phase locked exciton-polariton condensates *Phys. Rev. B* **97** 075305

[145] Askitopoulos A, Kalinin K, Liew T C H, Cilibrizzi P, Hatzopoulos Z, Savvidis P G, Berloff N G and Lagoudakis P G 2016 Nonresonant optical control of a spinor polariton condensate *Phys. Rev. B* **93** 205307

[146] Pickup L, Kalinin K, Askitopoulos A, Hatzopoulos Z, Savvidis P G, Berloff N G and Lagoudakis P G 2017 Optical bistability under non-resonant excitation in spinor polariton condensates *ArXiv170907351 Cond-Mat*

[147] Kavokin K V, Shelykh I A, Kavokin A V, Malpuech G and Bigenwald P 2004 Quantum Theory of Spin Dynamics of Exciton-Polaritons in Microcavities *Phys. Rev. Lett.* **92** 017401

[148] Sun Y et al 2018 Stable switching among high-order modes in polariton condensates *Phys. Rev. B* **97** 045303

[149] Li G, Liew T C H, Egorov O A and Ostrovskaya E A 2015 Incoherent excitation and switching of spin states in exciton-polariton condensates *Phys. Rev. B* **92** 064304

[150] Cirac J I and Zoller P 2012 Goals and opportunities in quantum simulation *Nat. Phys.* **8** 264–6

[151] Blatt R and Roos C F 2012 Quantum simulations with trapped ions *Nat. Phys.* **8** 277–84

[152] Cerda-Méndez E A, Krizhanovskii D N, Biermann K, Hey R, Skolnick M S and Santos P V 2012 Dynamic exciton-polariton macroscopic coherent phases in a tunable dot lattice *Phys. Rev. B* **86** 100301

[153] Buller J V T, Cerda-Méndez E A, Balderas-Navarro R E, Biermann K and Santos P V 2016 Spatial self-organization of macroscopic quantum states of exciton-polaritons in acoustic lattices *New J. Phys.* **18** 073002

[154] Sala V G et al 2015 Spin-Orbit Coupling for Photons and Polaritons in Microstructures *Phys. Rev. X* **5** 011034

[155] Kim N Y, Kusudo K, Löffler A, Höfling S, Forchel A and Yamamoto Y 2013 Exciton–polariton condensates near the Dirac point in a triangular lattice *New J. Phys.* **15** 035032

[156] Masumoto N, Kim N Y, Byrnes T, Kusudo K, Löffler A, Höfling S, Forchel A and Yamamoto Y 2012 Exciton–polariton condensates with flat bands in a two-dimensional kagome lattice *New J. Phys.* **14** 065002

[157] Whittaker C E et al 2018 Exciton Polaritons in a Two-Dimensional Lieb Lattice with Spin-Orbit Coupling *Phys. Rev. Lett.* **120** 097401

[158] Klembt S, Harder T H, Egorov O A, Winkler K, Suchomel H, Beierlein J, Emmerling M, Schneider C and Höfling S 2017 Polariton condensation in S- and P-flatbands in a two-dimensional Lieb lattice *Appl. Phys. Lett.* **111** 231102

[159] Baboux F et al 2016 Bosonic Condensation and Disorder-Induced Localization in a Flat Band *Phys. Rev. Lett.* **116** 066402

[160] Ohadi H et al 2017 Spin Order and Phase Transitions in Chains of Polariton Condensates *Phys. Rev. Lett.* **119** 067401

[161] Ohadi H, del Valle-Inclan Redondo Y, Dreismann A, Rubo Y G, Pinsker F, Tsintzos S I, Hatzopoulos Z, Savvidis P G and Baumberg J J 2016 Tunable Magnetic Alignment between Trapped Exciton-Polariton Condensates *Phys. Rev. Lett.* **116** 106403

[162] Sigurdsson H, Ramsay A J, Ohadi H, Rubo Y G, Liew T C H, Baumberg J J and Shelykh I A 2017 Driven-dissipative spin chain model based on exciton-polariton condensates *Phys. Rev. B* **96** 155403

[163] Preece D, Keen S, Botvinick E, Bowman R, Padgett M and Leach J 2008 Independent polarisation control of multiple optical traps *Opt. Express* **16** 15897–902

[164] Cristofolini P, Christmann G, Tsintzos S I, Deligeorgis G, Konstantinidis G, Hatzopoulos Z, Savvidis P G and Baumberg J J 2012 Coupling Quantum Tunneling with Cavity Photons *Science* **336** 704–7